UNIVERSITY OF CALIFORNIA, SAN DIEGO

Single-cell dynamics of mammalian gene regulation

A dissertation submitted in partial satisfaction of the requirements for the degree
Doctor of Philosophy

in

Bioengineering

by

Martin Kolnik

Committee in charge:

Professor Jeff Hasty, Chair
Professor Alex Hoffmann
Professor Tracy Johnson
Professor Shyni Varghese
Professor Kun Zhang

2012

ProQuest LLC.
789 East Eisenhower Parkway
P.O. Box 1346
Ann Arbor, MI 48106 - 1346

The dissertation of Martin Kolnik is approved, and it is acceptable in quality and form for publication on microfilm and electronically:

_____

_____

_____

_____

_____

Chair

University of California, San Diego

2012

DEDICATION

To my mom and dad for selflessly supporting me in all my endeavors,
my bro for inspiring me with his good humor and calm demeanor,
and my family and friends for making the journey a memorable one.

TABLE OF CONTENTS

LIST OF ABBREVIATIONS

AU ..... arbitrary units

bp ..... base pair

CHO ..... chinese hamster ovary

CMV ..... cytomegalovirus

DAW ..... Dial-a-Wave

DNA ..... deoxyribonucleic acid

dox ..... doxycycline

EM ..... erythromycin

EMCV ..... Encephalomyocarditis Virus

ETA ..... erythromycin-responsive transactivator

eqn. ..... equation

FACS ..... fluorescence activated cell sorting

fig. ..... figure

FL. ..... fluorescence

FN ..... fibronectin

GFP ..... green fluorescent protein

IRES ..... internal ribosomal entry site

KRAB ..... Kruppel-associated box

mRNA ..... messenger ribonucleic acid

MODC ..... murine ornithine decarboxylase

NFκB ..... nuclear factor kappa B

PBS ..... phosphate buffered saline

PCR ..... polymerase chain reaction

PDMS ..... poly(dimethylsiloxane)

PTFE ..... Polytetrafluoroethylene

RPM ..... revolutions per minute

rtTA ..... reverse tetracycline transactivator

SIN . . . . . self-inactivating

tet . . . . . tetracycline

TNFα . . . . . tumor necrosis factor alpha

TF . . . . . transcription factor

tTRg . . . . . tetracycline transrepressor, G-class

UV . . . . . ultraviolet

LIST OF FIGURES

LIST OF TABLES

ACKNOWLEDGEMENTS

First and foremost I want to thank Dr. Jeff Hasty for the unwavering support, generosity and critical guidance he has given me over the course of my tenure in his lab. His unique ability to always be able to cut to the chase and see the big picture has time and again inspired and motivated me during dark and difficult segments of my career as a graduate student. His steadfast belief in my abilities has kept me going at times when my own confidence wavered. I also would like to thank Dr. Lev Tsimring and Dr. Alex Hoffmann for the insightful advice and continued support they have always graciously provided.

I feel particularly lucky to have been surrounded by amazing colleagues whose intelligence and ability far surpasses mine and continues to inspire me to better myself. Specifically, I want to thank Michael Ferry for his incredible and unique combination of encyclopedic knowledge and razor sharp critical thinking that he has always generously applied to aid me in my endeavors. Along those lines, I want to thank Ivan Razinkov for his invaluable friendship and moral support, as well as Natalie Cookson for her kindness and encouragement. I am indebted to Jangir Selimkhanov for his collaboration and I am extremely thankful for his patience and ever-ready willingness to help. Finally, I want to thank Brooks Taylor for assisting me with cell tracking, as well as all the past and present members of the Hasty Lab for making the journey a happy and memorable one.

Chapter Two contains material submitted for publication as Kolnik, M., Tsimring, L.S., Hasty, J., 2012: Vacuum-assisted cell loading enables shear-free mammalian microfluidic culture. *Lab on a Chip*

Chapter Three contains material in preparation for publication as Kolnik, M.*, Selimkhanov, J.*, Hoffmann, A., Tsimring, L.S., Hasty, J. 2012: Single-cell NFκB response in a dynamic microenvironment. (*equal contribution).

Chapter Four contains material in preparation for publication as Kolnik, M., Tsimring, L.S., Hasty, J., 2012: A genomically integrated synthetic mammalian oscillator.

VITA

2005	Bachelor of Science in Bioengineering Rice University
2007	Master of Science in Bioengineering University of California, San Diego
2012	Doctor of Philosophy in Bioengineering University of California, San Diego

PUBLICATIONS

Peer Reviewed Journal Articles

Kolnik, M., Tsimring, L.S., Hasty, J., 2012: Vacuum-assisted cell loading enables shear-free mammalian microfluidic culture. *Lab on a Chip*, submitted.

Kolnik, M.*, Selimkhanov, J.*, Hoffmann, A., Tsimring, L.S., Hasty, J. 2012: Single-cell NFκB response in a dynamic microenvironment. Manuscript in preparation. (*equal contribution).

Kolnik, M., Tsimring, L.S., Hasty, J., 2012: A genomically integrated synthetic mammalian oscillator. Manuscript in preparation.

FIELDS OF STUDY

Major Field: Bioengineering (Synthetic Biology and Microfluidics)

Studies in Biological Dynamics
Professor Jeff Hasty and Dr. Lev S. Tsimring

ABSTRACT OF THE DISSERTATION

Single-cell dynamics of mammalian gene regulation

by

Martin Kolnik

Doctor of Philosophy in Bioengineering

University of California, San Diego, 2012

Professor Jeff Hasty, Chair

Observation of single-cell behavior has become increasingly important to our understanding of complex biological systems given the highly dynamic nature of underlying regulatory processes which is often obscured by population-level observation. The focus of this dissertation is to explore gene regulatory dynamics in individual mammalian cells with the use of microfluidic technology and synthetic biology. First, I develop a novel microfluidic device platform which enables dynamic stimulation of mammalian cells during long-term perfusion culture. The device incorporates an innovative cell-loading method which uses a temporary on-chip vacuum to capture cells in culture regions isolated from detrimental effects of fluid-induced shear stress. Second, I use this device to characterize the single-cell NFκB response to dynamic stimulation with TNFα. The induction of cells with a linear temporal gradient compared to a step impulse reveals significant differences in timing variability and amplitude of the response for the two modes of stimulation. Finally, I follow a synthetic biology approach to construct artificial negative and positive transcriptional feedback gene circuits in mammalian cells

and I explore the potential of this architecture to generate oscillatory expression behavior.

Chapter 1

Introduction

Since the sequencing of the first complete genome of a free-living organism in the mid-nineties (Fleischmann et al., 1995), the rate of accumulation of biological information to describe the state of the living cell has been increasing at a tremendous rate. High-throughput technologies in sequencing, mass spectrometry and automated chromatography have enabled the collection of massive amounts of data to describe cellular genomes, transcriptomes and proteomes (Fig 1.1A). As a case in point, the GenBank sequence database at the National Center for Biotechnology Information (NCBI) has grown exponentially from just under 1 million base pairs in 1983 to over 95 billion by 2008 (Lathe et al., 2008). This biological data revolution has spawned the creation of ”omics” disciplines of science and engineering focused on analyzing the complete genome, proteome, and other -omes of an organism. Such an approach stands in sharp contrast to the traditional hypothesis-driven reductionist scientific method and has revealed a tremendous amount of complexity in terms of internal connectivity of cellular components.

The field of systems biology has emerged to support the omics sciences with the goal of using a ”systems-level” approach focused on describing how the complex interactions among the molecular components of the system drive cellular behavior and determine biological phenotype (Fig 1.1B). A significant amount of attention in the field

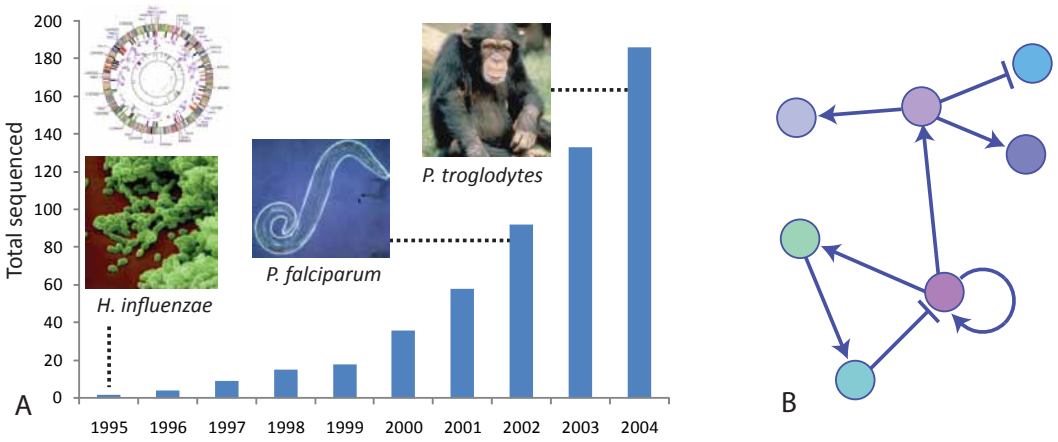

Figure 1.1: Genomics revolution and systems biology. (A) The cumulative number of complete genomes sequenced through the turn of the millennium has grown at an exponential rate. (B) The explosion of biological data describing the full complement of an organism's genes, proteins, etc has caused a paradigm shift from the traditional reductionist approach of basic biology to a systems-level focus that seeks to understand the complex dynamics interactions among cellular components. Depicted is a hypothetical gene network with various activation and inhibition interactions (arrows and barred lines) among the individual genes (circles).

has concentrated on studying molecular interactions at the single-cell level since it has become increasingly clear that the behavior of individual cells can often be masked when observing a population-level response (Longo and Hasty, 2006; Spiller et al., 2010). A common example of this phenomenon is the case in which out-of-phase oscillations of a biological signal in individual cells are obscured when observed at a whole population level. The importance of the single-cell level response as opposed to the whole population behaviour is illustrated by such biological signaling models as the shuttling of NF-kappaB from the cell cytoplasm to the nucleus in response to stimulation (Lee and Covert, 2010), the transport of calcium across the cell surface during the activation of ion-channels in neuronal signal transmission (Dolmetsch et al., 1997), and other highly dynamic processes such as segmentation during development (Pourquié, 2003) and the circadian clock (Liu et al., 2007).

The emerging focus on the study of single-cell dynamics has greatly benefited from enabling technologies such as microfluidics which allows for precise control of

the cellular environment during live-cell imaging using time-lapse microscopy. In addition, systems biology has been complemented by the related field of synthetic biology which has attempted to narrow down the study of biological networks by building simple synthetic circuits for which the dynamic interactions of a small number of components can be studied in relative isolation from the large and highly complex native interaction networks.

1.1 Microfluidics

The handling of sub-microliter volumes of fluid using micron-scale channel networks has facilitated biological research in a number of areas, primarily in the multiplexing of biochemical assays and the manipulation of live cells for long-term imaging experiments. In terms of the latter, microfluidics offers the ability to very precisely control the cellular microenvironment in both space and time due to the highly predictable laminar flow regime that is characteristic of fluid dynamics on this scale. The stimulation of cells using chemical concentration gradients, time-varying induction, and adhesion to patterned substrates are just a few examples of successful applications (Wang and Levchenko, 2009). The ability to expose cells to a time-varying inducer using microfluidics is of particular interest since this type of stimulation is not easily achieved in traditional macroscale culture platforms but such dynamic stimulation most closely mimics the ever-changing natural environment in which cells normally reside. Several microbial studies using microfluidic platforms have successfully embraced the power of dynamic stimulation to observe biological behaviors at the single-cell level and reveal network properties that are masked by traditional static induction systems. Bennett et al. (2008) used a microfluidic device to expose cells to pulses of galactose at various frequencies to reveal that the *Saccharomyces cerevisiae* galactose utilization gene network acts as a low-pass filter that allows the organism to ignore transient fluctations and only respond to a slowly changing environment. Similarly, Hersen et al. (2008) explored the response of the *S. cerevisiae* HOG signaling pathway to osmolar shock oscillating over

a range of frequencies and discovered that the signaling network integrates the stimulus during rapid induction cycles but responds faithfully to slowly changing induction conditions. Furthermore, Charvin et al. (2008) demonstated the use of a microfluidic device to administer transient periodic induction of the G1/S or G2/M trigger in *S. cerevisiae* to synchronize division in a growing field of cells followed for more than five generations.

While such microbial platforms for dynamic stimulation using microfluidics have been successfully deployed to study cell behavior at the single-cell level, studies using mammalian cells have been somewhat slower to adopt this approach. Mammalian microfluidics has lagged behind microbial systems partly due to the increased sensitivity of mammalian cells to external culture conditions in comparison to most model microbial organisms. Small deviations away from optimal pH, osmolarity, temperature, shear stress and other external factors tend to quickly have detrimental effects on mammalian cell viability and capacity for proliferation (Kim et al., 2007). Although the micron scale offers the advantages of low reagent volume consumption, the downside is that the extremely high surface area to volume ratio of microfluidic systems greatly increases evaporative losses of fluid, thus exacerbating the problems of osmolarity and pH change of the mammalian culture medium. Therefore, the design of mammalian microfluidic systems must take extra care to take these considerations into account. Successful designs typically rely on perfusion flow of media to constantly refresh the culture volume and reduce evaporation or a humidified environmental chamber is used to enclose the microfluidic device in the case that media flow is absent during cell culture. In addition to maintaining optimal culture conditions, retention of cells within the device has to be achieved during perfusion flow to prevent the washing away of proliferating cells. Physical trapping methods tend to rely on channel geometries which sequester cells in regions with high resistance to flow, while more complicated designs may employ multi-layer channel networks and/or additional fluid control valves (Nilsson et al., 2009).

Despite the additional challenges of working with mammalian cells, several microfluidic devices have been designed to successfully analyze the live-cell response of individual mammalian cells to dynamic stimulation. Gómez-Sjöberg et al. (2007) de-

veloped a device with automated valves to control the addressability of individual culture chambers to allow for rapid periodic exchange of culture media for cell stimulation studies. To achieve a similar effect, King et al. (2007) used flow-encoded switching of two media inlets to enable periodic stimulation of cells in downstream culture chambers. Both of these approaches can deliver step-functions of stimulus at various concentration to the cells, but they are limited in this manner and cannot create a smooth continuous waveform such as triangle or sine wave which are often more relevant forms of stimulation in a natural biological context. Such a true function generator for dynamic stimulation of mammalian cells was developed by Lee et al. (2008) of CellASIC corporation but has not yet seen application in literature, perhaps due to the complex/expensive nature of the associated pneumatic flow controller external hardware or due to on-chip limitations of an extremely large culture chamber with a long turnover time. Similarly, Zhang and Roper (2008) developed a 3-layer glass/polymer device employing pneumatic pumps for mixing two flow streams in order to generate temporal gradients for delivery to cells.

While a handful of existing devices are able to achieve true dynamic stimulation by generating any desired waveform of inducer stimulus for delivery to mammalian cells, their limited adoption is indicative of high barriers to use due to complex fabrication (multi-layer/multi-material) and/or costly/complicated external support hardware. In addition, such designs devote little emphasis to robust cell-trapping which is necessary in the case of perfusion culture where a variety of more sensitive cell types can suffer from detrimental shear stress effects. To address these concerns, in chapter two I present a novel microfludic mammalian culture device with true function generation capability for long-term dynamic stimulation experiments. This design employs a new method of loading cells into small culture chambers that are highly isolated from the convective forces of fluid flow by employing an on-chip temporary vacuum to remove air from the chambers and replace the volume with fluid containing the cell suspension. The simplicity of this one-layer cell loading and culture method is coupled to an equally simple and robust function generator termed the ”dial-a-wave” to develop a

complete platform for user-friendly dynamic stimulation for long-term perfusion culture. In chapter three, I describe the use of this platform to characterize the response of the NFkappaB signaling pathway. The results from this study emphasize how the unique ability of microfluidics to stimulate cells with a time-varying concentration profile can shed new light on the behavior of regulatory networks at the single-cell level.

1.2 Synthetic biology

In addition to using novel tools such as microfluidics to study the component interactions of native regulatory networks, systems biology has benefited from the related field of synethic biology. This relatively nascent discipline seeks to build and characterize artificial gene regulatory networks with only a handful of components that are typically isolated from the complex 'spaghetti soup' of native regulation. In this manner, synthetic biologists hope to use the insight gained from studying the dynamics of small synthetic networks to better predict the behavior of larger native ones. In addition, translational synthetic biology hopes to further apply that insight towards the goal of creating rationally designed biological regulatory networks for controlling cell behavior in medical and bioprocess applications.

In the past decade, much has been done to carryover the knowledge from pioneering work in bacteria to build synthetic gene circuits with complex dynamic behavior in mammalian cells. Early mammalian synthetic biology focused on developing the biological parts necessary to enable control of transgene expression. The brunt of the initial effort centered on the creation and characterization of novel chimeric transcription factors (TFs) consisting of a DNA-binding protein fused to either an activation domain (e.g. VP16 from herpes simplex virus) or a silencing domain (KRAB from human kox1 protein) (Weber and Fussenegger, 2006). The activity of the DNA-binding protein is typically tunable by a small-molecule chemical since many of these domains are prokaryotic repressors which evolved to respond to antibiotic compounds such as tetracycline, pristinamycin and erythromycin (Gossen and Bujard, 1992; Fussenegger

et al., 2000; Weber et al., 2002). The use of these chimeric TFs allowed for the creation of the first synthetic mammalian regulatory cascade at the turn of the millennium (Moser et al., 2001) and the subsequent development of more complex circuits such as the epigenetic toggle switch (Kramer et al., 2004), a hysteretic switch (Kramer and Fussenegger, 2005) and a variety of logic gates to perform Boolean algebra (Rinaudo et al., 2007).

While such early synthetic circuits largely focused on exploring the steady state characteristics of gene networks, it took some time to develop a fundamental understanding of the dynamics of biomolecular interactions in a gene network that allow for the creation of more complex circuits such as oscillators. Again, much of the groundwork for mammalian synthetic biology in this regard was laid by breakthrough studies in bacteria. The first artificial genetic oscillator in E. coli was somewhat noisy and unstable (Elowitz et al., 2000), but paved the way for the development of a robust and tunable version several years later (Stricker et al., 2008). Experimental and computational characterization of these bacterial oscillators revealed that several key ingredients are necessary for robust functionality, such as the presence of time-delayed negative feedback, fast-degradation kinetics, and a coupling to rapid positive feedback. These observations were recently put into practice to develop mammalian versions of a synthetic genetic oscillator transiently transfected into chinese hamster ovary cells (CHO). In the first system, Tigges et al. (2009) built a coupled feedback auto-regulated sense-antisense transcription control circuit that produced autonomous and self-sustained oscillations of GFP reporter protein with a period that was tunable in the range of two to five hours depending on the plasmid dosage during transient transfection of the circuit components. In a follow up study, Tigges et al. (2010) incorporated an intronically encoded siRNA to provide the delayed negative feedback which resulted in low-frequency oscillations with a period of approximately 26 hours upon transient transfection into CHO cells. These milestone studies are critical to gaining a deeper understanding of how mammalian gene networks give rise to complex dynamics - knowledge that is essential for translating basic synthetic biology research towards clinical and bioprocess

applications.

There has been significant progress in this regard and clinical applications of mammalian synthetic biology have begun to emerge (Khalil and Collins, 2010; Ruder et al., 2011). For example, artificial circuits have been developed to aid in identification of novel antimicrobials and screen for anti-cancer drug candidates. Weber et al. (2008) designed a synthetic circuit in CHO cells to screen for small molecules that could potentially alleviate the drug-resistance of *Mycobaterium tuberculosis* to treatment with Ethionamide. The synthetic circuit features a transactivator driving a fluorescent reporter to identify molecules that interfere with a DNA-binding portion of the transactivator which is normally responsible for promoting drug resistance by the bacterium. In terms of anti-cancer candidates, Gonzalez-Nicolini and Fussenegger (2005) developed a synthetic circuit to control proliferation of CHO cells in an inducible manner allowing for the creation of two isogenic populations of growth-arrested and normally proliferating cells. The challenge of such two populations with cytotoxic drug candidates then allows for the screening of compounds which preferentially kill proliferating cells without affecting the growth-arrested population. Moving beyond drug screening strategies to cell-based therapies, Chen et al. (2010) have developed a novel synthetic RNA regulatory circuit to tightly control T-cell proliferation in response to drug application. In this way, the success of adoptive transfer of T-cells during immunotherapy can be greatly increased by using the RNA circuit to induce T-cell proliferation for a prescribed amount of time while avoiding uncontrolled growth that can lead to leukemic transformation. Another cell-therapy approach developed by Kemmer et al. (2010) employs a synthetic gene circuit to sense elevated uric acid using an engineered trans-silencer sensitive to urate. During overproduction of urate, the trans-silencer is inactivated and allows for the expression of a urate oxidase that eliminates uric acid and brings its level back to subpathological levels in mice implanted with the engineered cells.

While it is clear that synthetic mammalian biology is slowly building momentum towards gaining a foothold in clinical applications, much remains to be done in order to translate the successes of basic circuits such as switches and oscillators into real-

world applications. A significant hurdle for this transition is that many of the interesting mammalian synthetic gene circuits are originally demonstrated in a plasmid-based context where the circuits are only transiently transfected in the mammalian cells and are eventually diluted out by cell division. Unlike many model prokaryotes, mammalian cells lack a means to efficiently replicate and maintain an episomal vector and it thus becomes necessary to integrate genes into the genome in order to maintain circuit function. In terms of mammalian synthetic biology, genomic integration adds an extra layer of complexity due to the unpredictable regulatory effects of local chromatin remodeling upon insertion of the circuit into random sites within the genome. Unless a site-directed integration approach is used, the identification of functional synthetic circuits requires the screening of many clones to isolate a cell line with the desirable behavior. In chapter five, I discuss the construction and characterization of a novel synthetic genetic oscillator within the context of integration into a mammalian genome.

Chapter 2

Mammalian microfluidic culture platform for dynamic stimulation

2.1 Design criteria

Microfluidics offers an attractive alternative to standard culture dishes for live-cell imaging by allowing the user an unprecedented level of control of the cellular environment in both space and time. However, this level of control does not come free, as microfluidics requires a more complex experimental setup than a simple culture plate that is readily seeded with cells and media. Preparation and handling of a fabricated microfluidic device and its associated fluidic connections of several lines of microbore tubing interfaced with syringe-type fluid reservoirs generally involves considerable effort beyond simply securing a culture dish on the microscope stage (Fig 2.1A). In addition, the actual design of the microfluidic device network has to take into account how the extreme difference of scale affects cell culture parameters that govern viability and proliferation in order to ensure biologically relevant experimental conditions. The goal of developing a successful microfluidic platform for routine adoption in cell biology becomes maximizing the capabilities offered for controlling the cellular microenvironment while minimizing the time and effort required for experimental setup.

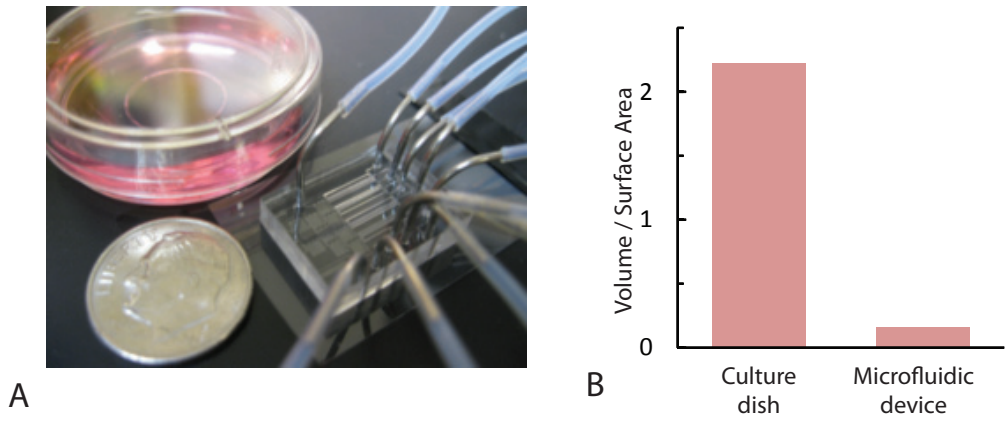

Figure 2.1: Traditional culture versus microfluidics (A) Close-up comparison of a 35mm glass-bottom culture dish routinely used for live-cell imaging and a microfluidic device. (B) The ratio of media fluid volume to growth surface area is drastically lower in a microfluidic chip compared to a standard culture dish.

2.2 Microscale culture parameters

To ensure that biological measurements at the microscale are relevant in terms of observations made in typical macroscale culture, a microfluidic platform must provide a healthy culture environment that is consistent with traditional culture methods despite the vast differences in scale. A detailed analysis of important parameters to maintain optimal culture conditions can be found elsewhere (Kim et al., 2007; Lee et al., 2011), and here I provide a basic overview of the critical factors that must be considered.

In brief, the most important considerations arise as a result of the drastically smaller volume to surface area ratio of microfluidic devices compared to standard culture (Fig 2.1B). Due to the extremely small volumes of fluid and the highly-gas permeable nature of the commonly used polymer for device fabrication (PDMS), evaporation rates and carbon dioxide exchange can strongly and rapidly affect the culture media osmolarity and pH buffering capacity. To combat this effect, a perfusion flow of media is typically established in microfluidic devices in order to constantly refresh the culture fluid volume. However, continuous perfusion culture requires that careful attention is given to designing the channel geometries such that cells can be effectively retained in

a designated culture area and so that fluid flow rates through this region are low enough to prevent cell damage due to shear stress. Given the laminar nature of fluid flow on the microscale, shear stress at the surface of a microfluidic channel can be estimated as follows (Kim et al., 2006):

$$\tau = \frac{6\mu Q}{h^2 w} \tag{2.1}$$

where μ is the viscosity (kg m^{-1} s^{-1}), Q is the volumetric flow rate (m^3 s^{-1}) and h and w are the channel height and width in meters. Thus for a given volumetric flow rate, increasing the height of the channels is one way to achieve decreased shear stress at the channel wall-fluid interface. This is a common strategy for device designs which do not employ specialized geometries to trap and retain cells and instead rely on cell adhesion to the substrate in a single perfusion channel with a large ceiling height. During cell seeding in such designs, flow is temporarily reduced to zero for a few hours and perfusion is resumed only once cells have fully attached to the substrate. A significant challenge with using this strategy is achieving a high-enough cell density throughout the relatively shallow culture chamber (typically $<150\mu$m ceiling) without having too many cells settle in and clog up the device ports (fluid heights here are on the order of millimeters and hence the ports contain several orders of magnitude more cells than the device channels). A more successful strategy relies on actively designing the channel geometries in a way that creates regions of high resistance to fluid flow where cells can be trapped and selectively retained while the remaining channels of the device are flushed clear for unobstructed perfusion flow. A variety of such designs exist in literature (Lee et al., 2006; Park et al., 2009; Di Carlo et al., 2006) and I discuss the development of a novel method for loading cells into such regions using an on-chip vacuum in section 2.4 of this chapter.

2.3 Design development

The design goal was to create a microfluidic culture platform with the aforementioned criteria in mind and the capability to dynamically stimulate cells with any desired real-time waveform of induction during long-term continuous perfusion culture. This separates the design into two discrete components consisting of a fluidic mixer network for generating the waveform and a separate region of the device for cell trapping and cell culture (Fig 2.2).

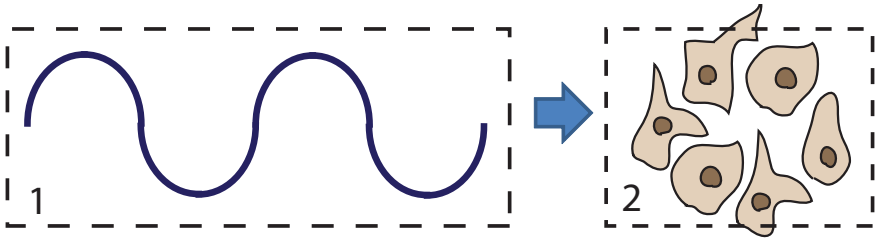

Figure 2.2: Device concept. The design seeks to couple a fluidic function generator (1) with a downstream cell culture region (2) for dynamic stimulation experiments.

2.3.1 Dial-a-wave function generator

A fluidic mixer network and associated external hardware and software was previously developed in our laboratory for the generation of real-time dynamic induction in a microfluidic device (Bennett et al., 2008). This original version of the function generator was termed the "Dial-a-wave" (DAW) in reference to its ability to dial-in any desired waveform. The DAW network was subsequently redesigned for better performance and the hardware and software have also been updated. The details of operating the DAW are well documented elsewhere (Ferry et al., 2011), but the basic premise involves mixing two fluid streams (one with inducer and the other with control media) at precise ratios to generate any intermediate concentration of inducer that is subsequently delivered to cells downstream of the mixer junction. The ratio of mixing corresponds to the ratio of flow rates which is in turn determined by increasing the hydrostatic pressure at one

input while at the same time decreasing the pressure by exactly the same amount at the other input (Fig 2.3). By automating the control of the hydrostatic pressures using pro-

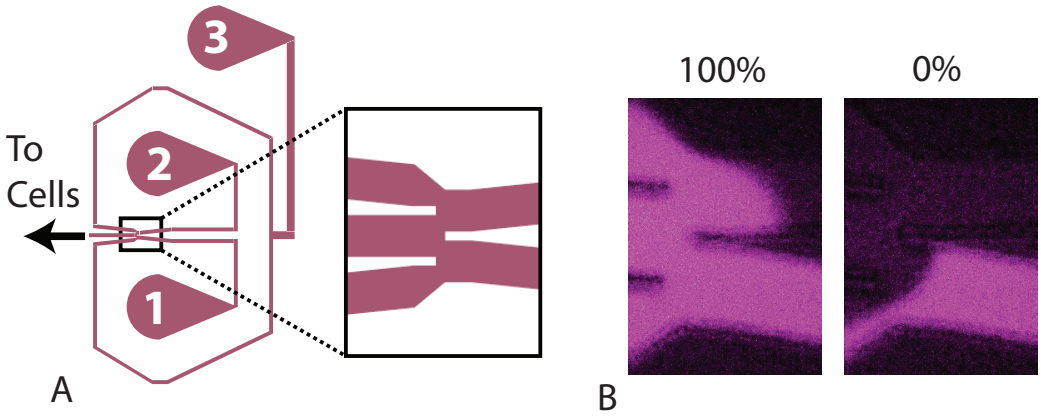

Figure 2.3: Dial-a-Wave mixer. (A) Fluidic network and close-up of mixing junction. Ports one and two are used to mix inducing and control media, while port three is a shunt to prevent backflow. (B) Visualization of fluorescent dye during signal delivery.

grammable software that communicates with linear stepper motors which move along a vertical direction, the DAW system is capable of generating any real-time concentration profile (sine, triangle, square waves, etc. of any desired frequency). The use of this system for a mammalian device design only required increasing the channel heights of the junction network and chaotic mixers to a suitable level to achieve flow rates fast enough to rapidly turn over the larger volumes of the mammalian culture channels. The precise fabrication methods are described later in this chapter.

2.3.2 Cell culture traps

The brunt of the device design effort focused on the development of an effective cell trapping geometry for robust long-term cell culture. I considered a simple large rectangular culture chamber, but experiments confirmed worries that the time required to allow cells to adhere to the substrate caused excessive settling of cells in the loading ports resulting in complete clogging which rendered subsequent perfusion culture ineffective. Thus it was clear from the start that a more complex trapping geometry would

be required, and the most logical first step was to adapt a proven literature design and couple it to the DAW mixer network. A high-aspect ratio trapping region developed by Lee et al. (2006) seemed like a suitable choice. In this device, a C-shaped curtain that comes down from the ceiling of the chamber but leaves a small gap at the glass coverslip interface which creates a culture region with high-resistance to convective flow but with diffusive transport of nutrients through the gap under the curtain (Fig 2.4A). Using this concept I designed a culture chamber of similar dimensions but with an expanded central culture area to accommodate a greater number of cells. The circular culture area within the C-barrier of the original design has a diameter of 280μm which could accommodate roughly thirty fully spread out fibroblasts. I expanded this diameter to 1,250μm in order to accommodate approximately 600 cells (Fig 2.4B). This required the addition of three

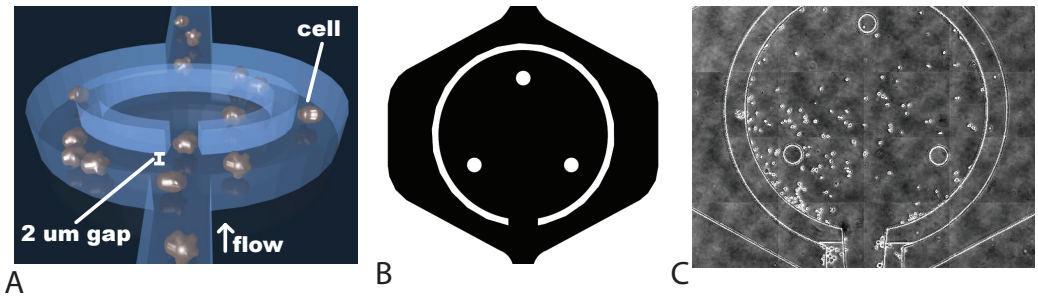

Figure 2.4: High-aspect ratio trapping region (A) Conceptual depiction of cell trapping. As a cell suspension is loaded into the chamber from the bottom channel, most cells go around the C-barrier and exit through the top channel but a few cells enter the C-region and are retained. Subsequent high-flow can be used to flush untrapped cells out of the device. The gap under the C-shaped curtain allows for mass transport to deliver nutrients to cells during perfusion. (B) CAD image for mask creating during fabrication. (C) Image of cells loaded into the finished device after cell seeding.

circular stabilizer posts to hold up the C-shaped curtain and prevent it from contacting the glass coverslip during device fabrication causing irreversible bonding. Cell seeding was effective and the culture area could be rapidly loaded with an adequate density of cells (Fig 2.4C). Unfortunately, extensive testing of the device was unable to maintain cell viability beyond just a few hours using either HeLa cells or NIH 3t3 fibroblasts. Troubleshooting initially focused on maintaining optimal pH of the perfusion medium,

as I thought that perhaps the gas-permeable PDMS was causing the bicarbonate-based buffering system of the media to fail as a result of exposure to atmospheric air rather than the 5% CO_2 used in traditional tissue culture incubators. Previous literature indicated that during perfusion culture the device does not need to be exposed to 5% CO_2 due to constant media renewal (Hung et al., 2005), but even when I used a humidified 5% CO_2 atmospheric chamber around the device cell viability could not be maintained. The next step was to try CO_2-independent media. I cultured the cells in Leibovitz L-15 media developed for this purpose (Leibovitz, 1963) but was unable to extend viability in the devices beyond the few hours I was able to achieve previously with CO_2-dependent media. This was extremely confounding as I was essentially recreating the microfluidic culture conditions validated by the aforementioned studies that originially developed the C-barrier design, but I could not replicate successful long-term cell culture inside the devices. One observation I made during this troubleshooting period was that while cells inside the culture chambers typically died within a few hours, regions within the device that were clogged with cells (such as the cell-loading port) exhibited normal viability and morphology (Fig 2.5). This led me to believe that perhaps shear stress due to convective flow was negatively affecting cells in the culture region of the device while a lack of flow near the clogged ports could be responsible for the improved viability there.

Fibroblasts, for example, have been shown to respond to a wide range of shear stresses depending on the cellular behavior in question (migration, secretion, proliferation, etc) (Dan et al., 2010). While values of 0.5 - 10 dyn/cm^2 are typical of microfluidic culture devices for mammalian cell culture (Lee et al., 2011), fibroblasts in-vivo normally reside in an extracellular matrix environment where extremely slow fluid flow rates 0.1-4 μm/s dominate (this is called "interstitial flow") (Scallan et al., 2010). The shear stresses in this space has been estimated to be 0.005-0.015 dyn/cm^2 (Pedersen et al., 2007), which is an order of magnitude lower than the protection provided by the high-resistance C-barrier (0.1-0.8 dyn/cm^2 for 280 μm culture area) (Lee et al., 2006).

With these considerations in mind, I designed several novel microfluidic culture chambers through an iterative process with the primary aim of reducing shear stress

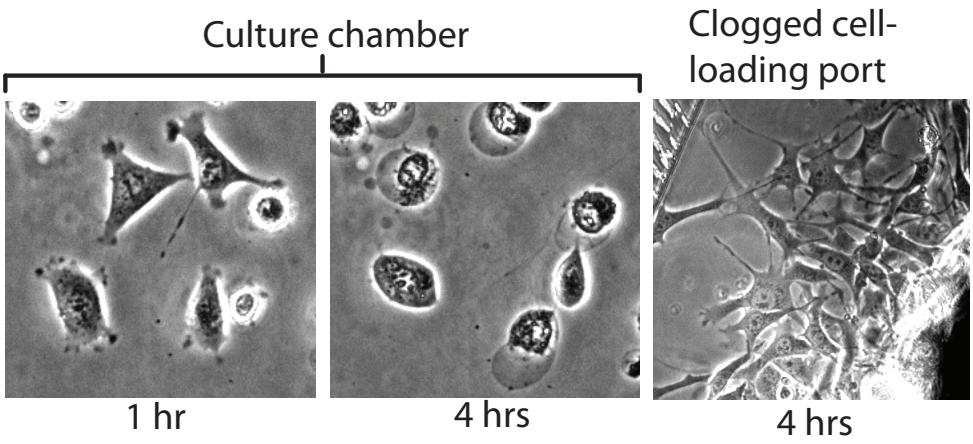

Figure 2.5: Troubleshooting cell viability in perfusion culture. Upon initial seeding into the device, mouse fibroblasts would begin to attach and spread out within the perfused culture chamber, but within a few hours the cells began to die as evidenced by cell blebbing and eventual rupture of the cell membrane. Meanwhile, in areas of the device where perfusion was limited due to clogging by excessive settling of cells, viability and proliferation appeared normal.

due to fluid flow. My first idea for a low-flow rate culture chamber was based on the concept that two parallel channels connected by a rectangular cell trap could be precisely set to have the same pressure drop driving fluid flow, thus rendering flow through the connecting region to be essentially zero under ideal conditions. I fabricated such a device with a central rectangular region and was able to easily load cells by creating a pressure differential between the parallel channels. Upon pressure equalization, flow through the central region ceased and cells were retained (Fig 2.6A). Unfortunately, I witnessed a similar behavior to what I had seen previously, namely that cells would begin to attach and show signs of spreading, but within a couple hours cell blebbing and eventual death occurred. Naturally, I thought the solution was to further limit flow through the cell chamber, so I modified the rectangle into a circular trap with two small openings connecting it to the parallel flow channels (Fig 2.6B). With this design, it was slightly more difficult to evenly distribute cells across the circular area due to the increased resistance of this chamber, but sufficient cell loading was possible with a little bit of flicking of the microfluidic lines during cell seeding. Again, extensive testing

with this device indicated a similar lack of long-term viability. Further expanding on this design, I greatly increased the resistance of the central cell culture region by constricting the openings and limiting the height of one of the openings to 5 μm so that during loading cells could not pass through the main culture chamber and would be effectively retained (Fig 2.6C). With this design I was able to increase viability to several hours, but long-term healthy microfluidic cell culture still eluded me.

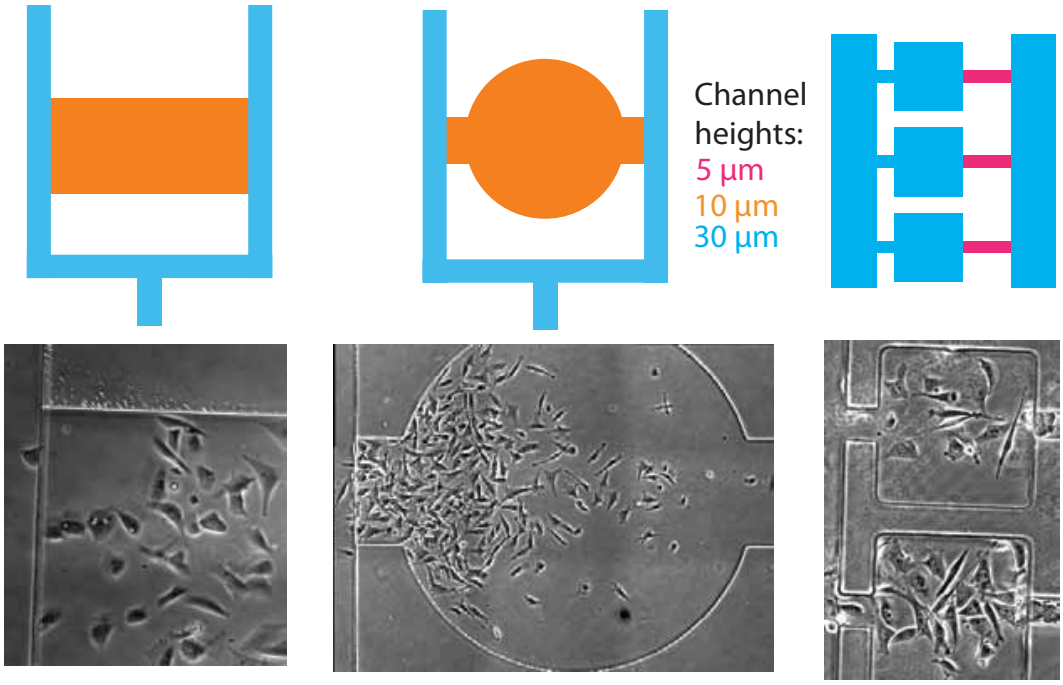

Figure 2.6: Cell trap designs for high-resistance to fluid flow. (A) A rectangular trapping region between two parallel perfusion channels will experience no pressure change to drive fluid flow if the individual pressures in each of the parallel channels are exactly the same. (B) Constricting the openings of the culture region and expanding the area in the shape of a circle further limits fluid flow. (C) A redesign with highly constricted trap entrance widths and a low-height perfusion barrier that prevents cells from passing through during loading. The width of the blue vertically parallel perfusion channels in all designs is 150 μm (design in C is magnified to better display the trapping regions)

Still convinced that higher resistance to fluid flow was needed, I contemplated ideas on how I could load cells into the square culture chambers of the latest design (Fig

2.6C) without the need for the low-height perfusion channel which currently served to allow fluid to enter the trap. Having read some literature on using degassed microfluidic devices to absorb fluid into isolated culture cavities (Luo et al., 2008), I got the idea of attempting to use a vacuum to load a fluid cell suspension into such a redesign of my latest device. I first attempted to degass the entire device and then load the cells as described by the aforementioned group, but I could not easily load cells because upon introducing a liquid suspension into the channels of the device the fluid would often precede the cells and load the traps immediately without any cells. What I needed was a way to precisely control the entry of fluid in time, and so I thought of simply connecting a vacuum line into the microfluidic channel that runs parallel to the square culture traps in Fig 2.6C but is now not fluidically connected (no purple perfusion channels). In this manner, I thought it would be possible to load a cell suspension into the device, cease the flow so that the cells would be sitting at the openings of the culture traps, then turn on the vacuum to evacuate air from the traps and bring in the fluid with cells. Indeed, I discovered that this was possible and this enabled a novel method of easily loading a desired number of cells into highly isolated culture traps.

2.4 Vacuum-assisted cell loading enables shear-free mammalian microfluidic culture

With the novel method of applying a transient on-chip vacuum within a specific air channel, it is possible to control the temporal and spatial distribution of gas exchange within the PDMS to allow localized wetting of chip components only when it is desirable to do so. Attempting to use external pressure to force fluid from the main channels into the chambers is ineffective due to the lack of an outlet for fluid or air inside each trap. However, the application of a temporary on-chip vacuum within an air channel adjacent to the cell chamber is sufficient to evacuate air from the chambers within 2 minutes due to the high gas permeability of PDMS. In this manner one can flow a high

density cell suspension into the main channel, stagnate the flow and then apply a vacuum to load cells in the chambers. Once captured in the traps, the cells are effectively shielded from the fluid flow in the main channel and remain undisturbed even at high flow rates. The complete culture platform incorporating the vacuum-loading method consists of 33 individual cuboid culture chambers (each has a 230 μm x 230μm footprint, 40μm height) adjoined to a main perfusion channel of identical height via a 50μm wide opening on one side of each chamber. The channel for application of a temporary vacuum runs parallel to the column of culture chambers at a distance of 160μm between the wall of this channel and the closest wall of each cuboid chamber (Fig 2.7). The Dial-a-Wave fluidic mixer joins to the main perfusion channel between port 2 and the first culture chamber and serves to deliver any desired waveform of biochemical inducer for dynamic stimulation of cells inside the culture chambers.

2.4.1 Cell seeding protocol and setup for long-term culture

For device loading and culture validation, HeLa cells and CHO-K1 cells were maintained in complete medium consisting of Dulbecco's Modified Eagle Medium and F-12K medium, respectively, supplemented with 10% fetal bovine serum (Gibco 10437) and penicillin/streptomycin(CellGro 30-002-CI) in a standard tissue culture incubator (Napco 8000WJ) at 37 degrees C and 5% CO_2. For device loading, cells are washed with dPBS, detached from the culture dishes with 0.05% or 0.25% trypsin EDTA for CHO-K1 or HeLa cells, respectively, centrifuged to form a pellet and resuspended in complete media at a density of 5-10 million cells per mL. A 3mL syringe connected to a one foot section of PTFE #24 AWG tubing interfaced via a 23-gauge sterile luer stub is used to first wet the device channels prior to cell loading as follows. All culture media for microfluidic use is passed through a 0.22μm filter (Millipore SLGP033RS) to remove debris. A small volume ($\sim$100μL) of complete media is aspirated into the end of the tubing by using the syringe and the tubing is then connected to port 5 of the device. Pressure is applied until fluid fills all of the ports except number 1. The

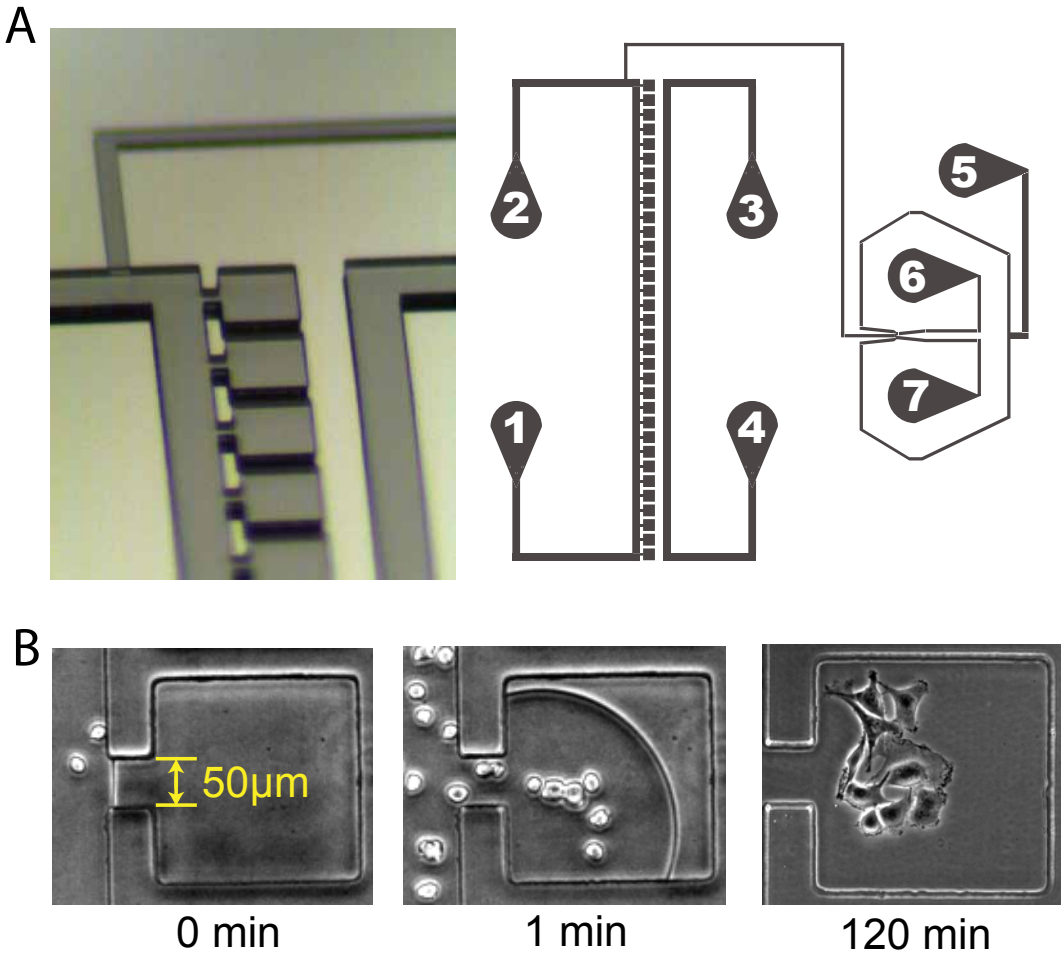

Figure 2.7: Device design and vacuum loading of cells. (A) Each of the 33 cuboid culture chambers is connected via a narrow opening to a main perfusion channel that runs between ports 1 and 2. A separate air channel between ports 3 and 4 allows the application of a temporary vacuum at the PDMS interface to draw fluid from the main perfusion channel into the culture chambers. Ports 5-7 comprise the DAW dynamic stimulation generator. (B) Upon application of a vacuum in the air channel at time zero, fluid containing cells is rapidly drawn into the culture chambers and fills the traps within 2 minutes, at which point the vacuum is turned off. HeLa cells attach and begin to spread out within 1-2 hours after loading during continuous perfusion culture.

tubing is then removed from port 5 and wet-connected to port 2 (a wet-connect means a fluid droplet from the tubing is connected to the fluid resting on top of a port prior to applying syringe pressure in order to ensure bubbles do not enter the system) (Young et al., 2006). Pressure is gently applied to fill port 1 and the device channels are now fully wetted with media, except for the culture traps which remain filled with air. A new one foot section of tubing is now attached to the same syringe to replace the old tubing, and a small volume of cell suspension is aspirated. The tubing is then connected to port 1 of the device. To prepare the vacuum connection, the house laboratory vacuum is interfaced with a 20 gauge luer stub using via 0.030" ID Tygon microbore tubing and the luer end is plugged into port 3 of the air channel. Port 4 is closed off by plugging in a luer stub fitted with a cap. The vacuum is initially OFF, and the cell suspension in the PTFE tubing is connected to port 1 and pressure is gently applied to the syringe until cells begin to fill the main perfusion channel. The flow is then stopped by ceasing to applying pressure at the syringe and the presence of a high density of cells in the main channel is confirmed visually under an inverted tissue culture microscope. At this point the vacuum is turned ON and the progress of cell loading into the culture chambers is visually monitored. Gentle tapping of the tubing containing the cells can enhance cell loading during this process by ensuring that cells move with the fluid flow into the traps rather than getting snagged on the entry-ways or due to the friction with the glass coverslip. Once the traps are completely filled, the vacuum is turned off and the line connections to the air channels are disconnected to relieve any remaining vacuum. It is now necessary to flush the untrapped cells out of the device. A new one-foot section of tubing is connected to the syringe and a small volume of complete media is aspirated and then the tubing is wet-connected to port 1 of the device. Pressure is applied to force cells in the main channel to flow out of the remaining ports of the device. Due to the extremely high resistance of the culture traps to convective flow, the cells there are effectively retained even during the high flow rate of this flush step. The device is now ready for experimental setup on a microscope stage for time-lapse imaging, or it can be precultured in a standard tissue culture incubator to allow cells to attach and proliferate

for a desired amount of time. To perform preculture, I have found that the easiest setup involved connecting PTFE #24 AWG tubing to a single syringe with complete media and wet-connecting it to port 1 of the device. Ports 2, 6 and 7 are closed OFF by putting a short (2") section of tubing into each port and tying off the end of the tubing into a tight knot to prevent fluid flow (it is easiest to tie the knot before plugging in the tubing). Finally, a section of tubing without a knot at the end is plugged into port 5 and the open end of this tubing is set so that its level in the z-direction is below the fluid level in the syringe. The entire setup is then placed in a tissue culture incubator for preculture up to two days. Due to the hydrostatic pressure difference between the fluid level in the syringe and the open end of the tubing in port 5, media will initially rapidly flow into the device and then a slow perfusion flow is established. Due to the microliter per hour volume flow rates of fluid emanating from the open end of the tubing in port 5, evaporation removes excess fluid that slowly leaks out of the tubing and perfusion flow is unhindered.

2.4.2 Culture chamber mass transport

The extremely high resistance to fluid flow from the main perfusion channel into the square culture chambers creates a shielding effect that protects the cells from any potentially detrimental shear stresses. The calculated mean fluid velocity in the culture chambers with a 50μm wide trap opening is $\sim$1/5300 of that in the main perfusion channel and this ratio remains constant for a large range of flow rates (Fig 2.8A) As a result, mass transport into the traps is dominated by diffusion with time-scales on the order of $\sim$15 minutes to reach an equilibrium concentration with the main channel for a small molecule such as Sulforhodamine 101 (Fig 2.8B).

Flow and diffusive transport within the device were modeled using the finite element method (COMSOL multiphysics 3.4). Flow velocities in the main channel and cell traps were calculated using the General Laminar Flow application mode within the microfluidics MEMS module by specifying a desired volumetric flow rate at the

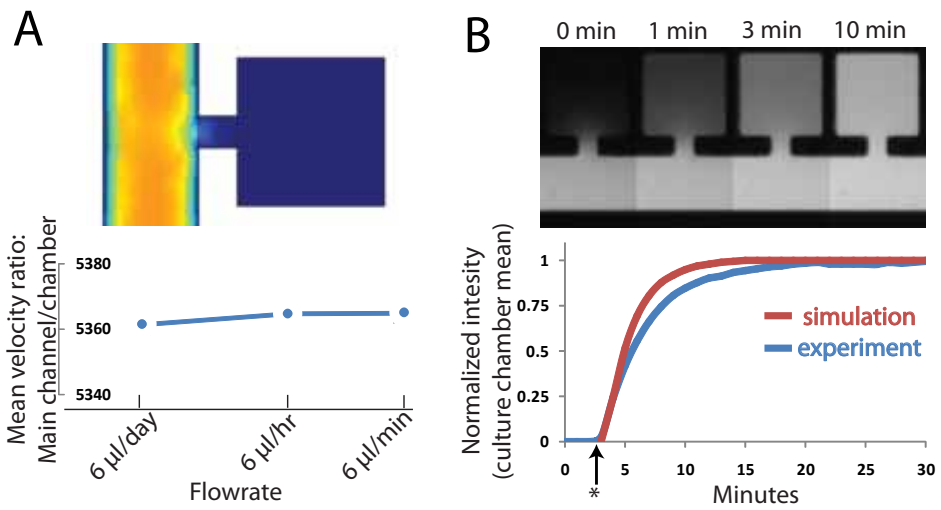

Figure 2.8: Cell trap mass transport characteristics. (A) Finite element modeling depiction of high resistance to convective transport into culture chambers (top). Mean fluid velocity inside the chambers is ∼1/5000 of that in the main channel for a wide range of flow rates (bottom).(B) Experimental validation of diffusion as dominant mode of transport using Sulforhodamine 101 fluorescent dye (top) and comparison to simulation with COMSOL (bottom). Star indicates time dye was added.

inlet (port 2) as a laminar inflow boundary condition and setting the outlet boundary condition (port 1) as zero pressure, no viscous stress. All other boundaries were set to the no-slip wall condition. The shallow channel approximation option was used to incorporate the channel heights. The DAW channels were excluded from this analysis to simplify the computation. Diffusive transport into the traps as a function of time was calculated using the transient analysis diffusion application mode within the COMSOL multiphysics convection and diffusion module. The inlet boundary condition was set to a fixed concentration and the outlet was specified as a convective flux boundary. A stationary general laminar flow solution was first computed and then used to compute the transient solution for the convection and diffusion module. A diffusion coefficient of 2.8 $\times$ 10^{-10} m^2 s^{-1} was used for Sulforhodamine 101 simulations (Hess and Webb, 2002). Experimental validation was performed with Sulforhodamine 101 (Sigma S7635) at a working concentration of 0.5 μg/mL.

Since many mammalian gene expression systems using small molecule inducers

are characterized by dynamics with half-lives on the order of several hours, the somewhat slow ∼15min diffusion time-scale should be generally acceptable. But if a faster rate of chamber turnover is required, I experimented with increasing the entrance width of the traps and found that it greatly enhanced mass transport while preserving the ability to vacuum load the traps. I tested trap openings of 180μm, 120μm, 80μm and 40μm width. All of them were easily loaded with cells, albeit the larger trap openings were more susceptible to losing cells during the flushing of the device due to the decreased resistance to flow in these chambers (Fig 2.9). These results demonstrate that the desired ratio of convective to diffusive transport for a specific application can easily be tuned with this culture trap design simply by modulating the width of the trap opening to the main perfusion channel.

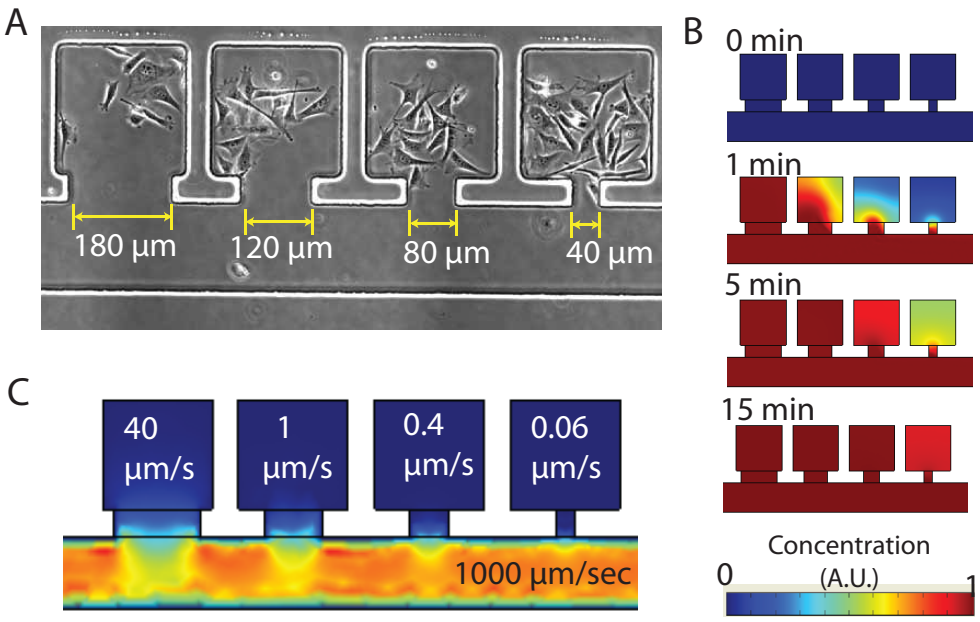

Figure 2.9: Tunability of mass transport. (A) Culture traps of various width openings are reliably vacuum-loaded with cells. Larger trap openings facilitate faster diffusion of small molecules (B) as well as a higher rate of convective flow (C).

2.4.3 Long-term culture and dynamic stimulation

To test the suitability of the microfluidic traps for long-term mammalian cell culture, I loaded devices with HeLa and CHO-K1 cells and monitored morphology and proliferation for up to four days under continuous perfusion at two different flow rates. For these experiments, I typically loaded less than 10 cells per chamber in order to allow sufficient space for growth over the course of each experiment. The loading density of each chamber can be controlled by modulating the density of the cell suspension in the main channel upon device loading. Perfusion experiments were carried out in chips that did not have the Dial-A-Wave network ports bored for fluidic connections as it was not necessary to have dynamic stimulation capability for these experiments. Furthermore, this allowed for precise control of the flow rates through the main perfusion channel by using a programmable syringe pump (KD scientific, model 210) to drive media flow from port 2 through the device and out to port 1. In order to culture the device at 37 degrees C and 5% CO_2 while maintaining a connection to the syringe pump, it was not possible to use a standard tissue culture incubator due to the inability to route fluidic tubing into the incubator (short of drilling holes through the walls/insulation). To remedy this, I built a simple and low-cost miniature tissue culture incubator using a consumer-grade egg incubator to maintain temperature and a home-made gas-flow regulator to bubble 5% CO_2 into the incubation space (Fig 2.10).

Fluidic connections from the ports of the device to syringes containing growth medium are established using 20 gauge PTFE tubing (Zeus Inc.) interfaced via 20 gauge stainless steel luer stub (McMaster) pins. I found that the use of a chemically inert material such as PTFE for the fluidic tubing connections was absolutely critical for successful mammalian microfluidic culture, as the use of commonly used Tygon microbore tubing proved to be cytotoxic in the case of perfusion culture. Similar reports of problems with Tygon microbore tubing exist in recent literature (Cooksey et al., 2011), indicating that the use of chemically inert tubing for this application is not yet well recognized and needs to be explicitly stressed in order to avoid extensive troubleshooting. I had been

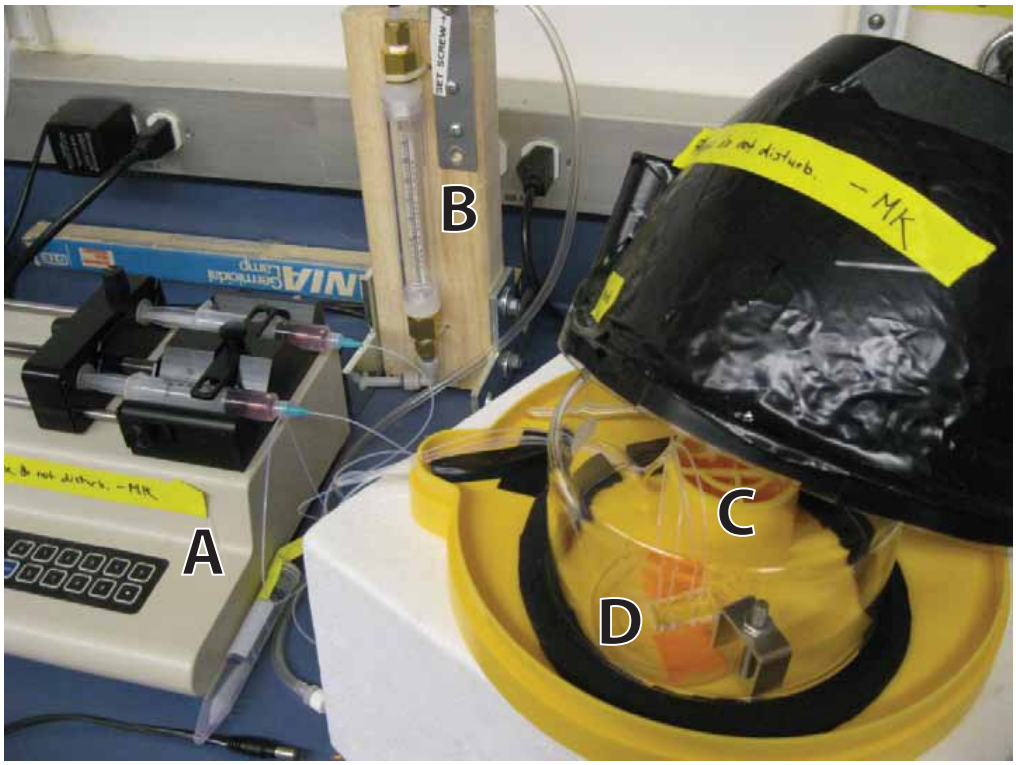

Figure 2.10: Custom incubator to interface with syringe pump. (A) The programmable syringe pump allows for the control of two syringes to maintain a precise flow-rate of culture medium to the devices inside the incubator. (B) A custom gas-flow regulator consisting of a flow meter (Gilmont Instruments GF-2160) coupled to a needle valve (McMaster-Carr 48965K14) allows fine-tuning of the 5% CO_2 flow rate (50mL/min) from a cylinder and regulator to the water bath in the central region of the incubator. (C) The egg incubator (Brinsea 6011260) consists of a yellow plastic base with a central water holding column to provide humidity and a heat source and sensor in the removable lid that has been covered with black electrical tape to prevent light from damaging the cells. (D) The two devices are taped to a 3cm culture dish which is held in place with a metal clamp. A glass enclosure dish (Pyrex 3140, 125 x 65 mm) surrounds the devices and sits on top of a black rubber seal to ensure the humidified CO_2 bubbling through the water column is retained.

using Tygon microbore tubing during the troubleshooting and development of my microfluidic designs mentioned prior to the vacuum-loading design, and I strongly suspect that cell viability would be significantly improved for many of those device designs if PTFE tubing was used. I suspect that Tygon microbore tubing does not perform well due to the relatively high gas permeability and associated changes in media osmolarity from evaporative losses and/or the leeching of plasticizers from Tygon tubing into the fluid media is detrimental to cell viability. For experiments using the vacuum-loading trap design I used PTFE tubing to make the fluidic connections. Hela and CHO-K1 cells types exhibited healthy morphology for all experiments and fully colonized the uncoated glass surface of each culture chamber within a few days (Fig 2.11)

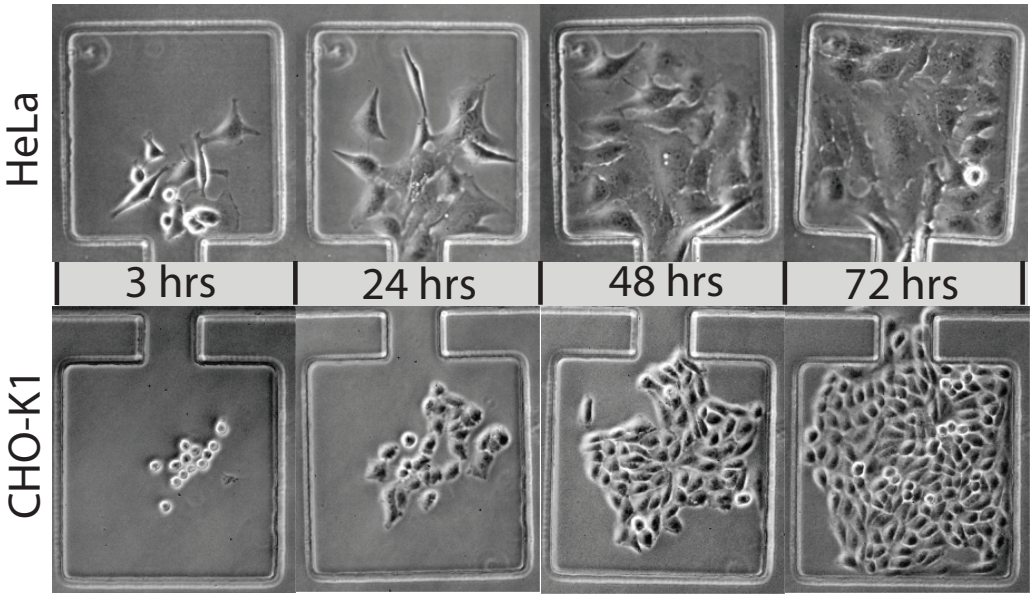

Figure 2.11: Long-term microfluidic cell culture. After initial vacuum loading into the culture chambers, HeLa and CHO-K1 cells rapidly colonize the glass growth area of the device during continuous media perfusion.

Specific growth rates for both Hela and CHO-K1 cells were somewhat lower in perfusion microfluidic devices than in traditional culture (Table 2.1), an observation that has been previously reported (Yu et al., 2007) and is most likely associated with con-

stant washing away of soluble autocrine growth factors during perfusion culture. Both cell types exhibited little change in growth rate between the two flow rate conditions (5 and 25 μl per hr). The robust growth and colonization of the device culture chambers by these cell lines indicates that application of a temporary on-chip vacuum during loading is not detrimental to cell viability or proliferation and is a novel useful method for delivering cells in suspension into isolated chambers within a microfluidic device. A unique feature of this on-chip vacuum loading method is that the addition of multiple

Table 2.1: Comparison of microfluidic and bulk culture characteristics. Perfusion microfluidic culture achieves comparable growth rates to traditional static culture.

Culture format	Culture area (cm^2)	Media flow	Specific growth rate (avg $\pm$SD*) CHO	HeLa
6-well plate	9.5	Static	1.129 $\pm$0.024	0.455 $\pm$0.009
device	0.017	5 μl/hr	0.910 $\pm$0.012	0.323 $\pm$0.028
		25 μl/hr	0.885 $\pm$0.002	0.342 $\pm$0.001

* n=2

vacuum channels throughout various areas of a chip design enables those areas to be individually addressed in terms of fluid loading in space and time. I have confirmed this by creating traps on either side of a main fluid channel, each trap with its own vacuum channel running in parallel, to allow for loading each trap at different times. This feature opens up the possibility of selectively loading different traps in the same fluidic channel with unique cell populations without the need for complex valves and on-chip flow control devices that would normally be required to address different portions of the same interconnected fluidic network. Such capability may be useful not only for comparison of two different cell populations seeded along the same fluidic channel but also for cell signaling studies in which two different cell types are loaded separately into traps on either side of the main fluid channel and modulation of flow rate is used to control the communication across the channel by soluble secreted factors.

Since one of the primary advantages of microfluidic technology is precise control of the cellular microenvironment, I confirmed the ability to dynamically stimulate

the cells in the culture chambers using the Dial-A-Wave function generator fluidic network. I used a 3t3 fibroblast reporter cell line which expresses destabilized GFP from a hybrid promoter co-regulated by the tet-transactivator and tet-transrepressor (see Chapter 5 for details of how I constructed this cell line) in response to doxycycline (DOX), an analogue of tetracycline. The cells were vacuum loaded into the device and pre-cultured with perfusion flow in the tissue culture incubator for 24 hours prior to setting up the device on the microscope stage for time-lapse imaging. In principle, the DAW function generator allows any waveform to be delivered to the cells, but for simplicity of observing the cell-response I delivered a square wave of 10ug/mL doxycycline with a period of 24 hours (12 hours ON, 12 hours OFF). Due to the destabilized nature of the reporter I could observe production and degradation of GFP that was roughly in line with the induction cycles (Fig 2.12). The successful long-term dynamic stimulation of cells using our novel trap design coupled to the Dial-a-Wave function generator demonstrates the effectiveness and ease-of-use of this platform as a means of probing the cellular response to any desired waveform of input stimulus.

2.4.4 Fabrication and device preparation

All of the device designs are fabricated by first generating a master mold of the features on a silicon wafer by way of layer-by-layer photolithography and then pouring and curing a polydimethylsiloxane (PDMS) replica onto the master mold which is then peeled off and finally bonded to a glass coverslip. Negative SU8-2000 photoresists (Microchem Corporation) are used according to established methods (Ferry et al., 2011) to create the master mold. Table 2.2 summarizes the specific fabrication steps particular to the vacuum-loading microfluidic culture platform discussed in this chapter. Briefly, the designs for each feature layer are drafted in AutoCAD and sent to CAD/Art Services, Inc. (Bandon, Oregon) for printing of the photomasks which are then affixed to borosilcate glass plates (McMaster 8476K131) using Loctite 495 instant adhesive. For each layer, photoresit is deposited onto the wafer using a Headway PWM32 programmable

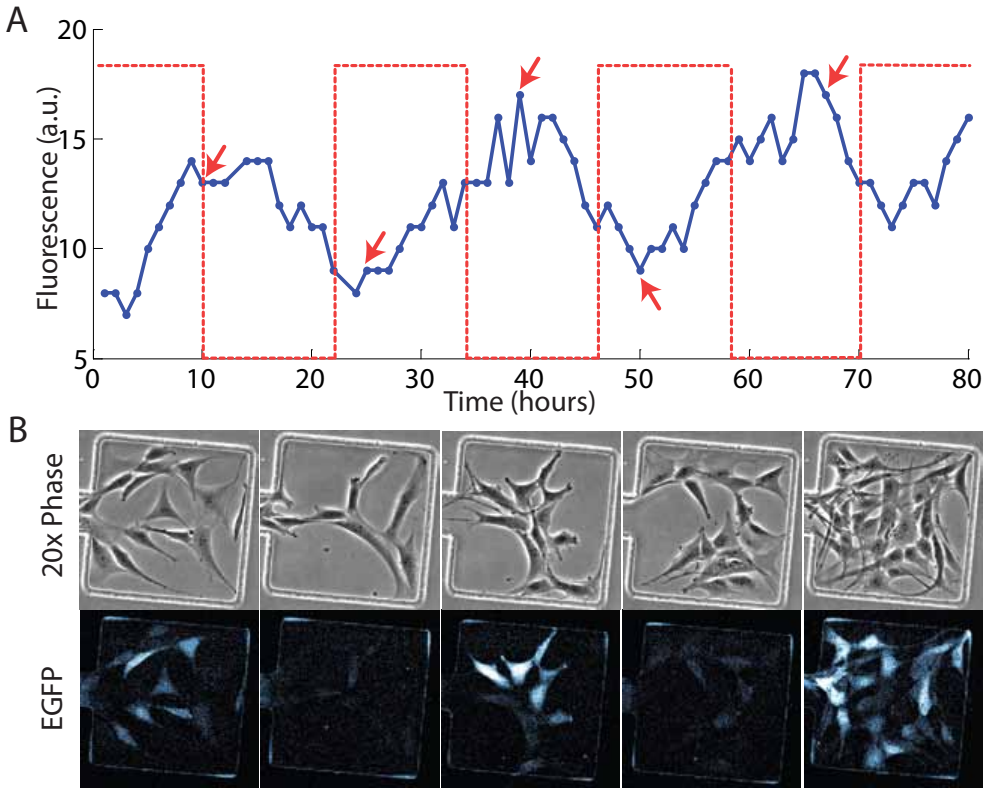

Figure 2.12: Dynamic stimulation of a fluorescent reporter cell line. (A) The DAW fluidic mixer was used to induce cells with 10μg/mL of doxycycline for 12 hour periods (dashed line) every 24 hours [imaging was initiated 2hrs after the start of the 1^{st} induction cycle]. Mean fluorescence of all cells in the chamber shown is plotted as a solid line. (B) Each of the image columns corresponds to the peaks and troughs of the fluorescent signal trace as indicated by the arrows in the time-lapse data in (A).

Table 2.2: Microfabrication process overview. The fabrication of each layer consists of spinning photoresist at a prescribed speed to deposit a desired height, followed by baking and UV crosslinking.

Layer	Height	Resist	RPM	PB, 65°	SB, 95°	Exposure	HB, 95°
DAW channels	15μm	2015	3300	1 min	3 min	150 sec	4 min
chaotic mixers	5μm	2005	3000	1 min	2 min	120 sec	3 min
main channels	40μm	2015	1000	2 min	4 min	2 doses, 120 sec ea.	10 min

RPM is rotations per minute, PB is pre-bake, SB is soft-bake, Exposure refers to UV crosslinking, HB is hard-bake

spinner set to the appropriate RPM to achieve the desired height. The wafer is then baked at a prescribed temperature and time to harden the resist and then placed on an HTG 84-3 Mask Aligner for aligning of the photomask and expsure to UV to crosslink the features. An additional baking step follows prior to developing the un-crosslinked photoresist. Feature heights are confirmed using a Dektak 150 Stylus profilometer and the wafer is finished by depositing chlorotrimethylsilane release agent for 5 minutes in a vacuum dessicator at $\sim$-1atm. The PDMS replica is then generated by mixing Sylgard 184 Elastomer curing agent and base (DOW corning) in a 1:10 ratio, degassing it for 30 minutes under vacuum, pouring onto the master mold wafer and curing for 1 hour at 80 degrees C. After allowing to cool, the finished PDMS stamp is carefully peeled from the wafer and autoclaved for 30 minutes at 121 degrees C to ensure long-term viability of cells in the devices (Chiu et al., 2000).

Holes for the fluidic ports are punched using a 16 gauge sharpened luer stub (Mcmaster Carr). The use of a sharpened punch to bore the fluidic ports is particularly critical to mammalian microfluidic culture because it prevents tears and other imperfections in the PDMS which act as nucleation points for bubble formation which is severely detrimental to cell viability and proper device perfusion (Kim et al., 2007). Furthermore, it reduces the creation of PDMS shavings that act as debris that often clogs the low-height channels of the DAW. Once all the ports are punched, they are flushed with

isopropanol and DI water to remove any such debris. The clean devices are subsequently bonded to cleaned glass coverslips (Corning 2940-244) via oxygen plasma exposure (Jelight UVO cleaner Model no. 42, 0.6 scfm O_2, 3 minutes). Coverslips are cleaned with methanol, ethanol and DI water which is sufficient to ensure good bonding, but if extra-clean coverslips are required an RCA standard clean 1 solution is recommended. For this procedure, NH_4OH, $30\%H_2O_2$ and DI water are mixed in a 1:1:5 ratio, brought to 75 degrees C and coverslips are submerged for 15 minutes to remove any organics by oxidative dissolution.

2.4.5 Experimental setup

For long-term cell growth experiments using the custom incubator described earlier in this chapter, PTFE #24 AWG tubing is directly interfaced with the fluidic ports of the device to deliver perfusion media. For time-lapse experiments on the microscope stage, the device is affixed to the stage and covered with a small shallow atmospheric chamber (In-vivo Scientific) to deliver humidified CO_2. This requires the tubing connections to the device to make a sharp 90° angle, and so a wider diameter tubing (PTFE #20 AWG) is used along with 20 gauge luer stub pins bent to 90°. This tubing is connected to 60mL syringes which are set to the appropriate heights to achieve the desired flow rates through the device via hydrostatic pressure. In reference to the microscope stage, DAW inputs (ports 6 and 7) are set to 23 inches above this level, the DAW shunt (port 8) is set to 18 inches, and the main channel syringe (ports 1 and 2) is set to 8 inches. The fluidic connections from ports 1 and 2 are combined via a Y-junction (Ziggy's Tubes and Wires, Inc.) to a single syringe to ensure that these ports are at exactly the same hydrostatic pressure to ensure that flow from the DAW enters the main channels and flows out of the device via both ports 1 and 2. If the Y-junction is not used, it is difficult to maintain equal pressures at ports 1 and 2 during the course of a long-term experiment, which can lead to a situation where one of the main ports backflows into the device and dilutes or eliminates the DAW signal.

Time-lapse phase and epifluorescent imaging was performed using a Nikon Ti-Eclipse inverted microscope fitted with a CoolSnap HQ^2 camera (Photometrics), a motorized stage (ProScanII, Prior Scientific) and a Lumen 200 fluorescent light source (Prior scientific). Automation of image acquisition was controlled with NIS-Elements software. For experiments not requiring frequent acquisition every few minutes, image capture was performed using a Nikon DX40 digital SLR camera connected to a Nikon Diaphot inverted microscope fitted with a 20x Phase ELWD objective.

2.5 Acknowledgements

Chapter Two contains material submitted for publication as Kolnik, M., Tsimring, L.S., Hasty, J., 2012: Vacuum-assisted cell loading enables shear-free mammalian microfluidic culture. *Lab on a Chip*.

Chapter 3

NF-κB signaling in a dynamic microfluidic environment

3.1 Introduction

Nuclear factor-kappa B (NF-κB) signaling is an extensively studied topic with over 35,000 publications describing this highly conserved collection of transcription factors which are involved in the regulation of various biological processes such as cell immune and inflammatory response, cell survival, and cell type maturation (Hayden and Ghosh, 2011; Zhu and Fu, 2010). The conserved family of NF-κB proteins can be traced as far back as the phylum *Cnidaria* (a diverse group of aquatic animals), although the proteins appear to have been lost from notable model organisms such as *S. cerevisiae* and *C. elegans* (Gilmore, 2006). For the past 25 years, NF-κB has served as a model for inducible transcription factors that respond to external stimuli by rapidly generating both transient and sustained changes in gene expression (Hayden and Ghosh, 2012). During a resting unstimulated state, NF-κB dimers are bound to and sequestered in the cell cytoplasm by IκB proteins. Upon induction by an external stimulus, a complex called IκB kinase (IKK) phosophorylates the IκB proteins targeting them for degradation. Thus, NF-κB is released and translocates into the cell nucleus where it binds DNA

along 9-10 base pair κB sites to regulate the expression of a variety of target genes, including the resynthesis of IκB proteins which act to resequester the NF-κB dimers back into the cell cytosol.

Historically, distinct modes of NF-κB activation have been classified into the canonical (classical) and non-canonical (alternative) pathways, depending on the specific dimers involved and the particular components involved in the signaling cascade. The NF-κB functional transcription factors exist as homo- or heterodimers of five possible NF-κB proteins in mammals: RelA(p65), RelB, c-Rel, p50 and p52. The dominant dimer in many cells and hence the most studied is the p50-RelA heterodimer involved mainly in the cannonical pathway of NF-κB activation. The canonical pathway is activated by the binding of a variety of stimulatory ligands (cytokines) to their respective receptors on the cell surface (such as the Tumor Necrosis Factor Receptor, Interleukin-1 Receptor, Toll-like receptor4, etc.) which then recruit adaptor proteins (such as TRAFs and RIP) to associate closely with the members of the IKK complex, including IKKα, IKKβ and a regulatory protein called NEMO. This leads to the aforementioned activation of the IKK complex that eventually leads to the release of NF-κB into the nucleus. The non-canonical pathway is activated by a specific subset of cytokines in the TNF family (such as CD40 and lyphotoxin B) and deals largely with the p100-RelB heterodimer during B- and T-cell organ development. A primary difference in the non-canonical signaling cascade is that it preceeds through an IKK complex with two alpha subunits but operates independently of NEMO (Scheidereit, 2006). Activation of IKKα proceeds through the protein NF-κB inducing kinase (NIK) which leads to the phosphorylation of p100, the processing of which releases p52-RelB dimers that enter the nucleus and activate genes involved in organ development. Although the canonical and non-canonical pathways were previously though to be largely independent (Pomerantz and Baltimore, 2002), recent evidence suggests that there exists significant crosstalk between the two cascades (Shih et al., 2010).

While there has been significant progress in the NF-κB field by characterizing the myriad of molecular players and developing computational models to describe

the connectivity of the various components of the pathway, we are just beginning to scratch the surface in terms of exploring the dynamic behavior of the NF-κB pathway (Gilmore, 2006). Dynamic behavior in the form of NF-κB activity oscillations was initially observed by whole-cell population assay and corresponding computational models (Hoffmann et al., 2002), but population-based measurements tend to obscure the exact dynamics occurring in single-cells, making it difficult to draw precise conclusions regarding the detailed character of such oscillations (whether they are rapidly damped or instead sustained and un-damped, for example). To answer these questions, live single-cell time-lapse imaging has enabled observations of fluorescently labeled NF-κB dynamics in individual cells. Such initial experiments by Nelson et al. (2004) confirmed the presence of NF-κB nuclear localization oscillations in single cells and proposed that these oscillations maintain NF-κB dependent gene expression during continuous stimulation of the system with TNFα. This raised some debate as to whether sustained oscillations of NF-κB are physiologically relevant in-vivo rather than a by-product of genetically engineered manipulations necessary for fluorescent visualization in live-cells (Barken et al., 2005; Nelson et al., 2005). In other words, is it the case that the frequency encoding of un-damped NF-κB oscillations plays a significant role in controlling downstream gene expression, similar to other signaling systems such as calcium translocation (Berridge et al., 2003)? As more single-cell studies were carried out (Friedrichsen et al., 2006; Ashall et al., 2009), the results seemed to support the idea that sustained NF-κB oscillations play a critical role in the regulation of this pathway. One of the original criticisms of the studies reporting sustained oscillations focused on whether the transiently transfected fluorescent cell lines were an accurate representation of native cellular dynamics. To address these concerns, Lee et al. (2009) created an NF-κB reporter cell line which has the native RelA/p65 knocked out and stably replaced with a lentiviral construct that uses the native RelA promoter to drive the expression of the fluorescent fusion protein p65-dsRED. The authors used this 3t3 mouse fibroblast cell line to observe the single-cell NF-κB response to TNFα and LPS to further characterize the oscillation dynamics of nuclear translocation.

In a follow-up study, the authors greatly expanded upon the single-cell analysis approach by using a microfluidic platform to parallelize the experimental setup to obtain thousands of individual cell trajectories of NF-κB in response to various stimulation levels of TNFα (Tay et al., 2010). The use of microfluidics allowed for the precisely timed delivery of TNFα pulses to stimulate cells growing in designated culture chambers of the device. Microfluidic valves were closed off immediately after stimulation to isolate the culture chamber from any subsequent media exchange and thus the cells in this device remained bathed in the initial volume of media containing TNFα for the entire duration of each experiment. This pioneering study highlights the potential power of microfluidics coupled with live-cell imaging to aid in the elucidation of signaling dynamics in pathways such as NF-κB. In this chapter, I discuss the use of the microfluidic platform developed in chapter two to probe the response of the NF-κB signaling pathway to dynamic stimulation.

3.2 Microfludic stimulation of NF-κB signaling with gradually increasing TNFα input

Tumor necrosis factor alpha (TNFα) is a cytokine produced predominantly by macrophages during immune stress and inflammation and it can generally be thought of as a proinflammatory mediator, although it also has the capacity to induce apoptosis and other bioactivities (Wajant et al., 2003). In its active form, TNFα exists as a soluble homotrimer that has been released by proteolytic cleaveage from its initial localization within the cell membrane (Black et al., 1997). At low concentrations below the nanomolar range, the soluble trimer tends to dissociate into the inactive monomer form. TNFα activates the canonical NF-κB signaling cascade by binding to cell-membrane TNF receptors and causing them to re-assemble by interacting with various proteins (SODD, TRAF2, TRADD and RIP) which eventually leads to activation of the IKK complex and subsequent release of NF-κB into the nucleus (Jiang et al., 1999; Hsu et al., 1995, 1996;

Wajant et al., 2001) (Fig 3.1).

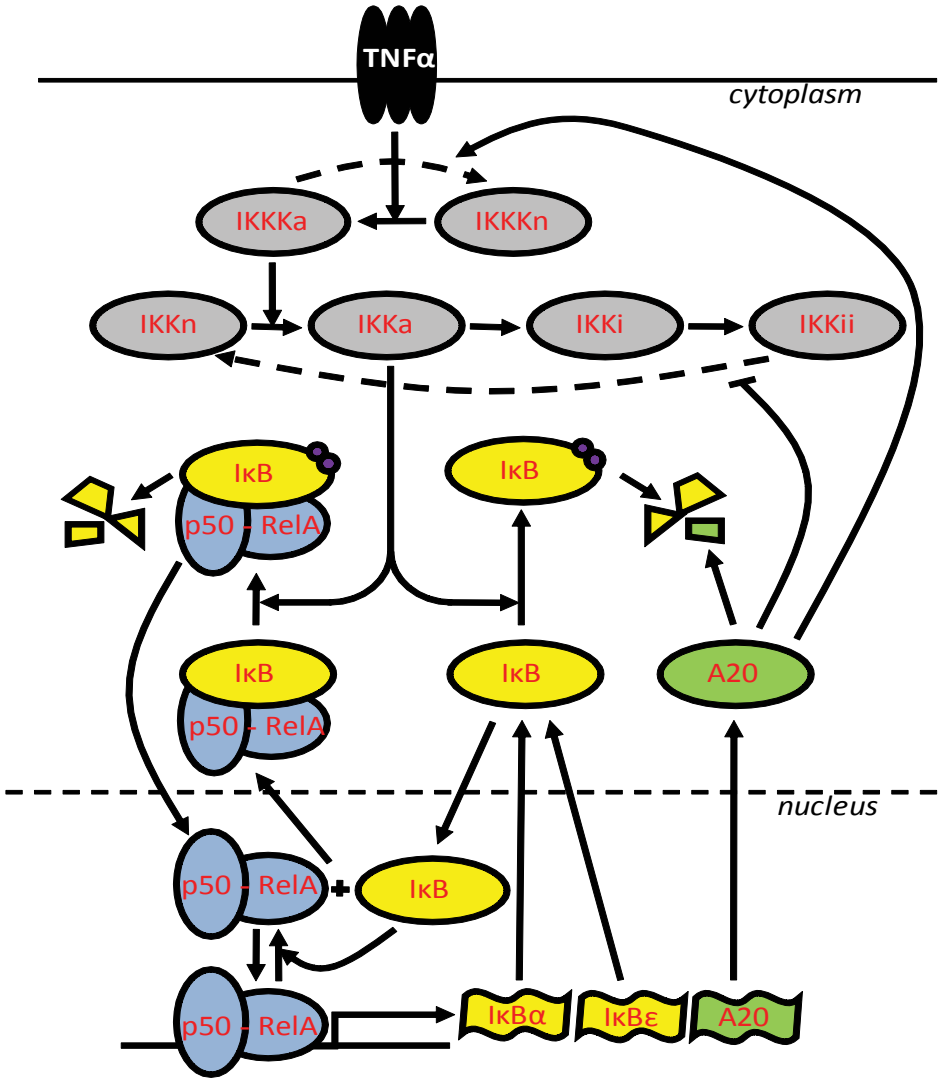

Figure 3.1: Activation of canonical NF-κB signaling cascade by Tumor Necrosis Factor alpha

Most tissues express TNF type 1 receptors which appear to be the dominant form of mediating TNFα signaling. (Wajant et al., 2003). Cells in their native environment in-vivo are typically exposed to a gradually increasing TNFα level that reaches a maximum with a few hours after immune stress upon infection (Chung et al., 1991). However, virtually all experiments characterizing the TNFα-induced activity of NF-κB

have exposed cells to a discontinuous step function of the inducer, simply because there has been no easy way to replicate a gradual induction scheme in macroscale culture. With our novel microfluidic culture platform for dynamic stimulation we were able to expose cells to a gradually increasing TNFα concentration which most closely replicates the in-vivo mode of induction. Comparison of the individual cell trajectories of NF-κB response to the two modes of induction (ramp versus step) provides novel insights into the dynamic behavior of this signaling pathway.

3.3 Experimental setup

To observe the NF-κB response at the single-cell level, I carried out experiments using a cell line developed and kindly provided by Lee et al. (2009) which contains a fluorescent fusion protein p65-dsRED for visualization of the cytoplasmic-nuclear translocation (Fig 3.2). This cell line was constructed by infecting a $p65^{-/-}$ mouse fibroblast (3T3) line with a lentiviral construct expressing the fusion protein from an endogenous p65 promoter and then selecting a cell clone with p65 protein levels comparable to wild-type. Furthermore, the modified cell line also expresses a histone H2B-GFP fusion protein to allow for fluorescent visualization of the nucleus for automated cell tracking during image processing (Chung et al., 1991). For simplicity of nomenclature, I henceforth refer to this double-fluorescent cell line as H2B cells. Microfluidic experiments using this cell line were carried out using the mammalian DAW (mamDAW) device described in chapter two, with minor device and protocol modifications to accommodate for the slow diffusion of a large molecular weight inducer such as TNFα and the particular behavior of mouse fibroblasts within the device culture chambers.

To allow for rapid diffusion of TNFα into the culture traps during induction, the ceiling height of the traps was increased to 160μm (Fig 3.3A). The additional fabrication step to deposit this layer used SU8-2025 resist spun at 900 RPM. The resist was then pre-baked for 5 mins, soft-baked for 20 mins, exposed twice to UV for 120 seconds (2 min rest period in between) and then finally hard-baked for 10 minutes. This ceiling height

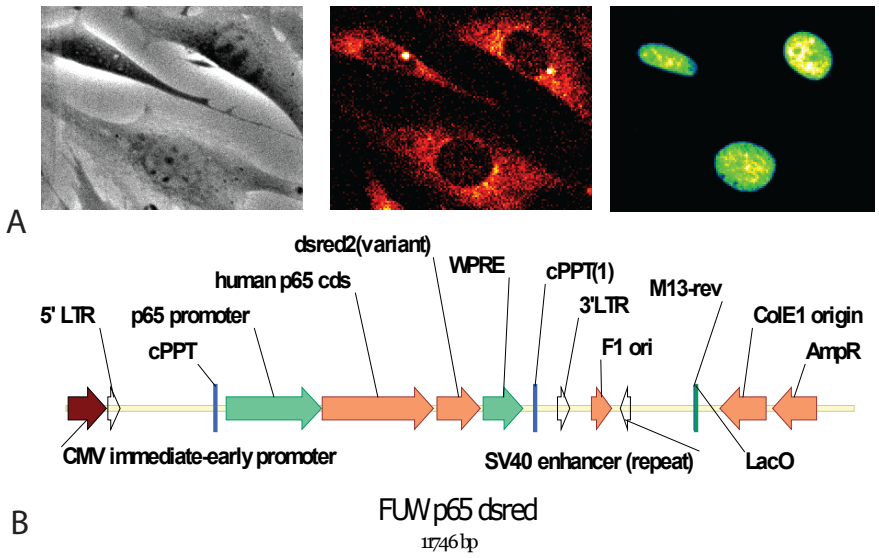

Figure 3.2: NF-κB reporter cell line. (A) Phase and fluorescent images at 20x magnification. p65-dsRED is well localized to the cytoplasm in unstimulated cells (red channel) while H2B-GFP is exclusively within the nucleus (green channel). (B) Plasmid map of the FUW lentiviral vector containing the p65-dsRED fusion protein expressed using a 1.5kb segment of the endogenous p65 promoter (Lee et al., 2009).

modification created a diffusion sink at the top of each culture chamber to drive rapid and uniform TNFα distribution across the bottom area of the culture chamber containing the adherent cells (Fig 3.3B). Since we were only interested in a single exposure of cells to TNFα, we were not concerned with the relatively long time it would take to wash TNFα back out of the culture chambers as a result of the increased volume of fluid above the cells. With this device modification, all cells within the culture chamber responded at the same time to a stepwise stimulation, confirming the functionality of the diffusion sink principle.

Unlike HeLa and CHO-K1 cells which readily attach to and spread on a bare glass coverslip surface within the device, the H2B cells showed weak adhesion and poor spreading on uncoated glass. This required coating of the glass with fibronectin (FN), a glycoprotein component of the extracellular matrix which promotes cell adhesion. The coating is performed as follows. Fibronectin (Sigma F1141) is diluted 1:40 in PBS to a concentration of 25μg/mL. A 3mL syringe connected to PTFE #24 AWG tubing (1

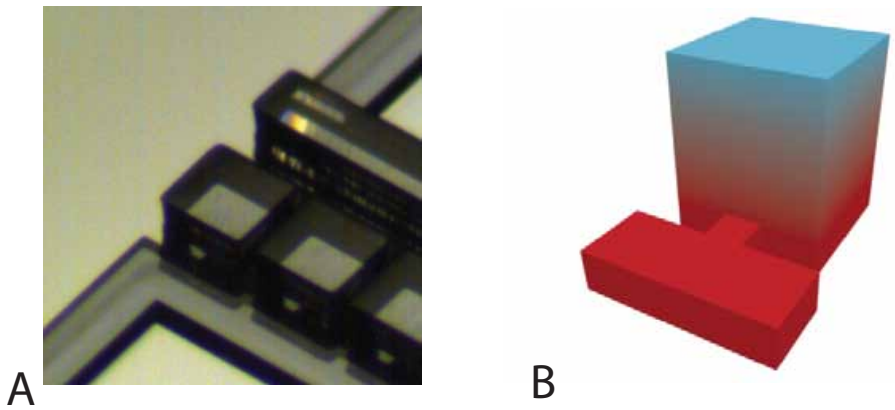

Figure 3.3: Culture chamber ceiling height modification. (A) Profilometer image of the 160μm high culture chambers. Note that the height of the adjacent air channel for application of vacuum was also increased. (B) Conceptual render of diffusion sink principle. TNFα (red color) delivered in the main channel rapidly covers the bottom of the culture chambers (where adherent cells are present) due to the diffusion gradient driven by a zero concentration of TNFα at the ceiling of the chamber (blue color).

foot section) via 23 gauge luer stub is used to aspirate a small volume ($<$40μL) of the fibronectin/PBS solution into the open end of the tubing. The tubing is then plugged into port 2 of the device and gentle syringe pressure is applied to flow the FN solution into the main perfusion channel alongside the 33 culture chamber traps but not so far as to reach port 1 of the device (in order to prevent subsequent clogging of this port with cells settling after loading). Once the main channel is filed with the FN solution, a vacuum is established in the air channel as described previously and the traps are filled with fluid. FN is allowed to adsorb in the device for a minimum of 1 hour at 4°C, and the fluid is subsequently aspirated out of the traps by attaching a fresh vacuum line to port 1 or 2 of the device. As a sidenote, the concentration of fibronectin used for this application was empirically determined by testing a range of values and noting that higher FN concentrations promoted unwanted cell adhesion to the PDMS sidewalls and ceiling, while lower FN concentrations failed to provide adequate adhesion and cell spreading.

Cell loading is performed using vacuum loading of the culture traps as described

in chapter two. The larger volume of the culture chambers due to the increased ceiling height of 160μm leads to a longer fluid filling time of the traps, which increases the number of cells brought into the chambers during loading. Hence, a lower initial cell loading density can be used, typically on the order of 2 million cells per mL. For the H2B cell line, an optimal loading density of 10-15 cells per culture chamber leads to adequate cell spreading and proliferation without overcrowding, which leads to cells crawling on top of each other and obscuring the nuclear signal. The high motility of fibroblasts compared to HeLa and CHO-K1 cells proved somewhat problematic, as the fibroblasts would rapidly move about the culture area after attachment and many of the cells would exit the culture trap, presumably in search of higher nutrient concentrations in the main perfusion channel. To deal with this particular behavior, it was necessary to preculture the loaded devices in a standard tissue culture incubator for approximately 36 hours prior to starting a time-lapse experiment in order to allow for some cells to crawl out of the culture traps while others remain in the trap and fully colonize the surface area there. This preculture is performed by using a simple scaffold to hold up a single media syringe for perfusion of the device and setting up the microfluidic chip such that a continuous perfusion flow is established through the main channel (Fig 3.4). Specifically, the media syringe tubing is plugged into port 1 of the device and ports 2, 6 and 7 are closed off to direct flow to port 5 to exit the device. Ports can be easily closed off by plugging in a short segment (2 inches) of tubing with a knot tied off at the end to prevent flow. Also, two ports can be connected with one segment of tubing to effectively close them off. Finally, port 5 is fitted with a 2 inch segment of tubing and the end is left open to the atmosphere, approximately 0.5 inches below the fluid level of media in the syringe. In this manner, a rapid perfusion flow is initially established to fill the tubing from port 5 with fluid, but within a few minutes, the height difference between the top of the tubing and the syringe fluid level is achieved and this drives a continuous slow perfusion flow suitable for multiday culture in the incubator.

Once the culture chambers of the device have been fully colonized with cells the chip is ready for a time-lapse imaging experiment. As soon as the device is initially

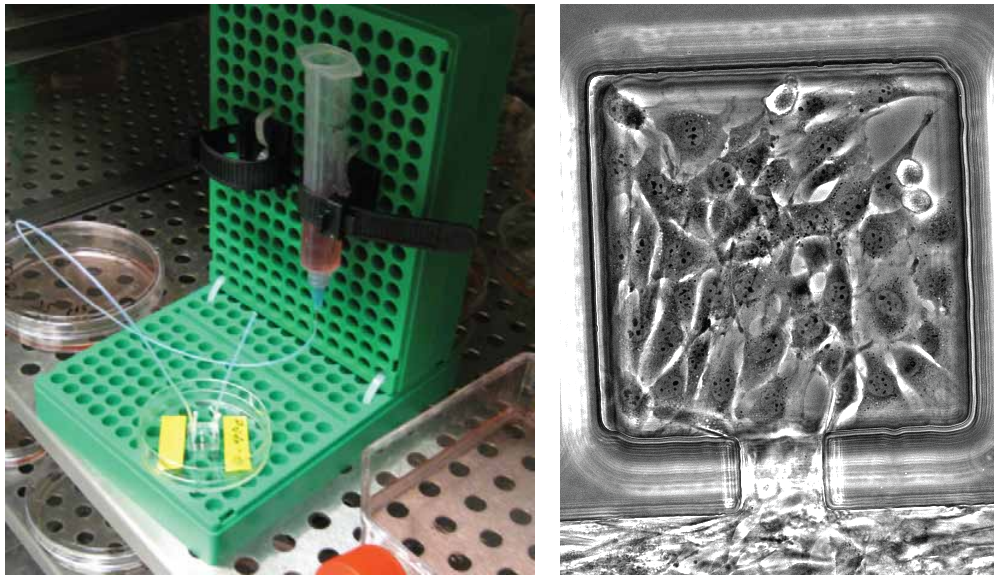

Figure 3.4: Perfusion pre-culture of fibroblasts in standard incubator. (A) A simple scaffold is readily constructed using plastic pipette holders (green) and zip-type syringe holders (black) which are held together with plastic zip ties (white). (B) Fibroblasts loaded into the culture chambers tend to migrate into the main channel and 1-2 days of pre-culture ensures the cells remaining in the trap fully colonize the surface area within the traps.

secured to the microscope stage, ports 1 and 2 are wet connected to fluidic lines that join via a Y-junction to a single syringe with filtered culture media. The device is then allowed to fill with fluid to ensure all bubbles that accumulated during pre-culture are pushed out of the DAW ports (the tubing stoppers are now removed to allow for this). Once fluid droplets are visible at the top of each DAW port, one can proceed to connect the DAW blank media and shunt ports. It is critical to allow fluid to properly fill the DAW channels during these experiments as the presence of a bubble during setup can block one of the channels of the DAW mixer and cause premature delivery of TNFα to the cells. To avoid this pre-stimulation altogether, the DAW port with TNFα inducer is only plugged into the chip while port 2 of the main channel is temporarily unplugged. This ensures all fluid from the DAW exits the chip via port 2 and does not reach the cells. In this manner, the DAW mixer can be calibrated from 0 to 100 percent and then set to zero (no TNFα going to cells) just before port 2 is carefully plugged back into the device (any disturbance of the fluidic lines at this point introduces turbulent mixing which can deliver TNFα to prematurely stimulate the cells). After all the ports have been connected in this way, the atmospheric chamber is gently set on top of the stage without disturbing the device and image acquisition can begin.

For each experiment, 25-30 culture chambers are chosen for imaging at 20x magnification. For our particular setup using the Coolsnap HQ^2 camera and Nikon 20x Plan Fluorite Long-working distance objective, the field of view (FOV) is roughly 420μm wide by 310μm high. This allows the imaging of one culture chamber withing a single FOV and thus a typical experiment will acquire 25-30 XY positions. At each position, a software-based autofocus routine is set to acquire phase images through a z-range of 24μm in 2μm steps, and the image at the z-position with the highest contrast is acquired and saved. This routine takes approximately 10 seconds to run, after which the red and the green flourescent channels are acquired (200ms and 20ms exposures, respectively). Hence, the imaging of 30 positions can be performed every 6 mins. Given the time-profile of NF-κB response reaches an initial maximum within 30-45 minutes of stimulation and oscillates with a 60-80 min period, this sampling period of 6 mins

is more than adequate to allow full reconstruction of the NF-κB signal. To track the delivery of TNFα, a cyan fluorescent dye (ATTO 425, 0.1μg/mL working conc.) is used in the media containing the inducer. For each experiment, a fresh 10μg/mL aliquot of TNFα (Calbiochem #654245) is thawed and diluted to the desired induction concentration in media containing the ATTO dye and the syringe is immediately plugged into the device during DAW calibration. At this point the TNFα is rapidly warmed to 37° and the precise time this occurs for each experiment is recorded. Images of the dye signal are captured at the DAW mixer as well as in front of the first and last culture chambers imaged during the experiment.

3.4 Image analysis

Extraction of NF-κB signal trajectories is performed with automatic tracking of individual cell nuclei using custom software developed in MATLAB. Briefly, the images in the green fluorescent channel are used to identify nuclear boundaries within each cell by virtue of the fidelity of nuclear localization of the H2B-GFP fusion protein (Fig 3.5). Nuclear overlap between successive images is then used to track cells from frame to frame. The red fluorescent channel images (p65-dsRED) are overlaid with the mask of nuclear outlines in order to measure the median intensity of the nuclear p65-dsRED signal and this value is linked between successive images using the tracking information to generate nuclear NF-κB signal trajectories for each unique cell. The raw trajectories are then automatically processed to eliminate those that meet any of the following criteria:

(a) trajectory starts after TNFα stimulation has already begun

(b) nuclear area changes by more than 50% between successive frames

(c) nuclear GFP fluorescence changes by more than 50% between successive frames

(d) trajectory ends within 3/5 of the length of TNFα stimulation duration

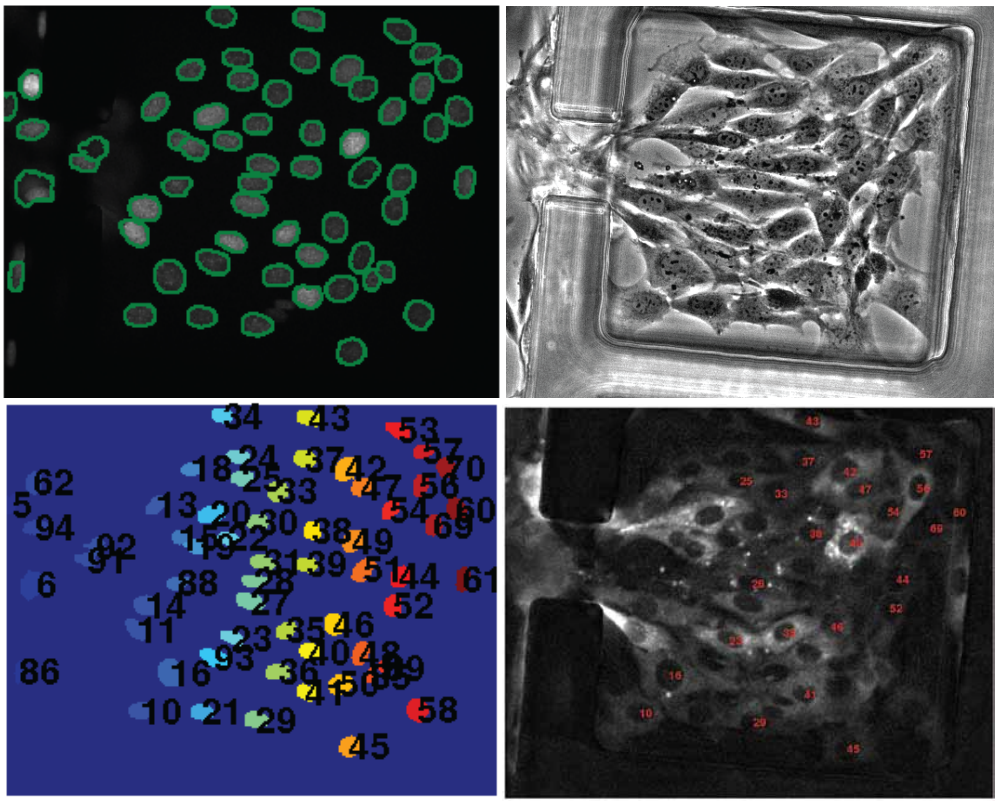

Figure 3.5: Image processing workflow. (Top-left) The green fluorescence channel containing the H2B-GFP signal information is used to identify cellular nuclei. (Bottom-left) Tracking of nuclear overlap between successive images allows for tracking of individual cells throughout the entire image stack and labeling of the nuclei with unique numerical identifiers. (Bottom-right) Automated removal of nuclei excludes cells that crawl out of the field of view and neighboring cells whose nuclei overlap excessively, indicating crawling over each other. Additional removal of such cell trajectories as well as those of dividing cells is performed manually for each image stack. (Top-right) Phase image of an ideal culture trap which contains a colony of cells that are well spread out and separated allowing for ready identification of distinct nuclei.

(e) fluorescence CV within the nucleus in any frame is greater than 1

(f) more than 5 frames are out of focus

(g) one fluorescent value is brighter than 99.5% of all values from that experiment

(h) 30 or more values in the trajectory are above 99% of all values from that experiment

All of the automatically generated trajectories are then manually checked for cells that divide or crawl over each other (obscuring the nuclear signal with cytoplasmic signal from a neighboring cell) and such trajectories are excluded from subsequent analysis. A peak-finding algorithm is performed on each trajectory using an amplitude cutoff calculated as:

$$cutoff = 3 \times median(std(10\ frames\ prior\ to\ signal)) \tag{3.1}$$

If a trajectory contains a peak prior to the start of TNFα stimulation whose amplitude is greater than or equal to:

$$4 \times median(std(frames\ prior\ to\ signal)) \tag{3.2}$$

then that trajectory is eliminated. Responding trajectories are identified as those whose largest amplitude peak is within 3 hours of the onset of stimulation and is greater than or equal to the value calculated by Eqn 3.2.

3.5 Results

The focus of our microfluidic experiments was to probe the hypothesis that two different modes of stimulation by TNFα (step versus ramp induction) each produce unique dynamics of the NF-κB response in single cells. A step induction is characterized by an instantaneous jump from zero to 100% TNFα and is the traditional mode of stimulation that has been practiced in macroscale culture. On the other hand, a ramp induction is uniquely enabled by microfluidics and exposes cells to a linear temporal gradient of TNFα which more closely mimics an in-vivo stimulation profile.

We explored the effect of this step versus ramp induction for a range of TNFα concentrations and "thaw times". As described in the experimental setup section, when TNFα is initially introduced it rapidly warms to 37°C and begins to degrade from the active homotrimer form into inactive monomers which are incapable of stimulating cells. The rate of this decay is the subject of some debate, as reports in literature on the half-life of TNFα degradation vary from a value of $\sim$20 hours or more (Poiesi et al., 1993; Krippner-Heidenreich et al., 2008) to just 1 hour (Tay et al., 2010). Thus in our experimental setup, we carefully record the time between initial TNFα introduction and the start of stimulation (step or ramp) as the TNFα "thaw time" in an attempt to explore whether the degradation of TNFα in this manner introduces a change in the NF-κB response. A summary of the individual microfluidic experiments is presented in Table 3.1.

3.5.1 Cell response, oscillations and effect of TNFα degradation

Our analysis indicates that virtually all of the cells respond to a step function of TNFα for all concentrations tested (Fig 3.6). Furthermore, a majority of these cells continue to oscillate, defined as having trajectories characterized by at least two peaks after the initial response peak. We observe essentially the same high fraction of responding cells when comparing ramp and step experiments, except for the 1ng/mL TNFα ramp experiments which show a slightly lower fraction of initial responders. This indicates that the low dose ramp experiments initially stimulate the cells with a minimal concentration of TNFα below the full-response threshold, which is in line with the previously reported digital mode of NFκB activation in single cells (Tay et al., 2010). In terms of oscillatory behavior beyond the initial response, all step and ramp experiments for the range of TNFα concentrations tested display the same fraction of oscillating cells, even though visually there appears to be a downward trend of this value in step experiments as a function of increasing thaw time. This is readily explained by noting that an increase in thaw time means that stimulation begins at a later time point in the experiment

Table 3.1: Summary of TNFα experimental conditions. Each condition is the result of a single microfluidic device experiment.

Exp #	TNFα (ng/mL)	Step or ramp (length)	Thaw time (hrs)	# of traj. post-auto	# of traj. final
1	10	step	1.4	515	388
2	10	step	3.9	579	400
3	10	step	6.3	107	100
4	10	step	6.3	639	379
5	10	step	6.5	448	291
6	10	step	7.2	340	188
7	10	ramp (6 hr)	1.6	260	126
8	10	ramp (6 hr)	1.9	358	265
9	10	ramp (7 hr)	2.2	524	381
10	10	ramp (6 hr)	2.6	383	235
11	10	ramp (3 hr)	2.7	349	206
12	1	step	1.2	533	382
13	1	step	1.7	420	283
14	1	step	3.3	596	436
15	1	step	6.3	335	143
16	1	step	6.4	777	409
17	1	ramp (3 hr)	3.8	282	185
18	1	ramp (4 hr)	4.3	402	300
19	0.1	step	0.7	438	351
			Total:	8285	5448

and given our typical experimental observation window of 10 hours we effectively decrease the number of peaks we can observe as a function of increasing thaw time. For comparable thaw times, the number of oscillations observed remains the same across experiments. The period of oscillations is consistently between 60-80 minutes for all experiments (Fig3.7A).

The degradation of TNFα is evident by noting the decrease in the amplitude of the initial response peak for step experiments as a result of increase in TNFα thaw time (Fig 3.7B). To determine the TNFα half life we used a model to fit the median amplitude of the first peak from the step-only experiments for 10ng/ml, 1ng/ml, and 0.1ng/ml TNFα. The model is based on these assumptions:

(a) TNFα decays exponentially

(b) Median amplitude of the first peak is related to the external TNFα concentration through the following function:

$$Amp = \frac{c1\ TNF_{external}}{c2 + TNF_{external}} \tag{3.3}$$

We model the relationship between TNFα and median amplitude of the first peak as:

$$Amp = \frac{c1\ TNF_{initial} \exp\left(-C_{decay}\ TNF_{thaw\ time}\right)}{c2 + TNF_{initial} \exp\left(-C_{decay}\ TNF_{thaw\ time}\right)} \tag{3.4}$$

Using this model we performed a parameter search for c1, c2 and C_{decay} (Fig 3.8A) and computed a half-life of 3.2 hours for TNFα. The model has a good fit to the experimental data (Fig 3.8B), except for very low concentrations of TNFα most likely because the minimum amplitude cutoff value (which is used during peak-finding analysis of experimental trajectories) is very close to the median first peak amplitude for those particular experiments.

Our value of TNFα half-life of 3.2 hours is closer to the half-life value of 1 hour determined by a recent microfluidic single-cell NFκB study (Tay et al., 2010) than to the 20 hr half-life reported by previous macroscale studies (Poiesi et al., 1993; Krippner-Heidenreich et al., 2008), but it is clear that a rigorous experimental determination of this value remains to be carried out. One significant difference between our setup and the microfluidic study mentioned above is that we continuously perfuse the culture chambers with media containing TNFα while the other study performed a one-time delivery of inducer media into the culture chambers which were then sealed off for the duration of the experiments. Due to the continuous internalization of TNFα by the cells in the culture chambers, the effective concentration of the inducer in their closed setup would be less than in our perfused system and this may explain the higher half-life value that we obtained by a similar mathematical analysis to that performed by Tay et al. (2010). The large discrepancy when comparing the TNFα half-life value obtained from microfluidic studies to macroscale experiments begs the question of a detailed analysis to address how adsorption of small hydrophobic molecules and proteins to the biomaterials of microfluidic devices can affect the effective concentration of

biochemical inducers in a microfluidic system (Toepke and Beebe, 2006; Regehr et al., 2009; Berthier et al., 2012).

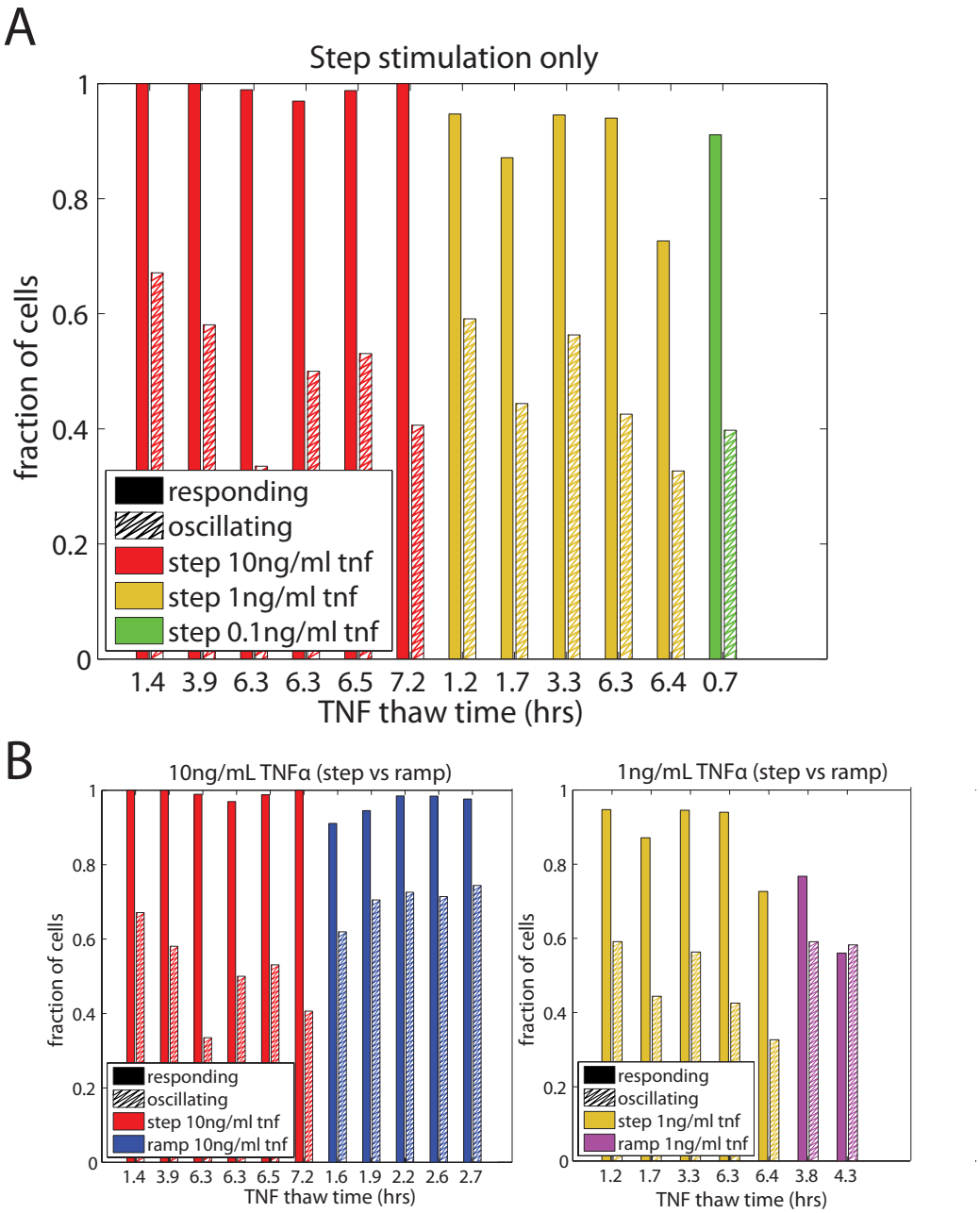

Figure 3.6: Initial response and oscillations. (A) Nearly all cells respond to a step stimulation of TNFα and a high fraction of cells shows oscillations. (B) The fraction of responding and oscillating cells for ramp experiments is comparable to step experiments, but ramp data does not display a decrease in the fraction of oscillating cells at longer thaw times.

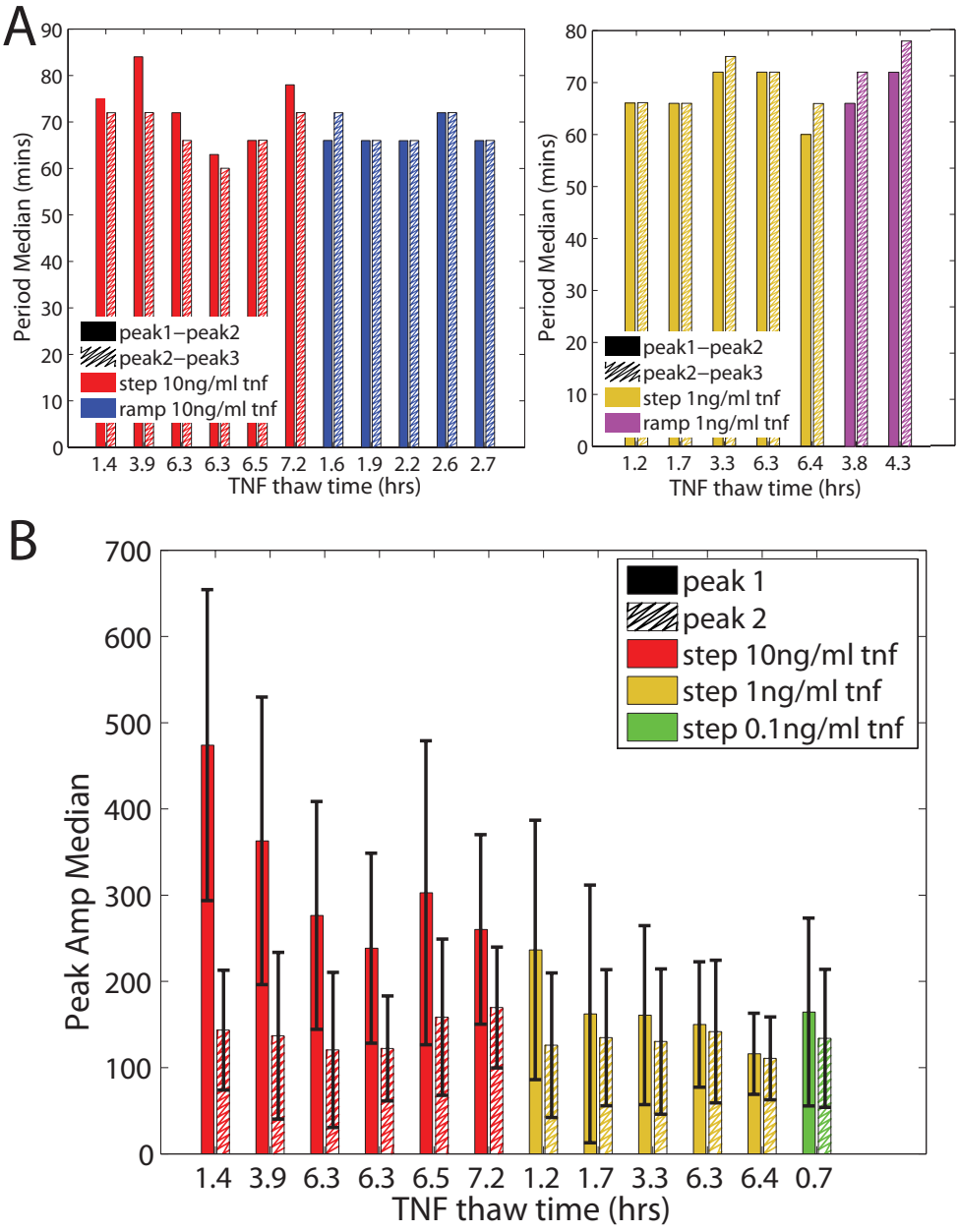

Figure 3.7: Oscillation period; effect of TNFα thaw time. (A) The period between peaks remains consistent for both step and ramp experiments. (B) The decrease in the amplitude of the first peak as a function of TNFα thaw time indicates the inducer is degraded over time and results in a lower magnitude of stimulation at increased thaw times.

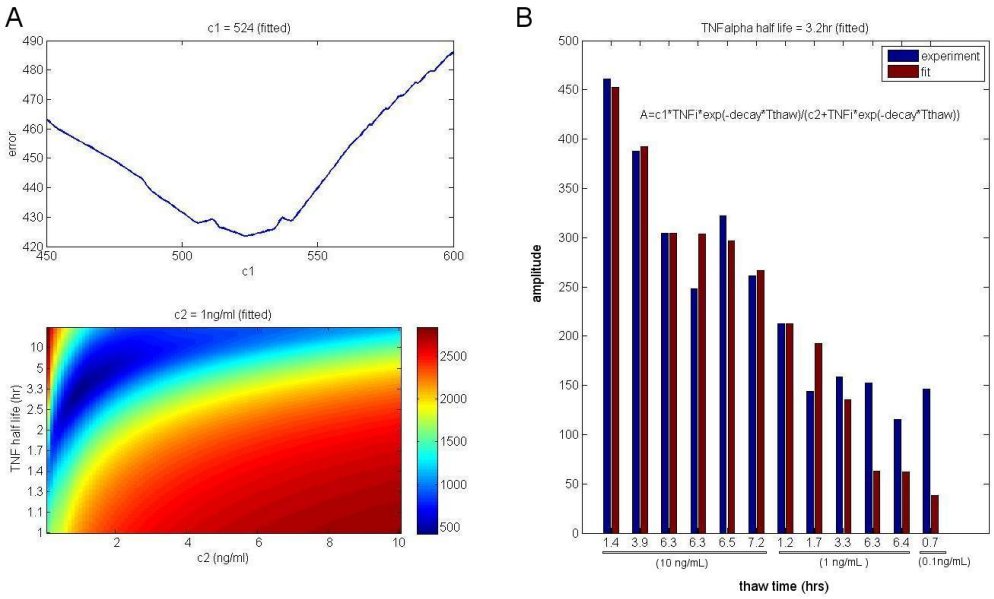

Figure 3.8: Model fit determination of TNFα half-life. (A) Parameter search to optimize the model fit to the experimental data (B) in order to obtain a value for TNFα half-life.

3.5.2 Timing of the NFκB response

Our analysis of the single-cell experimental trajectories reveals significant cell-to-cell variability in the timing of the NFκB response to TNFα. We find that for a step-wise stimulation with TNFα, a low dose of inducer (1ng/mL, 0.1ng/mL) results in a slight delay of the first response peak (increased response time) when compared to a 10ng/mL dose at similar thaw times (Fig 3.9A). Although the magnitude of the median delay is slight (5-10 mins), the increased standard deviation of the delayed peak at low TNFα concentrations indicates a significant change in the dispersion of the distribution of the single-cell response, as described by the large increase in the coefficient of variation from high to low TNFα.

The increase in CV is also evident in ramp experiments at 10ng/mL TNFα compared to step induction (Fig 3.9B). For all TNFα thaw times, the CV for 10ng/mL ramp experiments is nearly twice the CV in step experiments. At 1ng/mL TNFα, a difference in first peak timing CV between ramp and step is not discernible.

A previous single-cell study has demonstrated the effect of delayed activation of NF-κB as a function of decreasing dose of TNFα (Tay et al., 2010). We confirm these results by observing that a step function of a high level of TNFα (10ng/mL) significantly decreases the cell-to-cell variability in the timing of the NFκB response when compared to low values (1ng/mL and below) of TNFα. Furthermore, we present the first case of a truly dynamic stimulation of NFκB in single-cells by exposure to a linearly increasing concentration of TNFα and demonstrate that this mode of induction also has the effect of increasing response time variability.

The source of the variability can emanate from cell-to-cell differences in intracellular parameters (protein numbers, stage of cell cycle, stage of circadian rhythm, etc.) and/or inherent stochasticity within the NFκB signaling pathway. For exploring the contributions to variability from these sources, our results indicate that is important to consider not only the induction concentration of TNFα but also the time-dependent profile of stimulation (e.g. ramp or step). Even at high TNFα concentration, a ramp in-

duction allows for the observation of enhanced response timing variability as each cell is gradually exposed to its own minimum level of TNFα required to elicit a response.

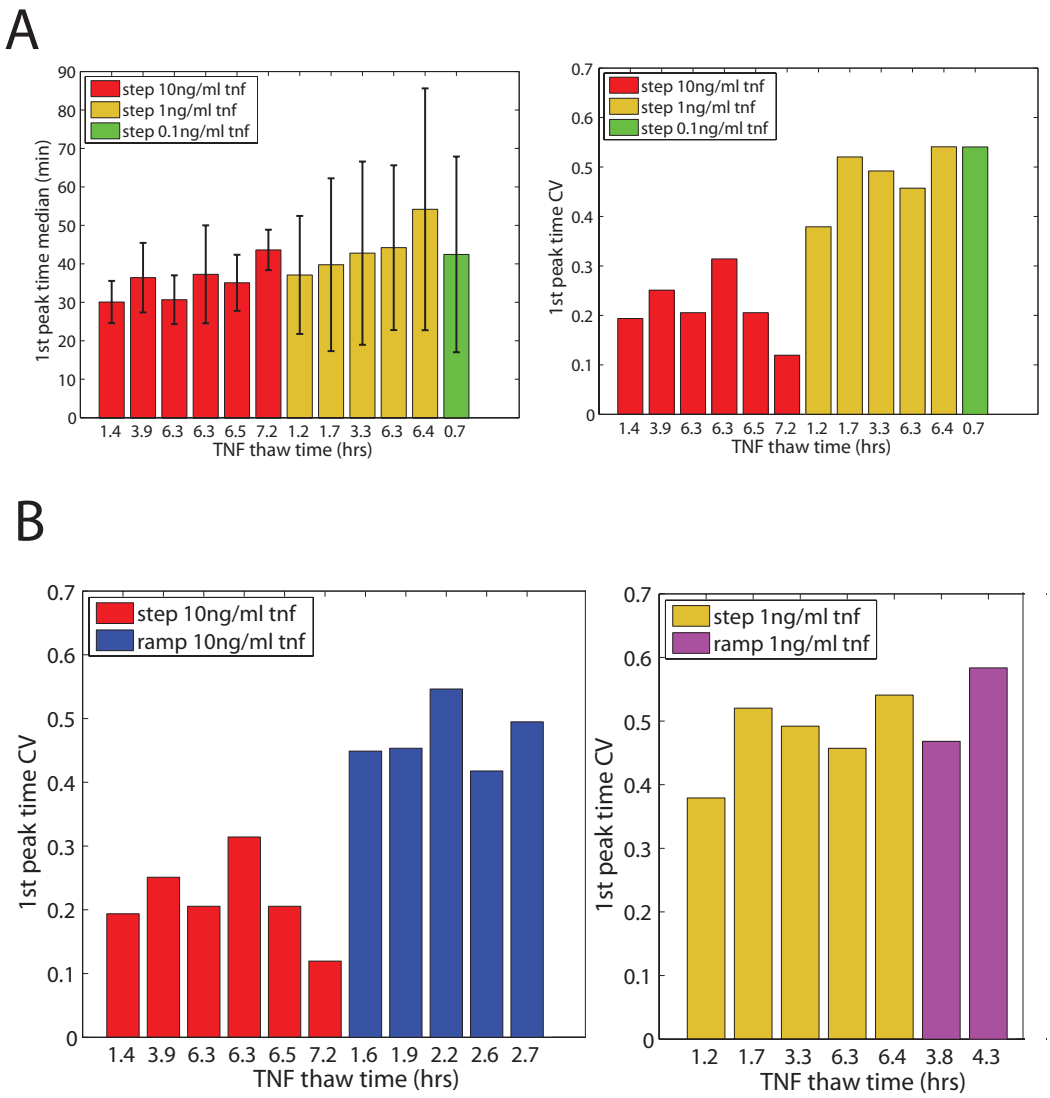

Figure 3.9: Timing of the NFκB response. (A) Step stimulation at low concentration of TNFα results in enhanced variability in the response time of the first NFκB peak compared to step induction with 10ng/mL TNFα. (B) Ramp stimulation at 10ng/mL TNFα produces a more variable timing response compared to a step induction at this concentration, but this ramp versus step effect is indiscernible at the 1ng/mL TNFα induction level.

3.5.3 Amplitude of the response

Perhaps the most interesting result from our dynamic stimulation experiments is the difference in amplitude response of NFκB to step versus ramp induction. We find that for all TNFα concentrations, a ramp mode of stimulation results in individual cell trajectories which are characterized by oscillation peaks of uniform amplitude. On the contrary, a step-wise induction with a strong TNFα impulse (high concentration and/or short thaw time) results in a sharp high-amplitude initial response peak followed by lower-amplitude peaks of uniform magnitude (Figures 3.10 and 3.11).

The median peak-1 to peak-2 amplitude ratio for all ramp experiments is approximately one, while for step experiments with 10ng/mL TNFα the typical ratio is two or higher, especially for short thaw times (Fig 3.12A). As the strength of the TNFα step-wise induction decreases (with lower concentrations or longer thaw times), the median peak-1 to peak-2 amplitude ratio approaches one (Fig 3.12B). Similarly, a 1ng/mL TNFα step stimulation with a very short thaw time (1.2 hrs) produces a peak-1 to peak-2 ratio around two, but at longer thaw times the ratio quickly approaches one.

Looking beyond the first peak for both step and ramp experiments, the peak-2 peak-3 ratio for all experiments is uniformly around one. A consideration of absolute magnitudes rather than relative ratios allows for comparison of peak amplitudes among different experiments (Fig 3.13), which further confirms that the characteristic high first peak amplitude is unique to step experiments of strong TNFα impulse while ramp experiments produce uniform peak amplitudes for the duration of the response.

A truly dynamic stimulation profile in the form of the ramp stimulation presented here was previously impossible to achieve in macroscale culture. Our study raises the question of whether the generally observed increase in amplitude response of the initial NFκB peak as a function of increasing TNFα concentration is simply a by-product of traditional step-like stimulation.

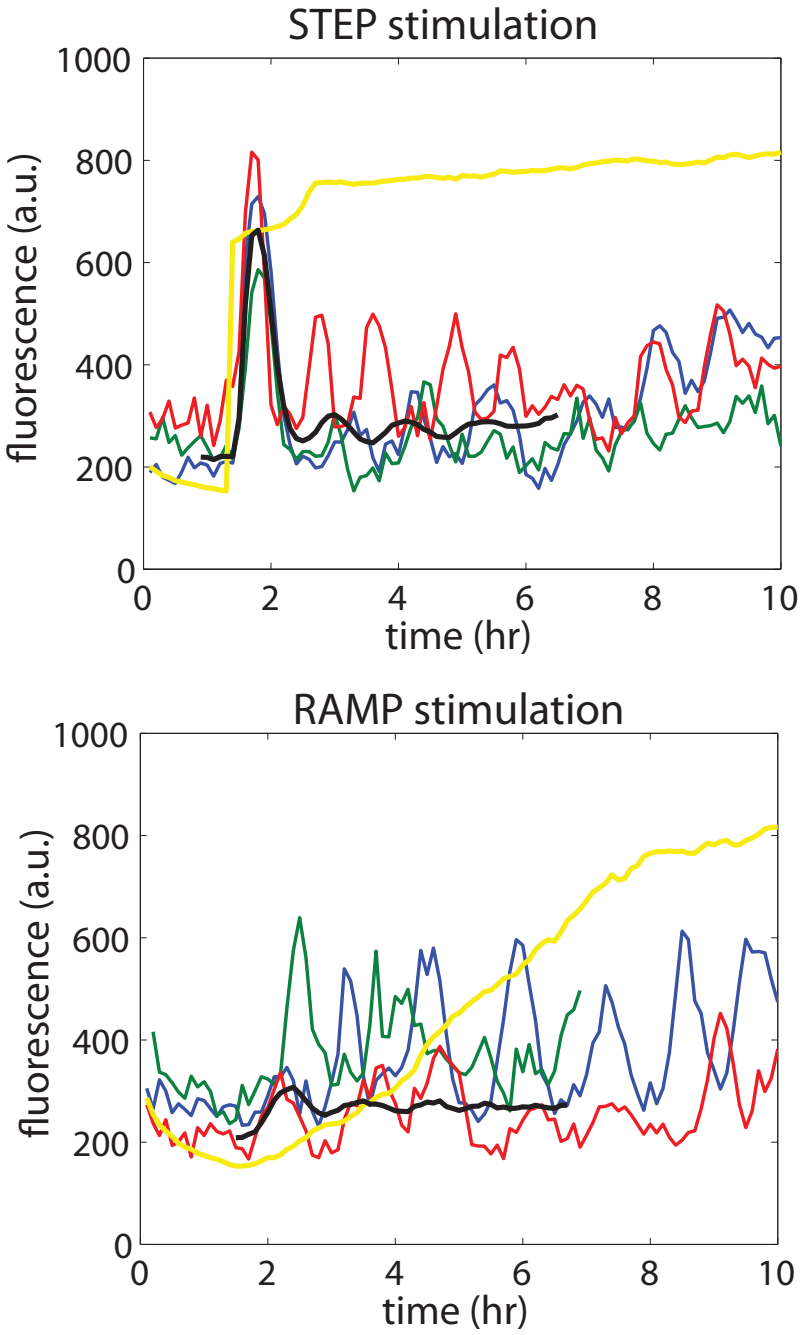

Figure 3.10: Single-cell trajectories: step versus ramp. Example trajectories of nuclear NFκB signal of individual cells in response to step (top) or ramp (bottom) stimulation with 10ng/mL TNFα. The yellow trace indicates the signal of TNFα concentration as followed by a fluorescent dye. The black trajectory represents the mean of all trajectories for each experiment.

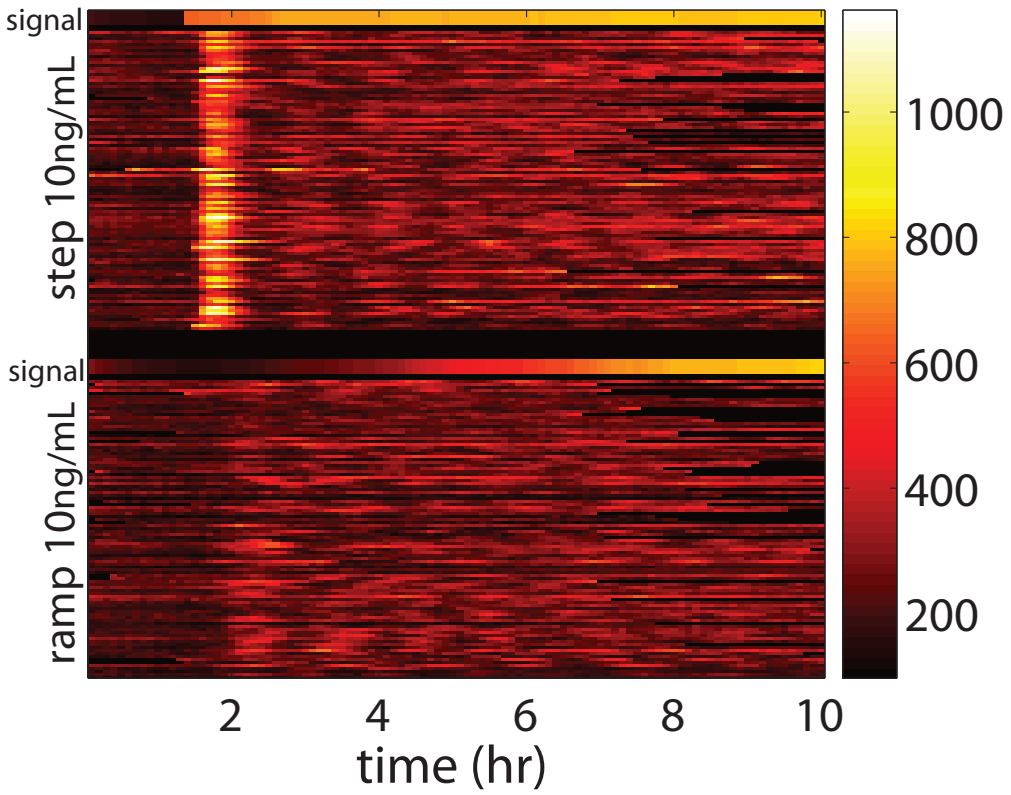

Figure 3.11: Trajectories heat map comparing step and ramp induction. All of the individual trajectories obtained from a step experiment (top) and a ramp experiment (bottom) at 10ng/mL TNFα are displayed.

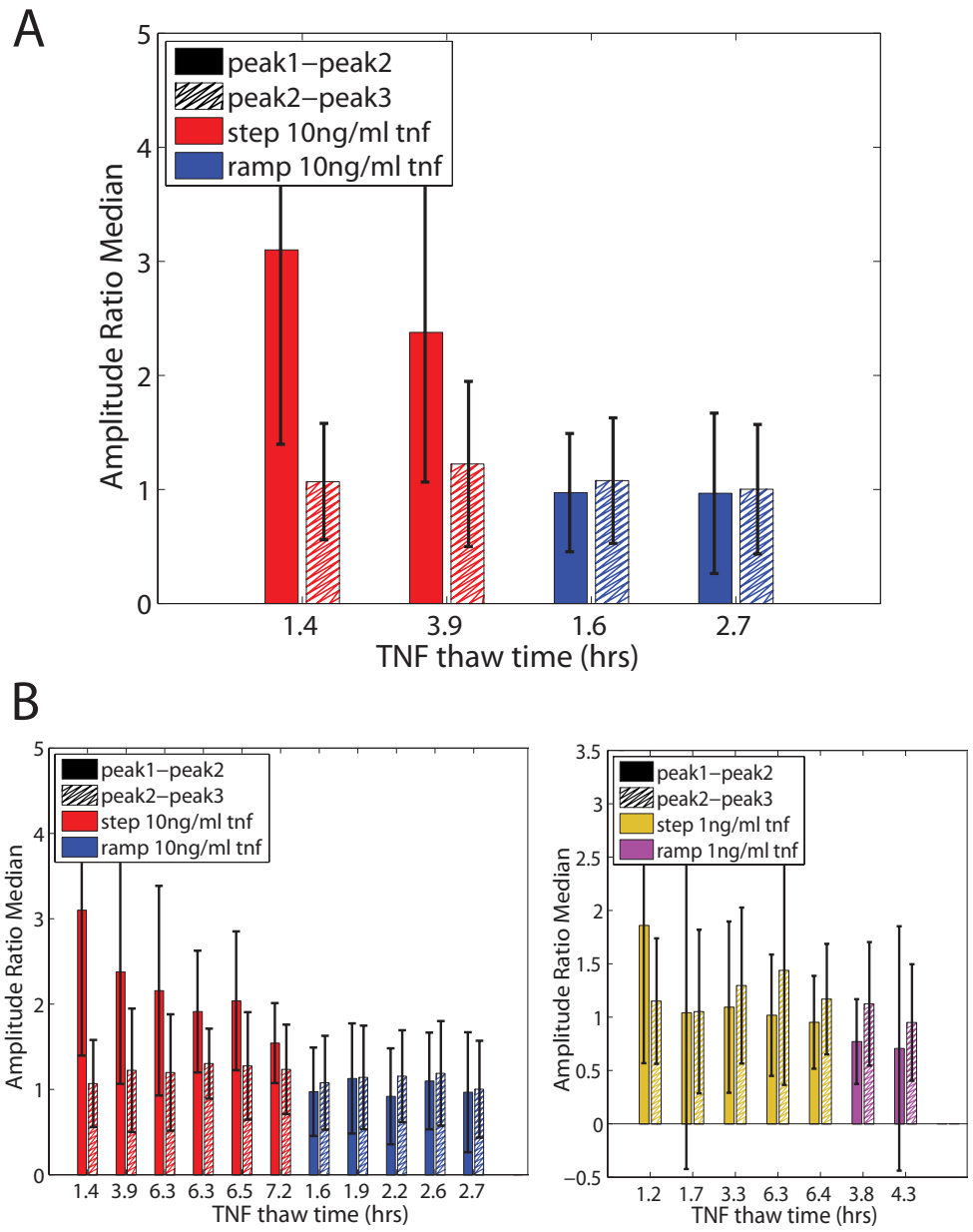

Figure 3.12: Response peak amplitude characteristics of step and ramp experiments. (A) 10ng/mL step experiments with thaw times that span a range inclusive of the presented 10ng/mL ramp experiments indicate that the peak1-peak2 amplitude ratio is much higher for step induction than ramp. (B) This effect is most pronounced at high TNFα levels (10ng/mL) with short thaw times and gradually diminishes as the dose of TNFα is lowered by decreasing the concentration and/or extending the thaw time. Response peaks after the initial peak are characterized by an amplitude ratio of $\sim$1 for all experiments.

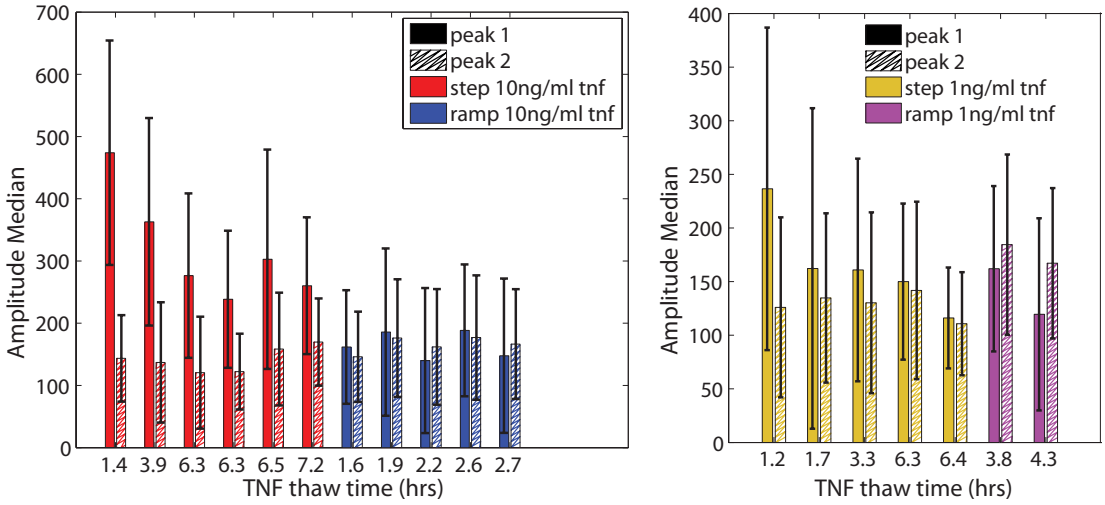

Figure 3.13: Absolute amplitudes of the first two response peaks. A consistent magnitude of peak two for all experiments shown (10ng/mL and 1ng/mL, step and ramp) further confirms that only the magnitude of the initial response peak changes as a result of changes in induction strength and/or profile.

3.6 Discussion

Our microfluidic experiments present a novel characterization of the single-cell NFκB response by exposing cells to a dynamic input of TNFα in the form of a linear temporal gradient (ramp). The principal results indicate that a ramp exposure to TNFα elicits the same high fraction of activated and oscillating cells as a step induction, but with key differences in the characteristic amplitude and timing of the response. Specifically, the uniform peak amplitudes observed in response to a ramp stimulation indicate that the previously described 1^{st}peak amplitude dependence on TNFα concentration in step stimulation experiments appears to be an artifact of this un-natural mode of induction which overstimulates the initial cell response by delivering a sharp impulse not representative of the gradual exposure of cells to TNFα in-vivo. Furthermore, the cell-to-cell variability in the timing of the response is diminished by a strong step impulse of TNFα compared to a ramp stimulation which gradually exposes each cell to its own minimum level of TNFα required to activate the NFκB response. Our results indicate

that studies which seek to characterize the dynamics of the NFκB signaling pathway need to consider whether a step-like impulse of a high level of inducer is relevant to the native context of in-vivo stimulation. The integration of our single-cell experimental data in a mathematical model to describe the NFκB response to dynamic TNFα input should provide novel insights into our understanding of this complex signaling pathway.

3.7 Acknowledgements

Chapter Three contains material in preparation for publication as Kolnik, M.*, Selimkhanov, J.*, Hoffmann, A., Tsimring, L.S., Hasty, J. 2012: Single-cell NFκB response in a dynamic microenvironment. (*equal contribution).

Chapter 4

Genomically integrated synthetic gene oscillator in mammalian cells

4.1 Design of a dual-feedback oscillator

The construction of synthetic genetic circuits that produce dynamic behavior has advanced our knowledge of how native biological systems function in real time which in turn enables us to construct synthetic circuits of increasing dynamic complexity. This cyclical relationship of ”build, discover, then build more” is at the core of synthetic biology and has proved to be a viable model for rapid progress in both the prokaryotic and eukaryotic space, although the latter has naturally lagged behind the former (Lim, 2010; Mukherji and Van Oudenaarden, 2009). The ultimate goal of synthetic biology beyond basic science is to apply the knowledge from this process towards the development of applications to improve human health (Weber and Fussenegger, 2011). With this goal in mind, we originally began the development of a mammalian genomically integrated synthetic gene oscillator in our lab almost a decade ago in order to help shed light on the interplay of transcriptional feedback mechanisms in the context of mammalian gene regulation.

The original mammalian design is largely based on lessons learned from a bac-

terial oscillator developed in E. coli (Stricker et al., 2008). The bacterial architecture consists of two transcriptional feedback loops which are coupled via expression from a hybrid promoter (Plac/ara-1) that has binding sites for each of the two transcription factors involved (Fig 4.1A). The negative feedback loop is mediated by LacI repressor which binds lacO operator sites within the promoter in the absence of a small molecule IPTG. The positive feedback loop is created by AraC activator which binds to the I1/I2 recognition site within the promoter in the presence of arabinose. The activity of the promoter is tracked by expression of GFP reporter. The two transcription factors and the fluorescent reporter protein are all tagged with a C-terminal degradation tag (ssrA) which targets the proteins for degradation by the ClpXP protease in order to enhance protein turnover which is required for fast oscillation dynamics. The key findings from the bacterial oscillator study are that a source of delay in the negative-feedback and rapid protein turnover are required for robust oscillations, in addition to strong repression and activation that ensures low basal promoter activity under repressing conditions but high expression during activation.

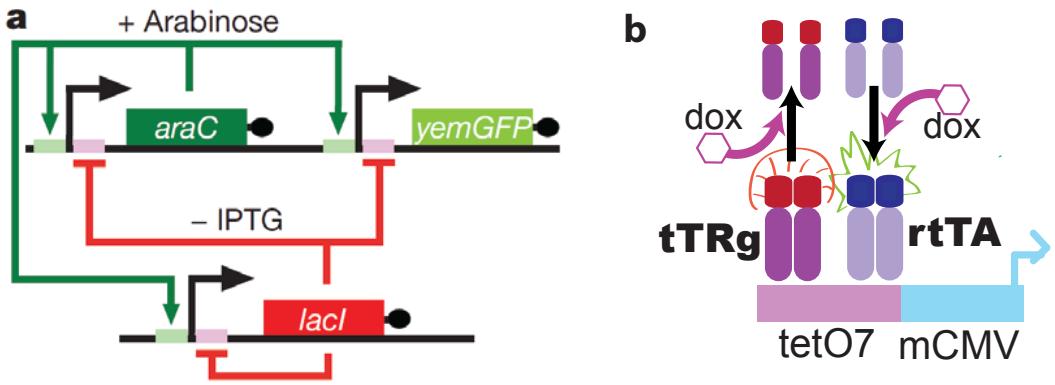

Figure 4.1: Dual-feedback oscillator design. (A) The coupled positive and negative feedback architecture of the bacterial oscillator is emulated by the mammalian design (B) which relies on the tetO7mCMV promoter to achieve coupling between rtTA and tTRG mediated positive and negative feedback, respectively. The effect of doxycycline on the activity of each chimeric transcription factor is indicated by arrows pointing towards either a functional dimerized state which can bind to the promoter or to an inactive dissociated form.

Given these observations, a mammalian analogue of this design was developed

and preliminary modeling indicated the potential for oscillations in certain regions of the parameter space. This original mammalian version was based on the use of the tetracycline-inducible transcription factors, rtTA and tTRg (Sprengel and Hasan, 2007; Rossi et al., 1998; Deuschle et al., 1995; Gossen et al., 1995). Both of these TFs are are chimeric proteins consisting of a tetR-based DNA-binding domain fused to either an activation or repression domain. The transactivator used is rtTA and consists of a tetR mutant with four point mutations that reverse the pharmacology of wildtype tetR response to doxycycline such that dox is required for tetR dimerization and subsequent binding to DNA operator sites. This mutant tetR is fused to the VP16 activation domain from Herpes simplex virus which recruits the RNA polymerase II transcriptional initiation complex to the tetR-bound DNA sites. The tTRg transrepressor consists of a tetR domain fused to the KRAB silencing domain from human kox1 protein (Moosmann et al., 1996a; Urrutia et al., 2003). The tetR domain in this case contains a G-class dimerization domain rather than the B-class domain of rtTA, hence the -g designation at the end of tTR. This G-domain prevents heterodimerization of the transrepressor with the transactivator when the two are used concomitantly (Rossi et al., 1998). The tetR DNA-binding of tTRg is abolished in the presence of doxycycline. To create coupled negative and positive transcriptional feedback loops using tTRg and rtTA, both transcription factors are expressed from a minimal CMV promoter preceded by seven tet operator sites (Fig 4.1B).

The positive feedback loop using rtTA has been previously constructed and characterized (Kramer and Fussenegger, 2005; Longo et al., 2010), but given the stable nature of the proteins used the system exhibits very slow kinetics requiring timescales on the order of days to transition between the ON and OFF state. As we learned from the bacterial study, oscillations are enhanced by rapid protein turnover rates and thus I chose to tag the transcription factors and fluorescent protein reporters with a degradation signal sequence from murine ornithine decarboxylase (MODC). MODC is an enzyme involved in polyamine synthesis and is characterized by extremely rapid turnover with a native half-life on the order of minutes. Much like the ssrA tag targets proteins for

degradation by the ClpXP protease, the C-terminal sequence of MODC leads to rapid degradation by the 26S proteasome (Murakami et al., 2000) and has been successfully used to destabilize fluorescent proteins (Li et al., 1998; Corish and Tyler-Smith, 1999). The degradation of MODC is unique in that it is independent of the ubiquitin pathway which targets most proteins to the 26S proteosome. Li et al. (1998) generated several variants of the MODC degradation sequence by mutating key amino acids and characterizing the corresponding change in protein half-life when fused to the C-terminus of GFP. While the native MODC degradation sequence (amino acids 422-461) decreased the half-life of the GFP fusion to approximately 2 hours, several slower and some faster turnover variants were created. For incorporating this degradation tag in my oscillator circuit, I sought to maximize turnover of the activator and fluorescent reporter GFP by using the mutant variant with the reportedly shortest half life (E428/E430A/E431). Since we learned from the bacterial oscillator that some timing delay is required for robust oscillations, we incorporated this idea in our mammalian design by tagging the repressor (tTRg) with a longer half-life MODC sequence variant (E444A). The fast and slow tags are henceforth refered to as modc1 and modc2, respectively, and the amino acid sequences of each are shown in table 4.1. The underlined positions indicate mutations where the amino acid of the native MODC sequence was converted to Alanine.

Table 4.1: Degradation sequences from murine ornithine decarboxylase were used target proteins for rapid turnover.

modc1	SHGFPP<u>A</u>V<u>AA</u>QDDGTLPMSCAQESGMDRHPAACASARINV
modc2	SHGFPPEVEEQDDGTLPMSCAQ<u>A</u>SGMDRHPAACASARINV

In order to express the multiple components (activator, repressor, fluorescent reporter) of the proposed oscillator circuit without requiring three separate promoter-gene-polyA casettes I chose to use internal ribosomal entry site (IRES) sequences to achieve polycistronic expression. Unlike bacteria, mammalian cells process newly transcribed mRNA by adding a 5' methylated GTP cap and a 3' poly A tail. Subsequent translation of mRNA in mammalian systems requires recognition of the cap to intiate

efficient protein synthesis by the ribosome. To bypass this cap requirement and to initiate protein translation in the middle of an mRNA molecule, an IRES sequence placed in such a position forms a tertiary structure which recruits ribosomes directly to this site to initiate efficient translation (Hellen and Sarnow, 2001). A variety of viruses employ IRES sequences to ensure translation of viral proteins when host translation may be inhibited, and as a result the majority of well-characterized IRES sequences in use today are derived directly from such viruses. Perhaps the most commonly used IRES is that from the encephalomyocarditis virus (EMCV) and this is the sequence which I chose to use for polycistronic expression (Bochkov and Palmenberg, 2006). This particular IRES has seen widespread use since Novagen (originally of Madison, WI) commercialized it in 1990 in the form of the pCITE-1 vector. When this sequence was originally developed, Novagen made a mistake during cloning and an extra Adenine was added to a string of 6As in what turned out to be a critical region of a bifurcation loop crucial for interaction with translation initiation factors. This sequence was corrected in pCITE-2 back to the wildtype EMCV but this caused overexpression from the IRES-driven cistron and Clontech (Mountain View, CA) eventually started offering vectors such as pIRES which had an EMCV sequence modified back to the 7A original pCITE-1 error. This 7A sequence offers comparable expression levels from both the first and second cistron in a bicistronic configuration and hence this is the IRES sequence I used for the constructs I describe here.

The next step was to determine the method of expressing the constructs in a mammalian cell line and since we were interested in generating stable cell lines we chose retroviral transduction to genomically integrate our genes of interest into the target cells. Based on initial work on this project by a graduate student in our lab, Diane Longo, a mouse fibroblast line (NIH 3T3) was chosen as the target cell line. To infect this cell line, retroviral vectors kindly provided by Helen Blau, Blau Laboratory (Stanford University, Palo Alto, CA) were used (Rossi et al., 1998). These vectors are based on the MFG-derived retrovirus containing a self-inactivating (SIN) 3' LTR; the MFG-vector is originally developed from the Moloney Murine Leukemia Virus (MoMuLV) (Dranoff

et al., 1993). The HRS vectors provided by Dr. Blau contain a tetracycline-regulatable promoter consisting of seven tandem tet-operator sequences just upstream of a minimal cytomegalovirus (CMV) promoter oriented antisense to the viral 5' LTR. A bovine growth hormone poly-A sequence follows after a multi-cloning site just downstream of the mCMV promoter. An SV40 promoter driving expression of the puromycin resistance gene is oriented anti-sense to the mCMV promoter and allows for antibiotic selection of cells infected with the construct. Three vectors containing the components for building the oscillator circuit (tTRg, rtTA, IRES, EGFP) were used and their composition is summarized in Table 4.2. The HRS backbone was used as the primary workhorse for developing the majority of constructs described herein, and its layout is shown in Fig 4.2. An ampicillin resistance cassette and bacterial pBR replication origin allow for plasmid cloning and amplification in E. coli.

Table 4.2: HRS vectors contain the tet-based promoter as well as the transactivator and transrepressor

Hermes HRSpuro-gfp	tetO7mCMV	EGFP-bex1	BGH polyA	SV40 puro
RetroTet RTRg(-)cd8	tetO7mCMV	tTRg	IRES	
RetroTet RTAb(+)	rtTA			

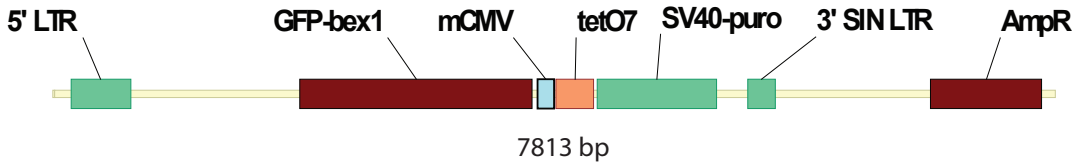

Figure 4.2: HRSpuro-gfp. The tetO7mCMV promoter drives GFP expression (or another gene of interest) while an antisense SV40 promoter drives expression of the puromycin resistance gene for selection of stably integrated constructs.

4.2 Molecular cloning and characterization of transgenic cell lines

I sought to efficiently combine all three protein components into a tricistronic casette within a single vector and I focused my initial molecular cloning to build the modular components required for this. Specifically, I tagged each protein with an MODC sequence and incorporated the IRES just in front of the tagged protein coding sequence. To easily combine three pieces of DNA in this manner, I used the method of yeast homologous recombination which allows rapid and efficient fusion of multiple PCR fragments (Vo et al., 1997; Wendland, 2003). PCR primers were designed such that each of the necessary components from the HRS vectors could be amplified and joined to each other via 40bp of homology. The 120bp MODC tags and stop codon were synthesized by PCR using two opposing primers of 70bp, each with 20bp 3' homology to the other. To perform the homologous recombination, plasmid pRS426 (a multifunctional high-copy yeast shuttle vector) is linearized by restriction digest and combined with the PCR fragments in order to transform yeast cells, which are then screened for the properly recombined sequence. In this manner, I generated the three modular constructs shown in Table 4.3, each of which was confirmed by direct sequencing (Eton Biosciences, San Diego, CA).

Table 4.3: Cassettes generated by yeast homologous recombination enable a modular approach to constructing complex vectors.

Cassette	components	total size
Fluorescent reporter	IRES - EGFPbex1 - modc1	1406 bp
Activator	IRES - rtTA - modc1	1697 bp
Repressor	IRES - tTRg - modc2	1685 bp

To link the activator, repressor, and EGFP in a single tricistronic construct, I used PCR to amplify the rtTA-modc1 and link it to the repressor and fluorescent reporter casettes. Specifically, an MfeI restriction site was used to join rtTA-modc1 to the repressor cassette and a PacI site was used to link repressor to fluorescent reporter

cassette. The tricistron was termed 'ARE' given the activator, repressor and eukaryotic gfp and contains a 5' BglII site and a 3' AgeI site. Ligations were all performed in the HRSpuro backbone which contains the BglII, MfeI, PacI and AgeI sites in between the mCMV promoter and polyA sequence in order to perform the sequential insertion of casette components to generate HRSpuroARE. This construct carries all of the oscillator components on a single backbone and exhausts the capacity of the MoMuLV backbone, given that the native size of this retrovirus is 8.3kb and the ARE construct pushes the MFG backbone to 8.0kb. This is critical to note for the design of retroviral delivery vectors because creating a payload beyond the native size of the retrovirus typically leads to improper packaging and recombination of the sequence to be delivered. During the stepwise construction of HRSpuroARE, the following constructs were also made: AE (activator-ires-egfp), RE (repressor-ires-egfp) and E (egfp only), each expressed from the tetO7mCMV promoter in the HRSpuro backbone.

For viral production, I used the Phoenix Ecotropic packaging cell line developed by the lab of Dr. Garry Nolan (Stanford University) and made available through the American Type Culture Collection (ATCC #SD-3444). The Phoenix-Eco line is a 293T derived cell line that is unique in that it is highly transfectable (typically at least 50% efficiency). The Phoenix cells express constructs which drive the production of the viral Gag and Pol genes, as well as the desired Envelope protein (either amphotropic or ecotropic). The ecotropic designation means that the virus produced only infects murine cells, as opposed to the wide host range amphotropic version. For initial viral production experiments using the Phoenix line, I carried out transfections by the calcium phosphate method (Schenborn et al., 2000). In brief, this very commonly used method causes DNA to co-precipitate with the calcium coming out of solution in order to create high concentration of DNA particles that settle on the cells and enter by pino/phagocytosis. To prepare the transfection complex, DNA is mixed with $CaCl_2$ and then precipitated by adding HEPES buffered saline. The simplicity of the protocol makes for widespread use of this method, but reproducibility of transfection efficiencies is highly sensitive to external conditions such as pH and temperature (Jordan et al., 1996). The pres-

ence of a fluorescent reporter (EGFP) in all of my constructs allowed me to easily track transfection efficiency by flow cytometry or epifluorescent imaging. For the first round of transfections, the following efficiencies for Phoenix cells were determined for the four constructs by flow cytometry: 64% (E), 19% (AE), 10% (RE) and 4% (ARE). The multicistronic constructs appear to express EGFP less efficiently, perhaps due to its positional effect of the second cistron. The efficiences were sufficient to expect some positive transductants of the virus into 3t3 cells upon infection. The virus was applied to the target cells and antibiotic selection was carried out with 3μg/mL puromycin after establishing a kill-curve on wildtype NIH 3t3 cells which indicated that this concentration was enough to kill all wildtype cells within a 3-4 days of culture. Analysis of transduced populations revealed that transgene expression rapidly decays in the absence of antibiotic maintenance after initial selection (Fig 4.3). Furthermore, at the population level a response to doxycycline was not detectable.

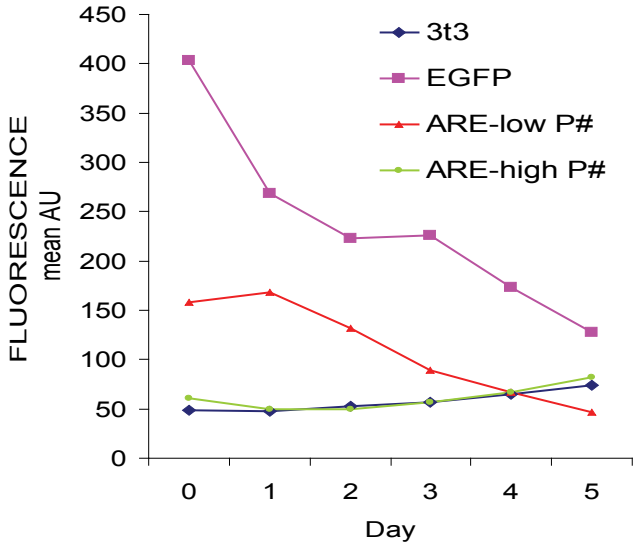

Figure 4.3: Transgene expression without puromycin maintenance. ARE cells were induced with 0.1 μg/mL doxycycline. All fluorescent cell lines display a time-dependent decrease in GFP expression in the absence of puromycin selection. High passage number ARE populations are virtually identical to wildtype 3t3s.

In order to minimize the effects of non-responding cells at the population level,

single cell clones for each transgenic cell line were obtained by fluorescence activated cell sorting (FACS) (Fig 4.4). During sorting, the E population of transduced 3t3 cells had a high GFP positive fraction (69%) while the remaining 3t3 cell populations (AE, RE and ARE) displayed minimal GFP expression (∼0.1%). A low fraction of positive cells is often beneficial for cell sorting since it prevents accidental deposition of two consecutive positive cells into the same well. From the total number of wells seeded for each population, a number of viable clones were obtained. The single viable ARE clone obtained grew slowly and was characterized by irregular morphology and thus it was excluded from further analysis. The remaining clones were characterized for basal GFP expression and response to doxycycline.

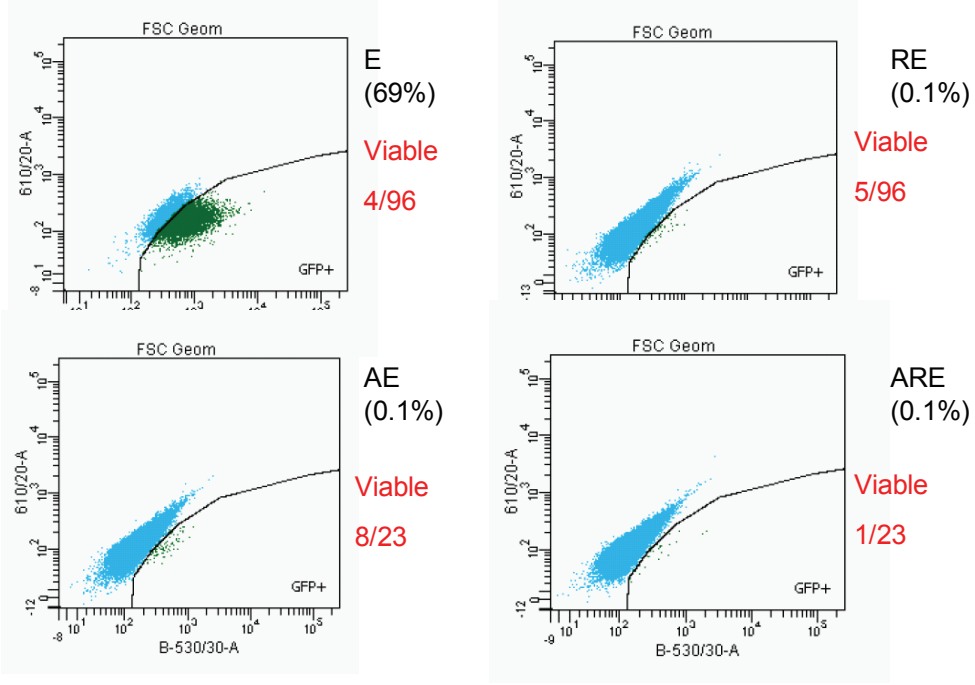

Figure 4.4: FACS to obtain clonal lines. The GFP positive cells which were sorted into single wells of a 96-well plate are shown in green within the GFP+ gate. The rate of positive cells is shown as a percentage for each population and the number of viable clones obtained from the total number of wells seeded is shown as a fraction in red.

The basal expression levels of GFP for a representative subset of clones is shown in Fig 4.5A. Notably, E clones had much higher GFP average fluorescence than AE

clones, suggesting that expression of GFP from the second cistron of a bicistronic configuration is less efficient than cap-dependent expression. The majority of AE clones respond to doxycycline as expected with increasing GFP production after dox induction in a dose-dependent manner (Fig 4.5B). The fold change at maximal induction is fairly low: 1.5 to two times the basal un-induced fluorescence level. Given this dynamic range for the positive feedback AE constructs, it was understandable that the negative feedback RE clones showed no detectable change in fluorescence upon dox induction. The results from these preliminary experiments indicated the need to express activator and repressor on two separate constructs (due to low cloning efficiency of the tricistronic ARE) and to move the fluorescent reporter into the first cistron to improve expression to obtain a greater dynamic range of dox induction.

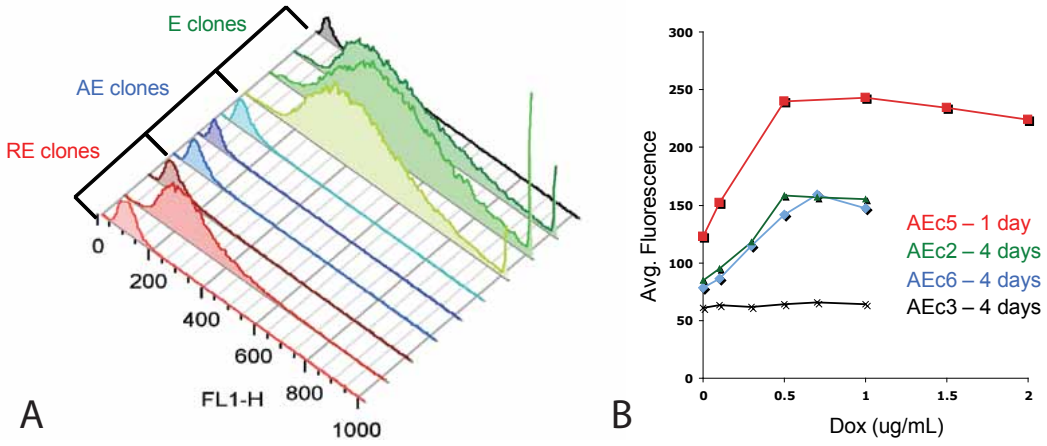

Figure 4.5: Basal GFP of representative E, AE, RE clones. (A) The low basal expression of EGFP from AE clones compared to E clones indicates low efficiency of IRES-driven expression. (B) The fold change of EGFP signal upon maximal dox induction of representative AE clones is minimal.

The modc1-tagged EGFP reporter was readily moved to the first cistron position by using the ARE construct as template for a PCR reaction to amplify everything except the AR portions of the vector and then re-ligating the PCR product to create HRSpuroEGFPmodc1. The rtTAmodc1 activator was then inserted as a second cistron behind EGFPmodc1 by PCR amplifying the IRES-rtTAmodc1 fragment with primers

that added AgeI flanking restriction sites and then ligating this product into the AgeI site immediately after EGFPmodc1. This yielded the construct HRSpuroEGFPmodc1-IRES-rtTAmodc1, referred to as HRSpuroEiA for short. The construct represents the self-contained positive feedback portion of the circuit which can be independently tracked via EGFP expression and selected with puromycin.

To create a corresponding negative feedback construct on a separate vector with independent antibiotic selection and its own fluorescent marker, the following molecular cloning was performed. An HRSpuroGUS vector (also received from the Blau Lab) was digested with BamHI and AvrII to remove a 708 bp fragment containing the puromycin gene and religated after blunting of the ends to yield a single AvrII site (BamHI site was now inactivated). The neomycin gene was amplified by PCR from pDsRed2-N1 (Clontech) in a manner that added flanking AvrII sites and the neo gene was then ligated into the AvrII site of the modified HRS vector to yield HRSneoGUS. The AR portion of ARE vector was then obtained by digesting with BglII and AgeI and this fragment was ligated into the BglII/AgeI sites of HRSneoGUS, which removes GUS and replaces it with AR. Thus, the vector HRSneoAR was created which expresses rtTAmodc1-IRES-tTRgmodc2 from the tetO7mCMV promoter and allows for selection with neomycin (G418). The rtTAmodc1 in this construct was replaced mCherry fluorescent protein by digesting HRSneoAR with BglII and MfeI to remove the tagged Activator and insert the mCherry sequence obtained by PCR amplification from pMFP58 using primers that added flanking BglII/MfeI sites. The resulting construct is HRSneoMCiT2, which refers to the expression of mCherry-IRES-tTRgmodc2 from the tetO7mCMV promoter and an HRS backbone with neomycin selection. I created this construct to test and confirm mCherry expression as a second fluorescent reporter in addtion to EGFP. Flow cytometry analysis indicated that a fluorescent reporter in addition to antibiotic selection greatly enhances screening for true positives (Fig 4.6).

The mCherry protein in this construct is stable since it does not contain a C-terminal MODC tag. To fuse the MODC tag on the end of mCherry required a two-step PCR. First a primer containing the 3' mcherry sequence (no stop codon) was used along

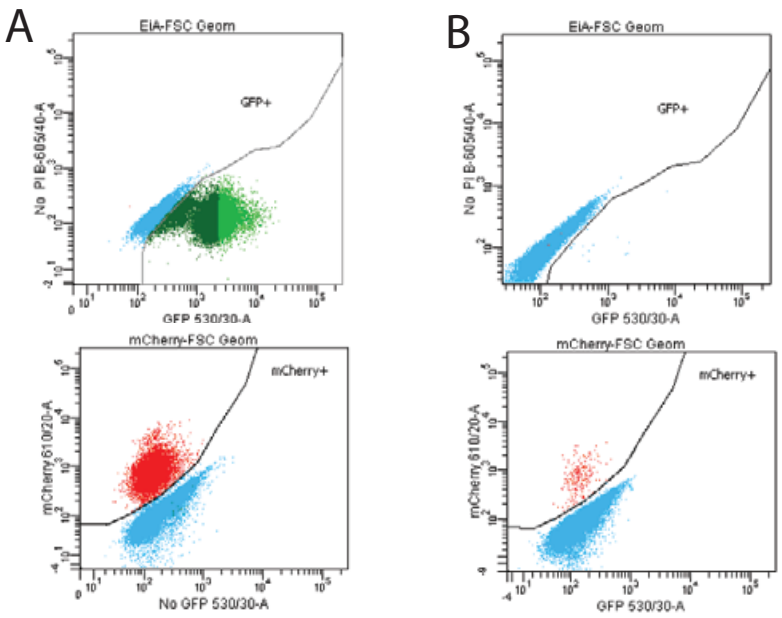

Figure 4.6: Selection with antibiotics and fluorescent reporter. All EiA and mCR populations were induced with 5μg/mL dox. (A) Cells were selected with 3μg/mL puro (EiA) and 200μg/mL g418 (mCR). (B) No antibiotic selection, sorting 72 hours after transduction.

with an antisense primer containing an MfeI site to amplify modc1 and modc2, individually, from previously created constructs. The resulting PCR fragment was used as a primer to amplify the mCherry sequence and add the modc tag to the resulting final PCR fragment which was then re-cloned into the BglII/MfeI sites of HRSneoMCiT2 to yield two new constructs: HRSneoM1iT2 and HRSneoM2iT2 (each containing modc-tagged mCherry in the first cistron). The final step was to create a tTRg version containing the short half-life modc1 tag. To do this, a similar two-step strategy was used. The end of tTRg (no stop codon) was incorporated in a primer to amplify modc1. The resulting fragment was used as a primer to amplify IRES-tTRg thereby adding the modc1 tag, and the resulting PCR fragment was religated into HRSneoM1iT2 to yield HRSneoM1iT1. Each of the intermediate complete vectors created throughout this cloning process was sequenced through the critical regions to confirm that no errors were introduced by PCR. The result of this molecular cloning was that I now had neomycin-selectable vectors for self-contained negative feedback portions of the oscillator circuit which allowed

for tracking of destabilized repressor via destabilized mCherry expression using two different half-life tags.

I generated clonal cell lines by FACS to eliminate the high level of false positive remaining after antibiotic selection (Fig 4.6). I had built the HRSpuroEiA constructs prior to finishing the destabilized mCherry negative-feedback constructs and thus I first generated positive-feedback clones by inducing the HRSpuroEiA population cell line with 5μg/mL dox and sorting for the brightest EGFP subpopulation. I generated several EiA clones and further characterized them with flow cytometry. The EGFP profiles for various levels of dox induction are shown in figure 4.7 for three representative clones. All of the positive-feedback clones displayed a bimodal switch-like response to doxycy-

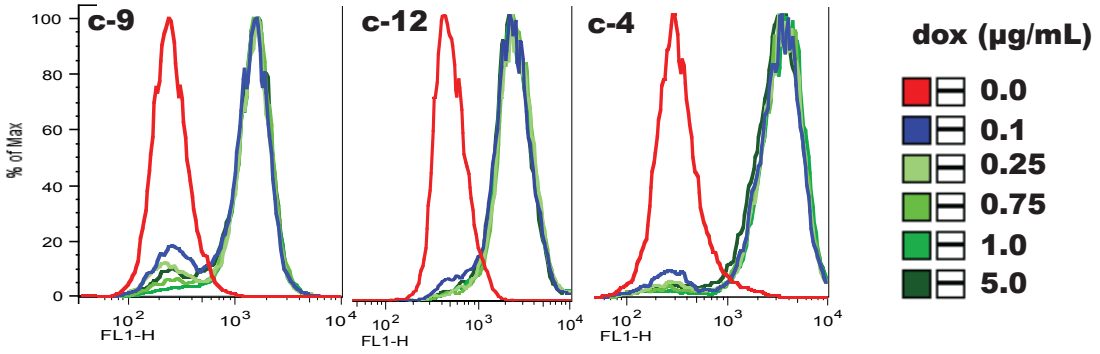

Figure 4.7: Positive feedback clones display bistability. In the presence of dox, cells switch to a high state of EGFP expression.

cline. In the absence of dox, all of the cells are in the OFF state since the transactivator rtTA is inactive. With the addition of dox, the transactivator is allowed to dimerize and bind to tetO sites which creates a positive feedback loop to make more transactivator and EGFP. Eventually the cells settle in a steady state of high transactivator/EGFP expression that is balanced by the degradation of these proteins. For the range of dox levels tested, virtually all of the cells reach the same ON state of high expression with no intermediate steady states between OFF and ON. This switch-like behavior of the positive feedback circuit is in line with previous studies that have characterized this type of tet-transactivator feedback loop (May et al., 2008; Kramer and Fussenegger, 2005; Longo

et al., 2010). It is interesting to note the difference in fold-change of EGFP expression for these clones compared to those constructed previously which express EGFP front the second cistron rather than the first. The EiA clones exhibit a much higher signal-to-noise (fold-change $\sim$10 from ON to OFF) compared to the AE clones (fold change $\sim$1.5, Fig 4.5B). This suggests that the first cistron is expressed more efficiently than the IRES-driven second cistron, but expression from the second position is adequate in the case of the constructs developed for this oscillator design given that enough transactivator protein is produced to confer the bimodal/switchlike behavior expected of a positive feedback transcriptional loop.

Having isolated functional positive-feedback clones in the form of the EiA cell lines, the next step towards the goal of a synthetic oscillator was to incorporate the negative feedback on top of the existing architecture in order to complete the dual-feedback design. As the timescale of generating stable cell lines can be on the order of weeks, I concurrently performed transient transfection experiments of the dual-feedback design into 3t3 cells to test the potential for oscillatory behavior of the complete circuit. Transfection efficiencies for each construct into 3t3 cells are typically less than 10%, and so the odds of a cell receiving both the positive and negative feedback constructs are fairly low. Approximately one out of a hundred cells displayed dynamic fluorescent behavior in both EGFP and mCherry channels during time lapse imaging. The results indicated that some cells have the potential for oscillatory behavior with an initial burst-like peak followed by long-lived decay of the signal before the initiation of another burst (Fig 4.8). In light of these encouraging transient transfection experiments, the next step was to genomically integrate the negative feedback constructs.

To generate the retrovirus for transduction of 3t3 cells, the HRSneoM1iT1 and HRSneoM2iT2 constructs were transiently transfected into the Phoenix-Eco packaging cell line, but this time I employed Fugene6 (Roche) lipid-based transfection reagent instead of the calcium phosphate precipitation method. Even more so than the $CaCl_2$ method, Fugene6 is extremely easy to use and not nearly as sensitive to environmental conditions in order to achieve high transfection efficiency (Jacobsen et al., 2004). The

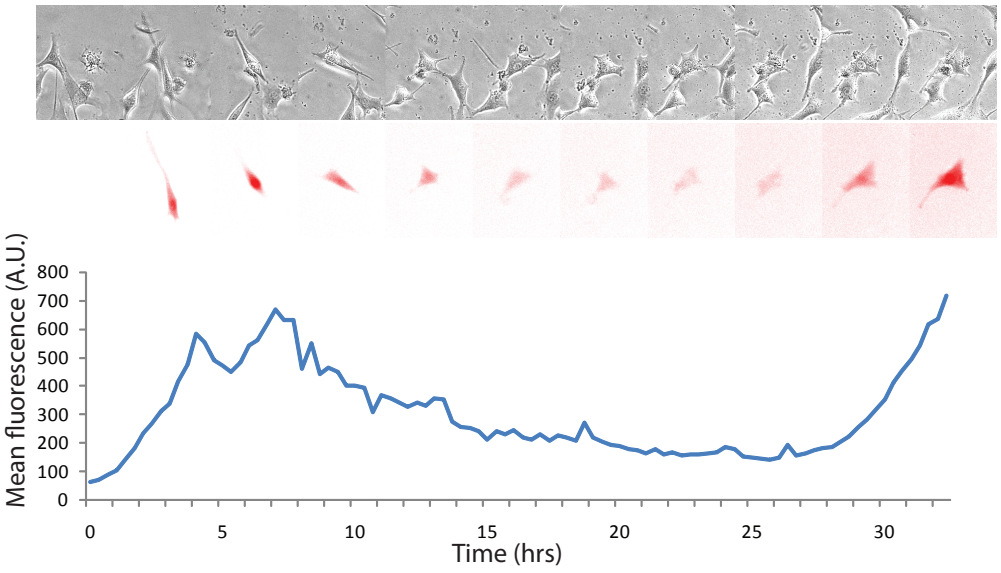

Figure 4.8: Transient transfection of EiA and m2it2 constructs into 3t3s. Time-lapse imaging of fluorescent reporter reveals the potential for oscillatory behavior in single cells. Phase and mCherry images (top) and corresponding fluorescence trajectory (bottom).

reagent is simply mixed with DNA to create a lipid-encased DNA complex within 15 minutes of incubation at room temperature, after which point it is applied dropwise to cells and incubated for 24-48 hrs. To achieve high transfection efficiencies, care must be taken to ensure that the ratio of DNA to reagent is not in excess of the recommended values, but there is no stringent pH or media composition requirement. Using Fugene6, Phoenix cells were readily transfected with the negative feedback constructs and the resulting virus was used to infect EiA clone 4 as well as control populations of wildtype 3t3 cells. Characterization of the resulting double-stable cell lines via time-lapse imaging revealed that activator dominates the circuit whenever doxycycline is present (Fig 4.9). The cells exposed to doxycycline gradually increase their production of EGFP and mCherry until a steady state fluoresence is reached and there is no apparent sign of a negative-feedback driven degradation of the fluorescent signal which would indicate the potential for oscillations. The functionality of the modc degradation tags was confirmed by inducing cells with doxycycline for 24 hours and then removing the inducer and ob-

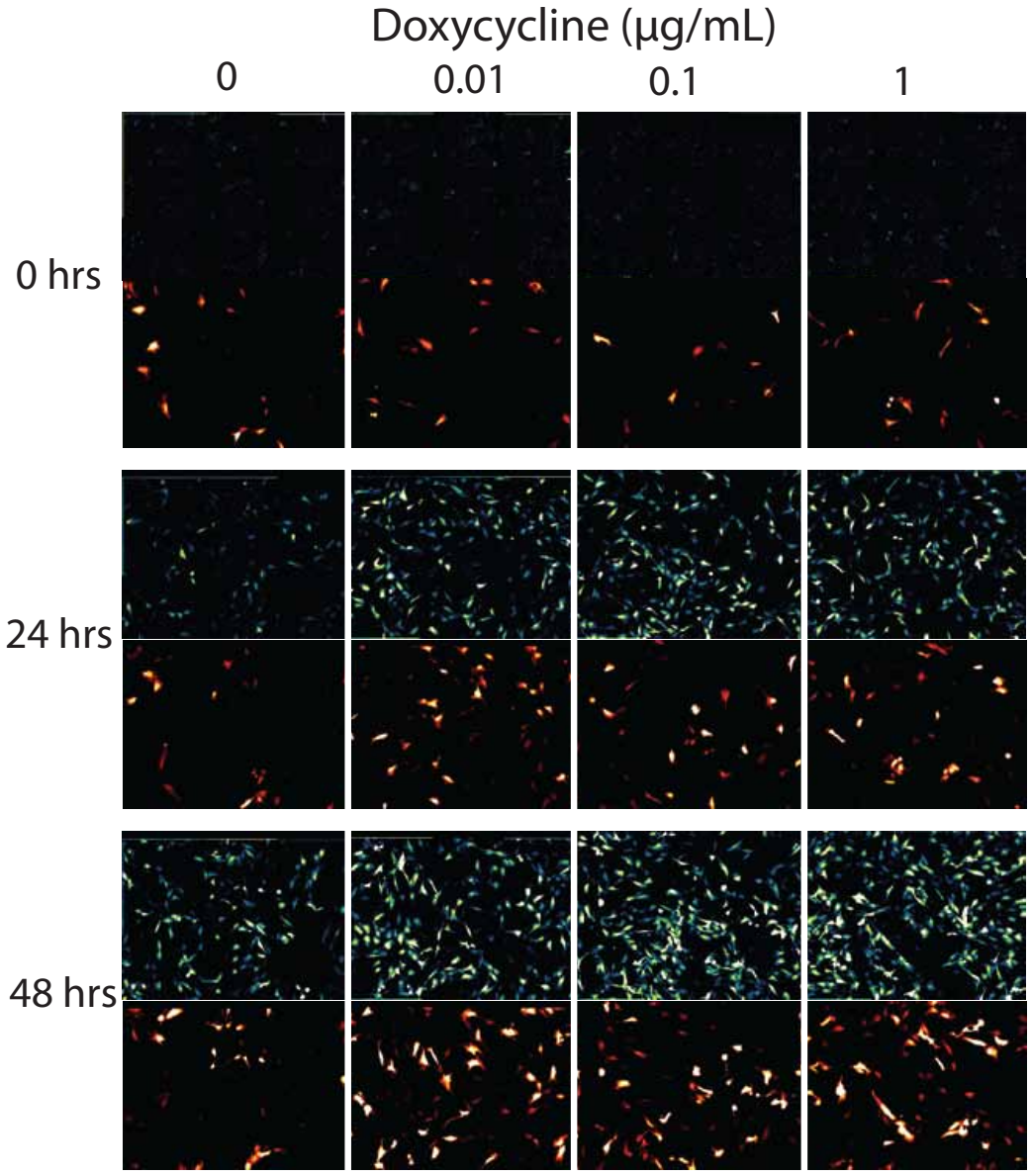

Figure 4.9: Tet dual-feedback stable cell line. EiA clone 4 stably transduced with m1it1 construct. Cells were induced with the indicated levels of doxycycline and cultured at 30°C during time-lapse imaging to retard cell motility. Images were captured every 20 minutes to enable oservation of fluorescent reporter dynamics in single cells, but the signal of both EGFP and mCherry for cells exposed to dox increases monotonically over the course of 48 hours without any apparent oscillations.

serving the decay of the fluorescent signal (Fig 4.10). Both EGFP and mCherry tagged

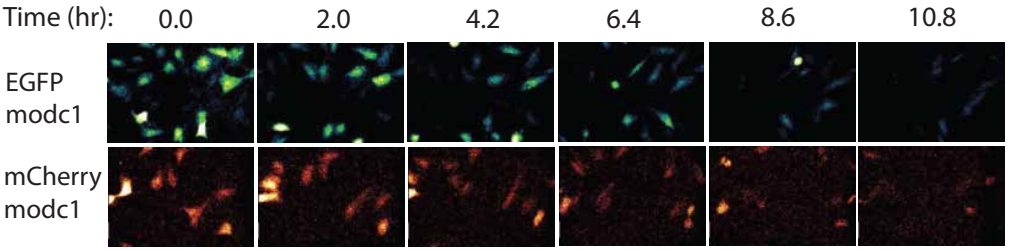

Figure 4.10: Destabilized fluorescent reporters are rapidly degraded. EiA clone 4 stably transduced with m1it1 was induced with 1μg/mL dox for 24 hours prior to time-lapse imaging in fresh media without inducer. The rapid decay of fluorescent signal for destablizied EGFP and mCherry confirms the functionality of the modc degradtion tags.

with modc1 exhibit rapid signal decay on the order of several hours, indicating that the destabilized proteins are being rapidly turned over and thus oscillations are not being prevented by a lack of protein degradation. Rather, it appears that in the presence of the inducer (dox), the activated transactivator (rtTA) dominates control of expression and out-competes the partially inactivated transrepressor (tTRg).

Indeed, a theoretical study of transcription factor competition at the promoter level was published concurrently with my synthetic oscillator development effort and its results indicate that oscillations are less favored when activator and repressor compete for the same promoter binding sites (Munteanu et al., 2010). To promote oscillations in a dual positive and negative feedback design, the most desirable configuration appears to be one in which activator and repressor bind separate operator sites in a non-competitive manner. Such non-competition leads to a larger parameter space for which robust oscillations with a characteristic frequency and confined amplitude predominate. On the other hand, the case of competition at the promoter tends to produce noisy pulse-like oscillations with long and variable decay times between peaks.

4.3 Redesign of circuit components

With these experimental and theoretical results in mind, I redesigned the synthetic mammalian oscillator circuit to allow for non-competition of the repressor and activator at the promoter level. This required changing the DNA-binding portion of one of the transcription factors and adding the corresponding operator sites in front of the mCMV promoter. I chose to modify the transactivator by replacing the tetR-based DNA-binding domain of rtTA with an erythromycin-responsive DNA-binding protein. Such a macrolide-based chimeric transcription factor was first developed by Weber et al. (2002) and has been successfully used in a variety of subsequent mammalian synthetic gene circuits (Weber et al., 2008; Kramer and Fussenegger, 2005; Kramer et al., 2004). The chimeric erythromycin-responsive transactivator (ETA) is analogous to the tetracycline-repsonsive rtTA as it retains the VP16 activation domain but replaces the tetR DNA-binding portion with an EthR domain that allows binding to EthR operator sites. In this manner, a new hybrid promoter design containing eight tandem EthR operator sites etO8 in addition to the seven tet operator sites (tetO7) allows for non-competition of the new transactivator (ETA) with the tet-based transrepressor (Fig 4.11).

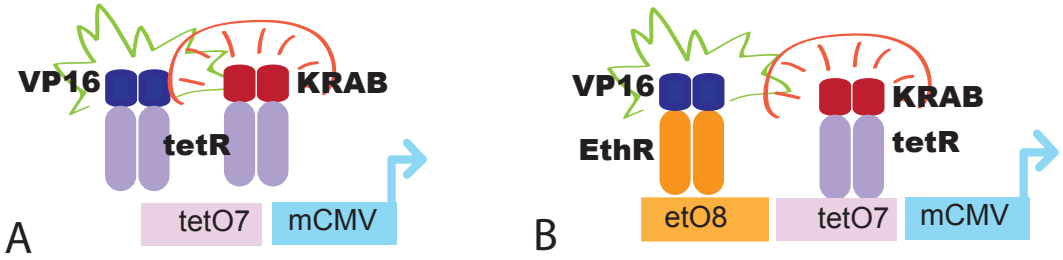

Figure 4.11: Hybrid promoter redesign for non-competition of transcription factors. (A) In the original tet-based design, activator and repressor both contain tetR as the DNA-binding domain which results in competition for the seven tet operator sites proximal to the promoter. (B) A non-competitive redesign replaces the tetR domain of the activator with an EthR DNA-binding domain that binds to unique etO sites.

To incorporate ETA in my constructs, I obtained plasmid pTZ3509 from Dr. Norihisa Noguchi (Tokyo University of Pharmacy and Life Science, Japan) which contains the mphR(A) gene encoding EthR (Noguchi et al., 1995). Double fusion PCR (Wach, 1996) was carried out to fuse EthR to VP16modc1. Specifically, EthR was amplified by PCR using primers to add a 5' BglII site and a 3' homology to VP16 to create fragment 1 for the double-fusion reaction, and vp16modc1 was amplified from HRSpuroEiA to create fragment 2. The two fragments were then joined in second-round PCR reaction to create EthR-VP16modc1, or ETA, which was then cloned into the BglII/SnaBI sites of HRSpuroAE to replace rtTAmodc1. Although I had previously reported that EGFP was not efficiently expressed from the second cistron, I built the ETA construct in this configuration because the molecular cloning was much less complicated given the presence of the SnaBI site and it appeared that the destabilized mCherry is a much better fluorescent reporter than EGFP in any case for mammalian live-cell imaging. The reason for this is that mammalian culture media typically contain a variety of flavins which contribute a large amount of background autofluorescence in the GFP channel (Ludin et al., 1996).

To construct the eight tandem EthR operators, two ultramers were synthesized (IDT, San Diego, CA) each containing four tandem repeats of the operator and a 3' terminal linker region (ATTTAGGGATAAACGATTGAA). The sequence of the EthR operator is GATTGAATATAACCGACGTGACTGTTACATTTAGG. The ultramers were joined by PCR and amplified by short flanking primers. The 5' region of each ultramer contains homology to the HRS vector for etO8 insertion upstream of tetO7. Specifically, the HRSneoR vector I created contains a single HindIII restriction site just upstream of the tetO7 sequence, which allowed linearization of the vector and incorporation of the etO8 synthesized sequence by non-amplifying PCR in the form of circular polymerase extension cloning (CPEC) (Quan and Tian, 2009). I discovered that the repeating nature of the EthR operator sequence was highly susceptible to recombination at the E. coli transformation step which resulted in tandem repeats of two, three and five operator sites. I settled on using the etO5 tandem sequence as a good option that should pro-

vide enough cooperativity to assure a high level of transactivation by ETA. The etO5 sequence was ported into the positive feedback vector containing ETA by a CPEC reaction to join an etO5tetO7 PCR fragment with a second PCR fragment consisting of the positive feedback vector itself. For the negative feedback constructs, the HRSneoR vector now containing the etO5tetO7 hybrid promotor was digested with BglII and ageI to remove R (tTRgmodc2) and replace it with the mCherry-modc1-IRES-ttRGmodc1 and mCherry-modc2-IRES-ttRGmodc2 fragments. Finally, the backbone from these two resulting vectors was PCR amplified in a manner that excluded tetO7 and the resulting fragment was religated to create negative feedback vectors containing etO5 sites as the sole operators in front of mCMV. A summary of the vectors created is presented in table 4.4. The designation for each construct follows a nomenclature where the operator sites are listed first (E5 for etO5 and T7 for tetO7), followed by the protein in the first cistron (e for ETA or m for mCherry) and a number indicating modc1 or modc2, i for IRES and then the protein in the second cistron (t for tTRg or g for EGFP) and its respective modc tag. Since there are two different hybrid promoter architectures of the positive feedback (A and B constructs) as well as the negative feedback (C,D,E and F), different modes of coupling can be achieved which are summarized in figure 4.12.

Table 4.4: Erythromycin and tetracycline regulatable transcriptional feedback constructs allow for various modes of coupling positive and negative feedback

Reference	Designation	operators	1^{st} cistron	2^{nd} cistron	selection
A	E5T7e1ig1	etO5,tetO7	ETA-modc1	EGFP-modc1	puro.
B	T7e1ig1	tetO7	ETA-modc1	EGFP-modc1	puro.
C	E5T7m1it1	etO5,tetO7	mCherry-modc1	tTRg-modc1	G418
D	E5T7m2it2	etO5,tetO7	mCherry-modc2	tTRg-modc2	G418
E	E5m1it1	etO5	mCherry-modc1	tTRg-modc1	G418
F	E5m2it2	etO5	mCherry-modc2	tTRg-modc2	G418

The critical regions of each of the six constructs A-F was confirmed by sequencing and transfection of Phoenix-Eco cells was performed using Fugene6 to create the retrovirus for infection of target 3t3s. Successful fluorescent reporter expression seemed to confirm proper functionality of each circuit (Figure 4.13). Specifically, the A con-

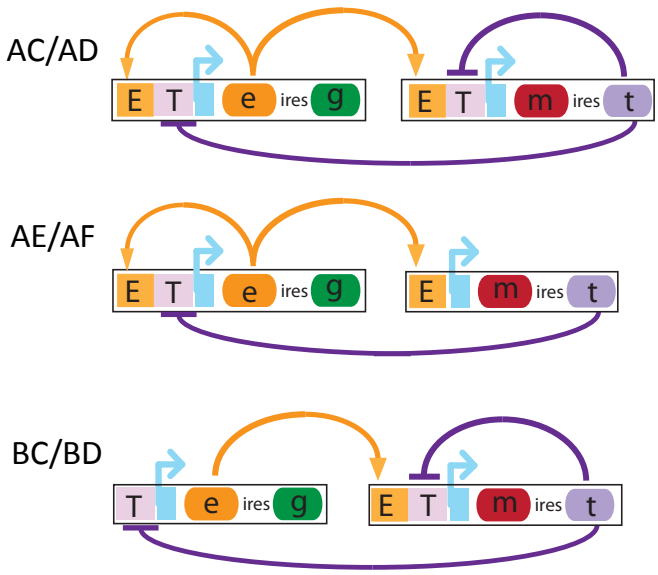

Figure 4.12: Various coupling combinations of positive and negative transcriptional feedback

struct exhibited much higher destabilized EGFP fluorescence than B, indicating a functional positive feedback loop by the ETA transactivator. Unlike the rtTA transactivator which becomes active only in the presence of the inducer doxycyline, the EthR portion of ETA has the reverse pharmacology for its inducer and ETA is active in the absence of erythromycin. All versions of the negative feedback constructs (C-F) expressed destabilized mCherry fluorescent protein, and the lower levels of expression for C and D compared to E and F indicated that negative feedback was functional for the former pair where tTRg could exert its action on the promoter via tetO7 sites which are absent in the E and F constructs.

Each construct was stably transduced into target cells by harvesting the retroviral supernatant from the Phoenix cells and applying it to cultures of wildtype 3t3 cells as before. Transductants of constructs A and B were selected with 3μg/mL puromycin and C-F were selected with 400μg/mL G418 in the presence of 1μg/mL doxycycline in order to inactivate any repressor which might interere with expression of the neomycin resistance gene. The transduced cell populations were analyzed by flow cytometry after

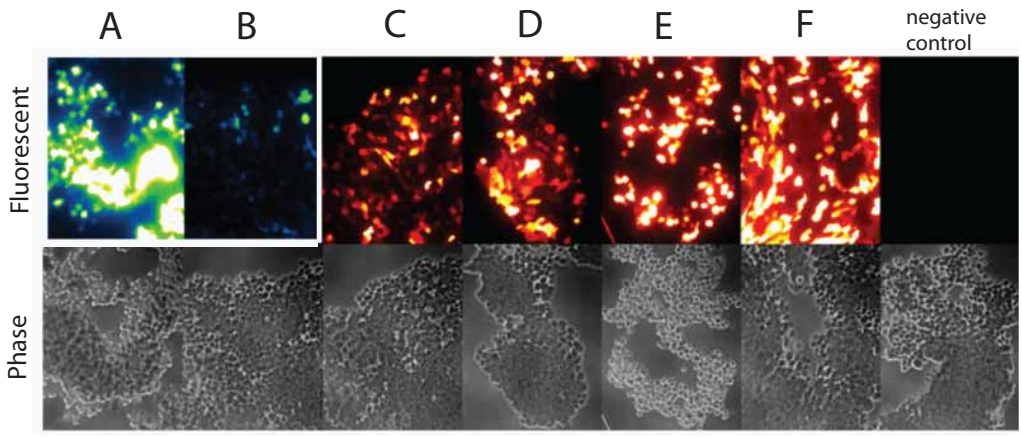

Figure 4.13: Transient transfection of Phoenix-Eco cells. Efficient transfection and expression of each construct (A-F) is confirmed with fluorescent microscopy.

several days of antibiotic selection. No doxycycline or erythromycin was added prior to analysis. The EGFP and mCherry fluorescent density plots for each single-stable population are shown in figure 4.14, with percent positive cells for each fluorescent gate displayed in the upper right corner. Population A consist of 28% EGFP positive cells as opposed to $\sim$0% for population B, which indicates that the presence of the etO5 sites in A allows for functional positive feedback in the absence of erythromycin in 3t3 cells. The EGFP distribution of population B is nearly identical to wildtype 3t3 (blue background distribution) which suggests that the highly destabilized EGFP-modc1 expressed from the second cistron results in virtually no basal background fluorescence in the absence of positive feedback. In terms of the negative feedback, populations C and D should be able to engage in tTRg repression of the tetO7 promoter in the absence of doxycycline, while populations E and F lack the tetO sites in front of the mCMV promoter. The percent positive mCherry cells for C and D is $\sim$3%, which is much lower than the corresponding modc1 or modc2 mCherry constructs in the E and F populations characterized by $\sim$20% positive cells. The difference in fraction of fluorescent cells in C and D compared to E and F indicates that a functional autoregulatory negative feedback by tTRg in the former populations is responsible for the lower signal as expression of

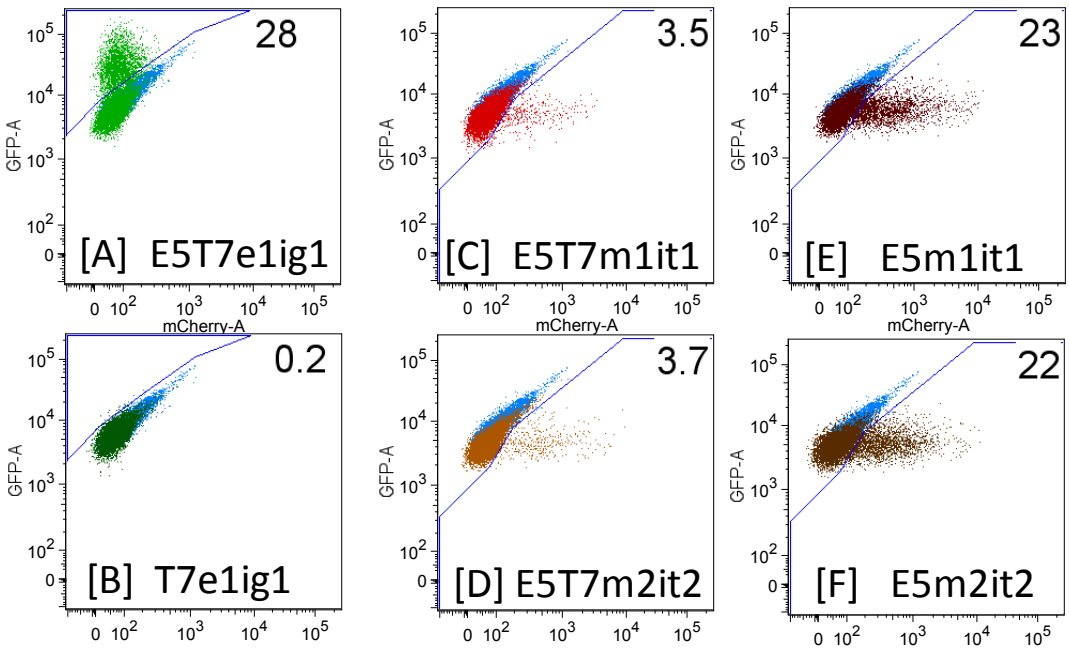

Figure 4.14: Single-stable 3t3 cell populations. Fluorescence density plots of EGFP (y-axes) and mCherry (x-axes) expression in stably transduced populations (A-F). Untransduced wildtype distributions are displayed in light blue. Gates are indicated by purple lines and percent positive cells is shown in the upper right corner of each plot.

mCherry in some cells is turned off by tTRg silencing of its own promoter.

Given our understanding of the bacterial oscillator which indicates that activated repression is required for robust oscillations, I generated double stable 3t3 transduced populations concurrently with the single-stable lines in an effort to rapidly generate dual-feedback designs. This was performed simply by infecting target cells with a mixed population of retrovirus to generate the combinations of feedback desribed previously in figure 4.12. The double-stable cell lines were all selected with the full complement of antibiotics: 3μg/mL puromycin, 400μg/mL G418 and 1μg/mL doxycycline inducer for several days. The EGFP and mCherry profiles of the six resulting populations were again assayed by flow cytometry and are shown in figure 4.15. An immediate observa-

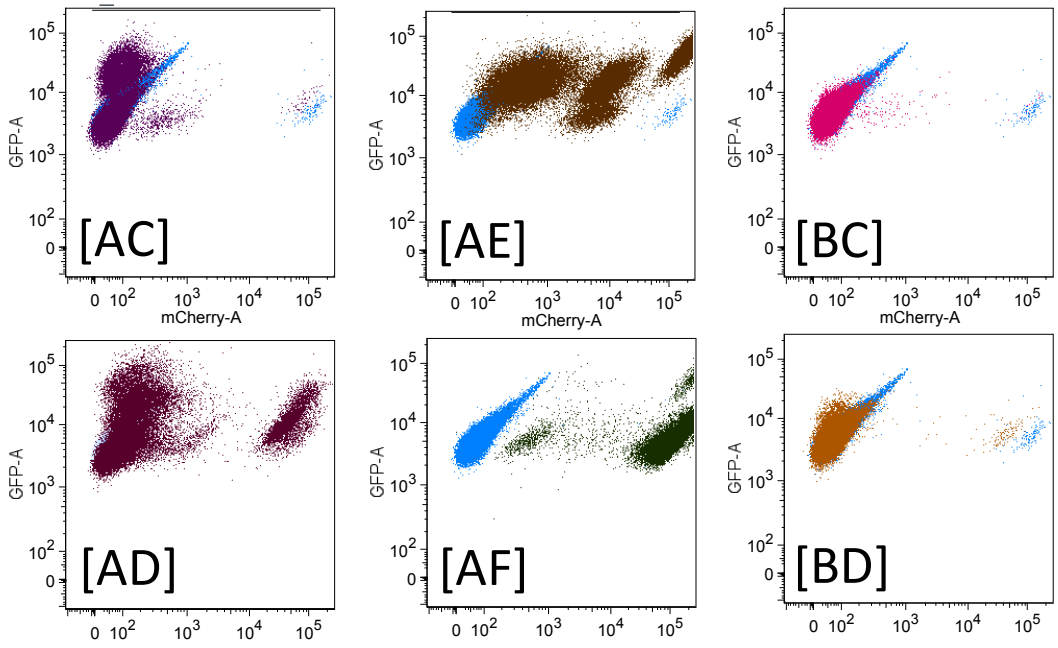

Figure 4.15: Double-stable 3t3 cell populations. Fluorescence density plots of EGFP (y-axes) and mCherry (x-axes) expression. Untransduced wildtype cells are shown in light blue.

tion is that the BC and BD populations are essentially identical to wildtype 3t3 in that the vast majority of cells exhibit no EGFP or mCherry fluorescence. This is readily explained by the lack of a positive feedback loop in the B constructs which do not have

etO5 sites to enable autoregulation by ETA. The profiles of the remaining populations (AC,AD,AE and AF) are interesting in that each of them is characterized by several subpopulations within the GFP/mCherry parameter space. This can be explained by considering the fact that viral recombination can readily occur between homologous sequences of DNA within the retroviral vector (Hu and Temin, 1990; Stuhlmann and Berg, 1992) and that my constructs are characterized by such sequences in the first and second cistron in the form of modc tags for the first and second protein. In this manner, a variety of recombination events can produce subpopulations that are any combination of the four components: mCherry, EGFP, tTRg and ETA. For example, in the AE population, the most highly fluorescent subpopulation in both EGFP and mCherry (top-right corner of density plot) likely does not contain the tTRg repressor. Given the presence of multiple subpopulations, it is difficult to tease out time-dependent dynamics of autoregulatory repression by tTRg using only flow cytometry. Single-cell time-lapse imaging is much better suited for this task and can quickly sweep a large parameter space of inducer concentrations by using a multi-well plate format.

Imaging experiments to characterize the double-stable populations were performed by seeding cells in glass-bottom multi-well plates (96-well or 24-well format) with increasing erythromycin and doxycycline concentrations along the two axes of the plate (Figure 4.16). Visual analysis of stacks of time-lapse images for each combination of erythromycin/doxycycline inducer allows qualitative detection of oscillatory behavior, but none was readily visible for the AE cells characterized in this manner. Fortunately, the 96-hour post-induction images indicate that the cells respond to erythromycin as expected. At low concentrations of EM the activator is activated and can exert positive feedback to turn on fluorescent reporter production in the negative feedback construct containing etO5 sites. This fluorescent signal is abolished at high EM concentrations which inactivate ETA and shut down the positive feedback loop. A response to doxycycline can also be detected, as higher concentrations of dox produce a stronger mCherry signal by the shutting down the negative feedback loop allowing a higher-constitutuive expression level from the non-repressed promoter.

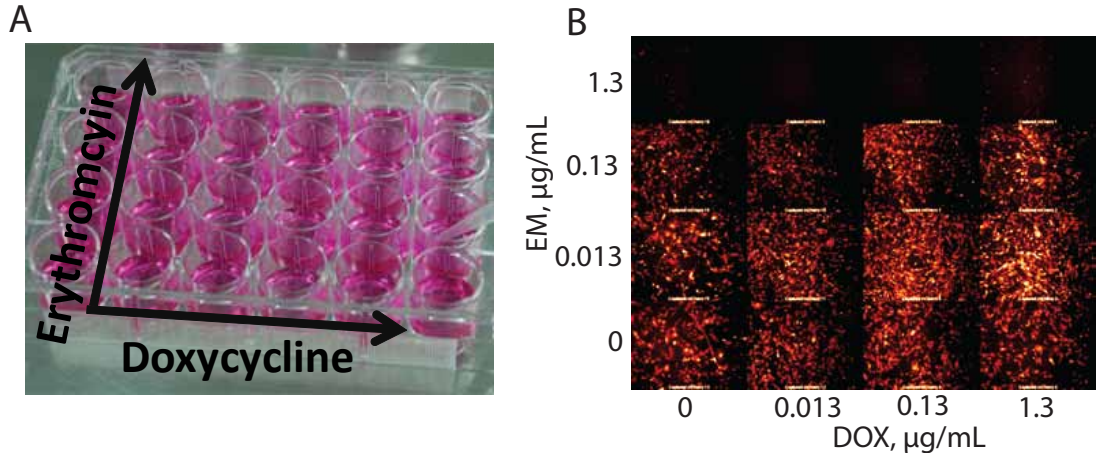

Figure 4.16: Multiwell time-lapse imaging. (A) Induction along two axes with Erythromycin and Doxycycline allows for a rapid sweep of the parameter space of activation and repression. (B) mCherry fluorescence of cells in 16 individual wells after 96 hours of induction at indicated concentrations of inducers. All wells are confluent with cells (phase images not shown)

To attempt to tease out the dynamic behavior of the circuit in single-cells, the time-lapse images were segmented and tracked using CellProfiler open-source image analysis software (Carpenter et al., 2006). I discovered that on the timescale of tens of hours, the high motility of 3t3 fibroblasts causes neighboring cells to come in frequent contact and the morphology of the cells is such that very thin cell edges have little contrast and cell boundaries of neighbors become indiscernable. In addition, the large cell area change associated with the motility of fibroblasts has a significant noise effect on the low signal intensity mCherry fluorescence trajectories. I concluded that a much better choice of cell line for dynamic fluorescence measurements is the commonly used workhorse of biotechnology, the Chinese Hamster Ovary (CHO) cell line. This cell line exhibits very low motility compared to fibroblasts and is almost exclusively used by the Martin Fussenegger group which is currently a global leader in mammalian synthetic biology.

4.4 Reconstruction of circuits in CHO cell line

CHO cells are a hamster-derived cell line which is not readily infectable with the murine retroviral system I was using. Fortunately, I was able to find a CHO cell line which had been modified to stably express the murine ecotropic receptor to enable infection by MoMuLV retrovirus (Hubbard et al., 1994). This cell line was kindly provided to me by Dr. Elaine Muchmore (Univ. of CA, San Diego) and I was able to rapidly generate transduced populations using my established protocols.

From my characterization of the synthetic circuits in fibroblasts, I had learned that functional positive feedback is relatively easy to establish since sorting to enrich for the most highly fluorescent cells readily isolates the ones that have transactivator producing a high level of fluorescent reporter. On the other hand, functional negative feedback is somewhat trickier to identify and isolate given the low magnitude change in fluorescence between non-repressing and autoregulated repression conditions. With these considerations in mind, I chose to initially focus on producing CHO cells with intact functional negative feedback before attempting to re-create the positive feedback portion of the circuit. I transfected the E5T7m1it1 (C) and E5T7m2it2 (D) constructs into Phoenix cells for generation of retrovirus, and I transduced CHO and wild type 3t3 control populations as before and analyzed the resulting populations with flow cytometry. While the 3t3 cells showed tranduction efficiencies of 3% for both C and D constructs similar to what I reported previously in figure 4.14, the CHO cells had ten-fold lower efficiences of $\sim$0.3%. Presumably this was the result of a suboptimal level of murine ecotropic receptor expression, and so I used bulk FACS to sort the CHO cell populations to enrich for mCherry positive cells after induction with 1μg/mL doxycycline for two days. I then tested the enriched populations for response to doxycycline and observed three distinct subpopulations. The predominant subpopulation (80-85%) was identical to wildtype CHO and had no mCherry expression but was G418 resistant. The remaining 15-20% of cells clustered into two separate subpopulations characterized by high and low fluorescence, respectively. The highly fluorescent subpopulation did not change the

mCherry distribution in response to dox, indicating that a functional repressor was not present in this cell group. On the other hand, the low fluorescent subpopulation showed a shifting mCherry distribution with increasing fluorescence at higher dox values, indicative of active repression at zero doxycycline and gradually inactivated tTRg with more dox (Fig. 4.17). This behavior was apparent for both the C and D constructs, and the shift in fluorescence distribution was most prominent after 70 hours of induction. The fold change of the mean mCherry signal from maximal repression at zero doxycycline to no repression at 100 ng/mL dox was 1.5 to 2, which can be expected given the basal expression rate from the minimal CMV promoter should be fairly low in non-repressing conditions. A functional negative feedback suggests that oscillations can potentially be observed. Given that the functional subpopulation represents $\sim$10$\%$ of cells in each of the C and D construct CHO cell lines, time-lapse imaging to search for such behavior among a large number of non-responding cells was not practical at this point. I decided to perform bulk FACS again to enrich for the dox-responsive cells and I characterized the resulting populations using flow cytometry. The same three distinct subpopulations were evident for each construct, and the dim mCherry subpopulation now represented 61$\%$ and 88$\%$ of total cells for the C and D constructs, respectively (Fig 4.18A). Induction with doxycycline confirmed that these subpopulations of cells respond to increasing dox levels by a shift in the fluorescence distribution of the mCherry signal (Fig 4.18B). I performed time-lapse imaging to characterize the dynamics of the mCherry signal in these negative feedback cell lines to attempt to detect oscillatory behavior by qualitative analysis of the image stacks. Individual cells appeared to show change in fluorescence as a function of time over the course of 24 hour experiments. As some cells appeared to have greater dynamic range in mCherry signal than others in these mixed populations, I decided to generate clonal cell lines in order to isolate a several cell lines with readily detectable changes in fluorescence during autorepression. Given that I had fairly high fractions of dox-responsive cells for both the C and D constructs after having performed the second bulk FACS enrichment step, I concluded that serial dilution cloning would be an efficient way to generate an unbiased selection of clones from the parent popu-

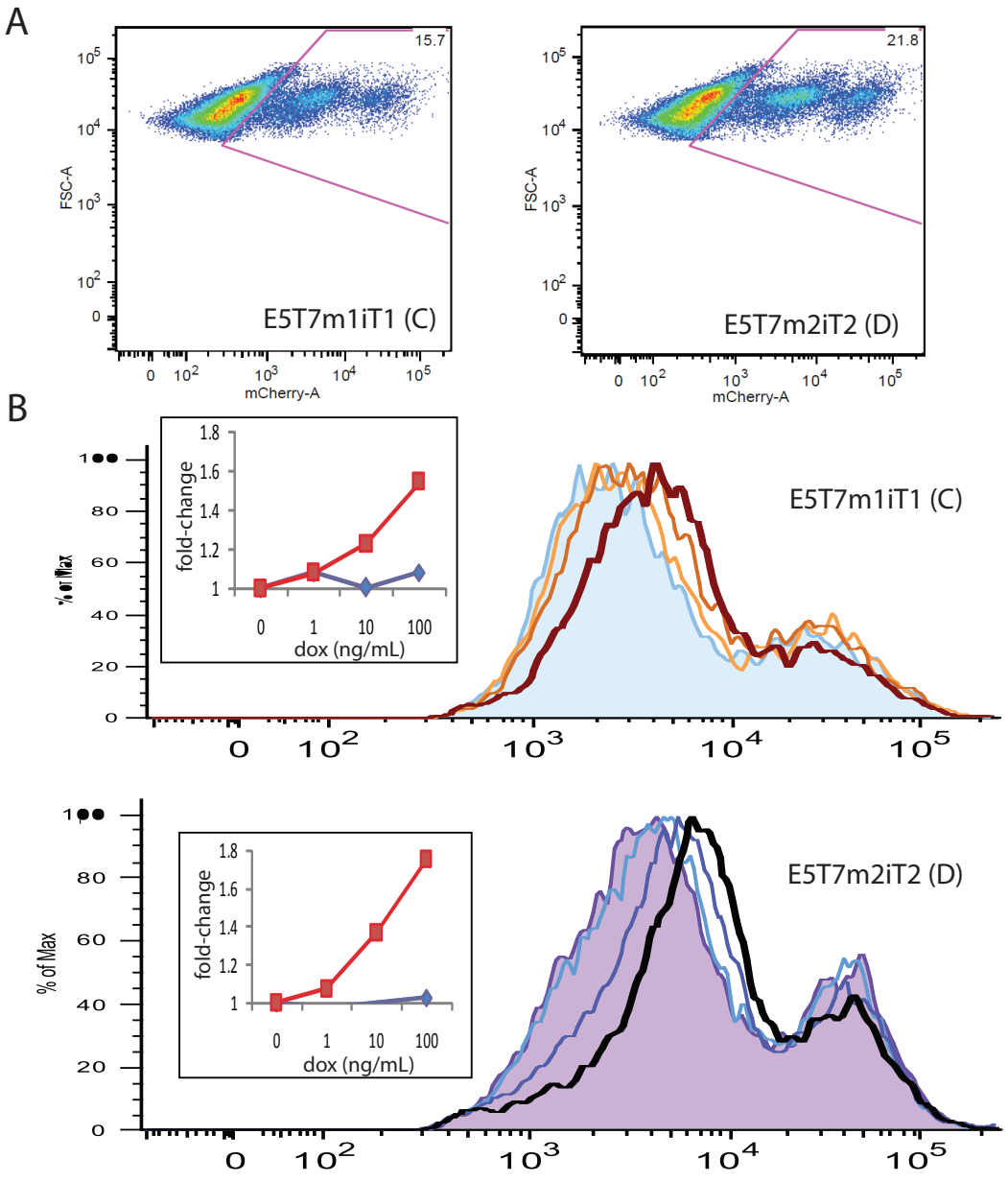

Figure 4.17: Screening for functional negative feedback in CHO subpopulations. (A) CHO cells transduced with C and D negative feedback constructs each display three distinct subpopulations: non-fluorescent cells, low mCherry expression and high mcherry expression. (B) mCherry distributions of C and D fluorescent subpopulations (as gated in A) after doxycycline induction at 0, 1, 10 and 100 ng/mL dox. The dominant fluorescent peak in each distribution represents the low mCherry subpopulation and displays an increasing mean fluorescence as a function of increasing dox levels. The fold change of this peak mean fluorescence compared to 0 dox is displayed in red in each inset, as well as the fold change of the non-responding high fluorescence peak which is shown in blue.

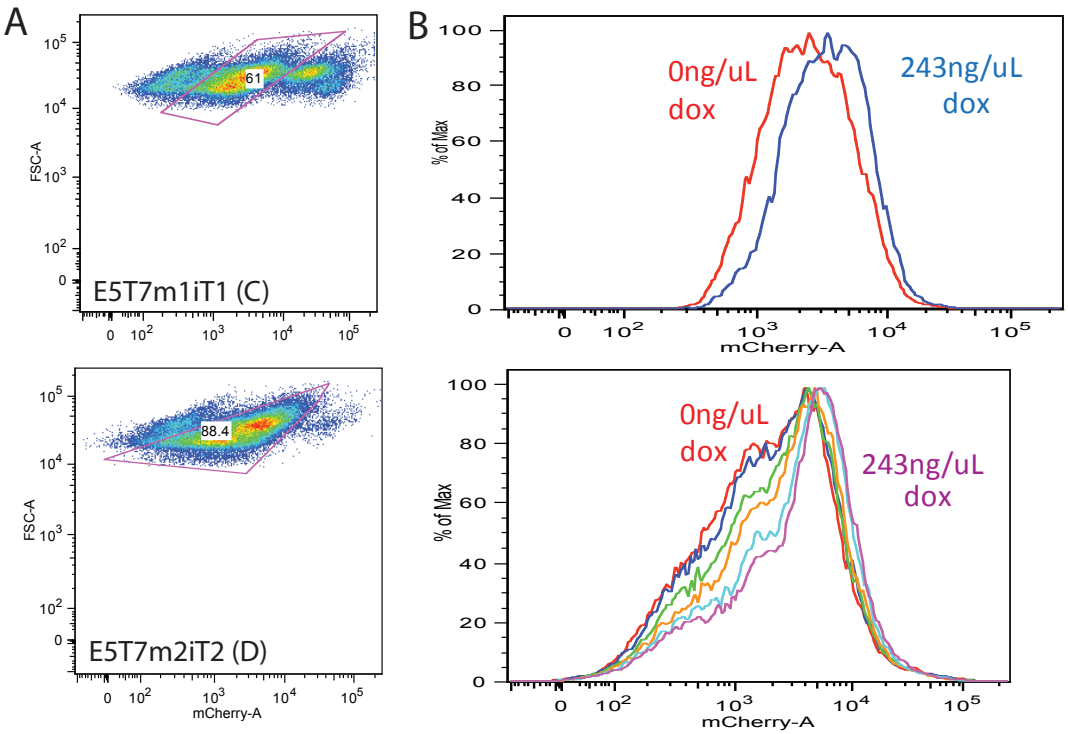

Figure 4.18: Enriched negative feedback CHO populations. (A) Density plots indicate that low mCherry expressing subpopulations now dominate the enriched C and D populations. (B) Each of the subpopulations gated in A responds to doxycycline. Top plot is C subpopulation mCherry histogram at 0 and 243ng/mL dox, bottom is D subpopulation histograms for a range of dox values: 0, 3, 9, 27, 81 and 243 ng/mL (increasing mean fluorescence from left to right)

lations. Briefly, the serial dilution method involves a 96-well plate, the first column of which is seeded with a serial dilution of cells, which is then expanded along the rows of the plate by further serial dilution. Hence the density of cells deposited into each well along the row of wells decreases exponentially until only a single cell is present in one of the wells. This is visually confirmed one day after seeding and such wells are marked for further expansion of the clones. In this manner I generated 10 clones for the C construct and 10 clones for the D construct, and these were screened for doxycycline response using flow cytometry (Fig. 4.19). Somewhat confoundingly, while the original cell populations used for seeding of clones had high fractions of dox-responsive cells, the majority of clones generated did not exhibit a dox response (14 out of 20). Of the C construct clones, two clones show a change in mCherry fluorescence in response to dox (C-2 and C-3). For the D construct, four clones exhibit a dox response and most interestingly, D-2 and D-7 are characterized by an extremely broad fluorescent signal distribution for fully active autorepression (zero doxycycline). This was very encouraging, since such a broad distribution, as evident primarily in clone D-2, is strongly indicative of oscillations. This is because an oscillating group of cells is expected to be characterized by some ”OFF” and ”ON” cells at the low and high end of the distribution, respectively, as well as many cells with fluorescence values in between these two states as they undergo a transition from ”OFF” to ”ON” and vice versa.

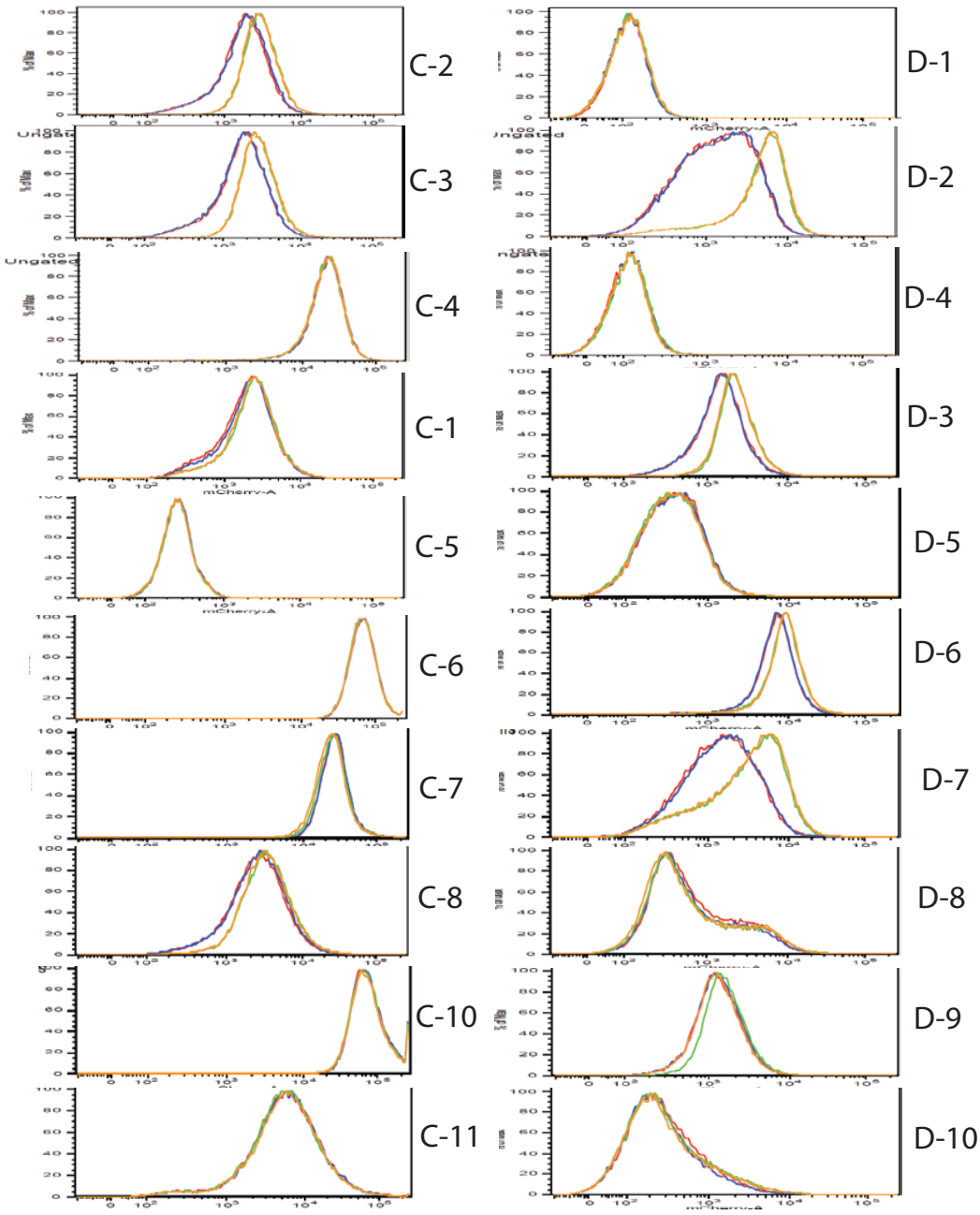

Figure 4.19: Screening CHO clonal lines. Ten clones were generated from each C and D enriched population and are labeled/numbered accordingly. To screen for response to doxycycline, each clone was cultured with 0 ng/mL or 243 ng/mL dox in duplicate and flow cytometry analysis was performed to generate the mCherry fluorescence distributions shown. Blue/red histograms correspond to zero dox, while orange and green are at 243ng/mL dox.

4.5 Characterization of negative-feedback dynamics and generation of dual-feedback clone library

Time-lapse fluorescence microscopy reveals oscillatory expression of destabilized mCherry reporter in single-cells of CHO clone D-2 in the absence of doxycycline (fully active repressor tTRg) (4.20A). I minimized cell migration to facilitate tracking of individual cells by decreasing the culture temperature to $32°C$ to suppress motility and proliferation (Kaufmann et al., 1999; Tigges et al., 2010). Individual trajectories were obtained manually by creating masks of cell outlines in the phase image channel which were overlaid onto the fluorescent images to measure the median signal intensity. Analysis was performed using ImageJ (Abràmoff et al., 2004). The period of oscillations at this temperature is on the order of $\sim$60 hours. Experiments at $37°C$ indicate a shorter period of $\sim$20 hours and rapid cell division with a doubling time of 15-18 hours at this temperature leads to a higher rate of dilution and thus a lower peak signal intensity. Virtually all cells in the field of view exhibit dynamic fluorescent reporter expression and a four-day time-lapse experiment at $32°C$ captures at up to two peaks for individual trajectories.

The shape of the individual oscillation peaks is characterized by a rapid rise in fluorescence on the upslope followed by a long-lived decay on the downslope (Fig 4.21B), which fits well with our understanding of this type of degrade-and-fire model of delayed negative feedback oscillations (Mather et al., 2009). Essentially, such oscillations consist of an initial burst of promoter activity and protein production while existing repressor concentration is too low to prevent transcription, followed by a long degradation phase of the active repressor until its concentration drops below a certain threshold and the cycle can repeat. Due to the inherent stochasticity of the biochemical reactions, the amplitude of the negative-feedback-only (NFO) oscillations can vary, but the shape of the trajectory is preserved. The noisiness of the NFO mammalian oscillator is apparent by observing the irregularity of the oscillations in single-cell trajectories (Fig

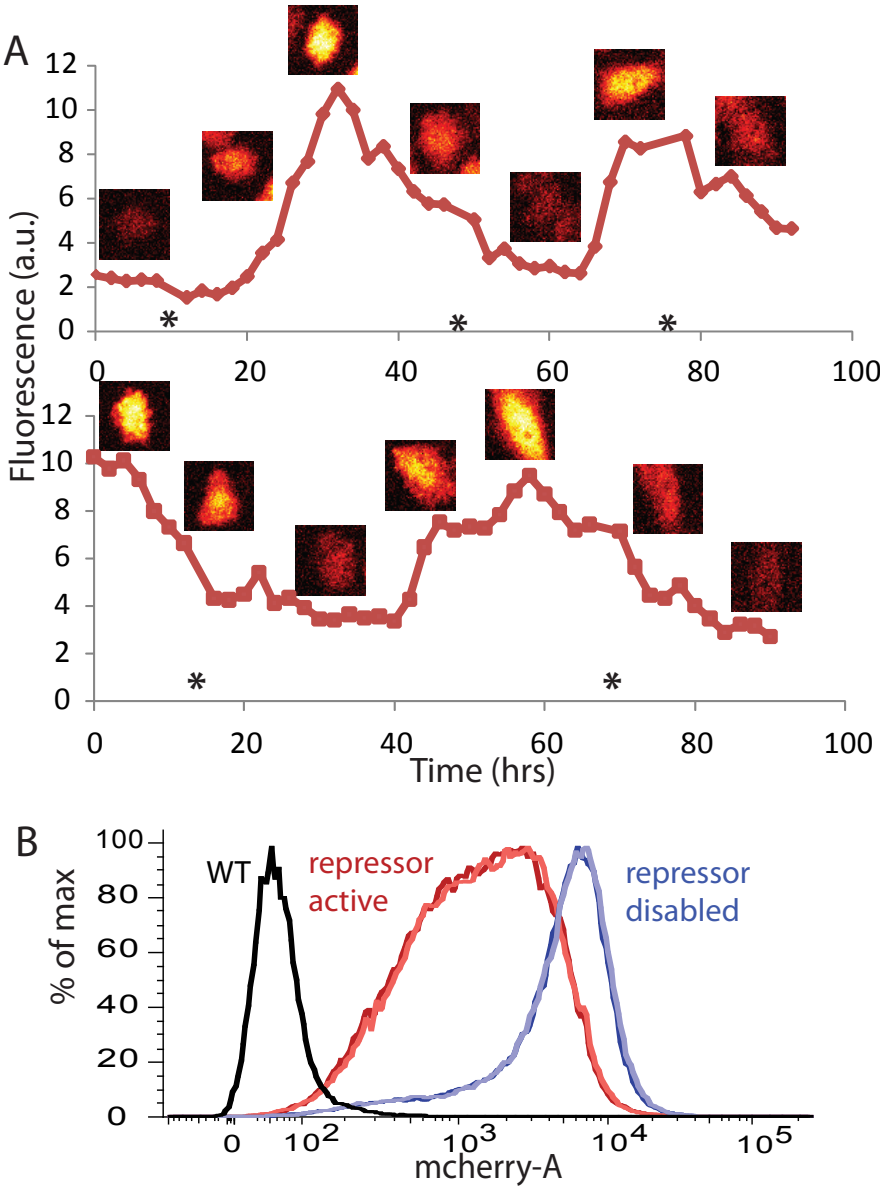

Figure 4.20: Negative feedback dynamics of CHO clone D-2. (A) Live fluorescent time-lapse imaging of individual cells at $32°C$ indicates oscillatory behavior when no doxycycline is present. Cell division events indicated by a star on the x-axis were excluded due to increased fluorescence in rounded cells undergoing mitosis. (B) Flow cytometry analysis of the clonal population after 2 days of induction indicates that cells with inactivated repressor (blue curves, 243ng/mL dox) exhibit a much narrower, higher fluorescence peak than cells with active repressor (red curves, zero dox) characterized by a very broad distribution indicative of out-of-phase oscillations (duplicate experiments are shown).

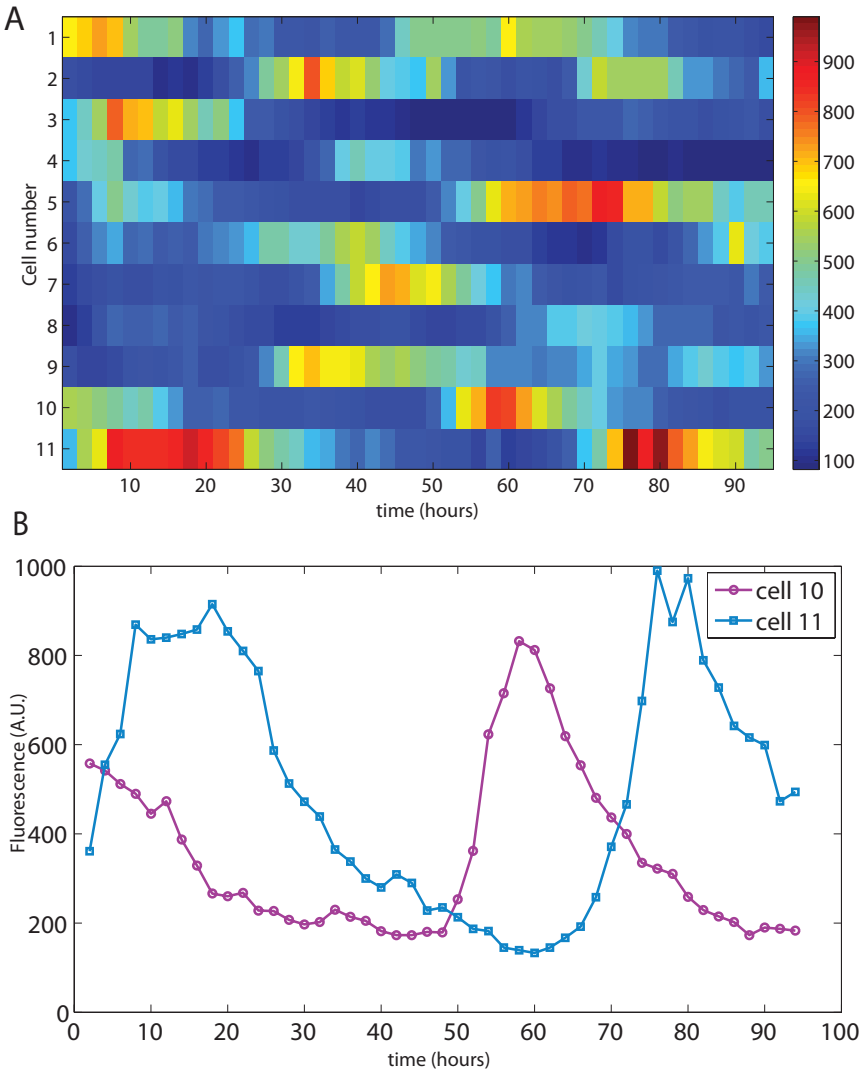

Figure 4.21: Oscillator single-cell trajectories. CHO clone D-2 cultured at $32°C$ in the absence of doxycycline. (A) Heatmap of eleven individual cell fluorescence trajectories (arbitrary units). (B) Trajectories' shape is characteristic of degrade-and-fire model of delayed negative-feedback oscillations.

4.21A). This is in line with the noisy oscillations that are observed in the NFO version of the bacterial oscillator (Stricker et al., 2008)

To ensure that the oscillations are not coupled to the cell-cycle, I arrested CHO D-2 cells in G1 phase by two separate mechanisms, DMSO exposure (Fiore et al., 2002) and low cultivation temperature (Kaufmann et al., 1999), and confirmed the functionality of the autoregulated tTRg negative feedback (Fig 4.22). During this analysis I

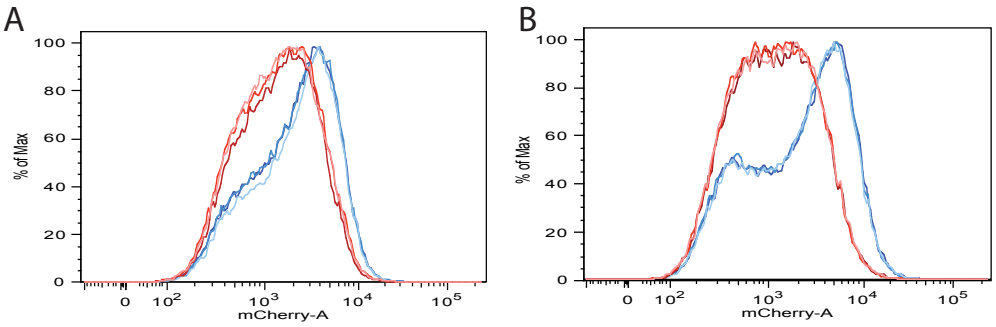

Figure 4.22: CHO clone D-2 cell cycle arrest. Cells were arrested in G1 phase by (A) culturing for 96 hours in 1%(v/v) DMSO or (B) cultivation at $32°C$. In the absence of dox (red curves, triplicate), the cells exhibit the extremely broad distribution characteristic of oscillations. Induction with 243ng/mL dox inactivates the repressor shutting off the auto-regulated negative feedback which results in a high fluorescence peak of constitutive mCherry production (blue curves, triplicate).

observed a widening of the inactivated repressor fluorescence distribution, indicative of potential instability of the clonal population since the cells I used for this analysis had been passaged several times (Barnes et al., 2003; Pilbrough et al., 2009). Subsequent analysis of higher passage number (>ten) CHO clone D-2 confirmed loss of responsiveness to doxycycline and thus further manipulations were performed with low passage number stocks of clone D-2.

To construct the dual-feedback design, CHO clone D-2 requires the addition of the positive feedback module. Since I had constructed both non-competitive (erythromycin based) and competitive (tet-based) positive feedback vectors previously, I used these to supertransduce two separate isolates of CHO clone D-2 and immediately generated clonal cell lines by FACS. Transfections of Phoenix cells to generate

the retroviral supernatants were performed with Fugene 6 as before, and low passage number cD2 populations were transduced with the E5T7e1ig1 and EiA positive feedback vectors. Transduced populations were selected in puromycin, G418 and dox as before and were single-cell sorted by FACS into 96-well plates to isolate the highest EGFP/mCherry fluorescent fractions. A large number of clones were generated and stored in liquid nitrogen. Specifically, 33 erythromycin (EM) positive feedback clones and 37 tetracycline (TET) clones. Such a rich library of clones requires a high throughput method for rapid screening, and thus a subset of these clones was analyzed by flow cytometry. The analysis reveals that many of the dual-feedback clones respond to doxycycline/erythromycin as expected. The fluorescence density plots for a range of induction conditions as shown for a representative EM clone (Fig 4.23A). Time-lapse imaging

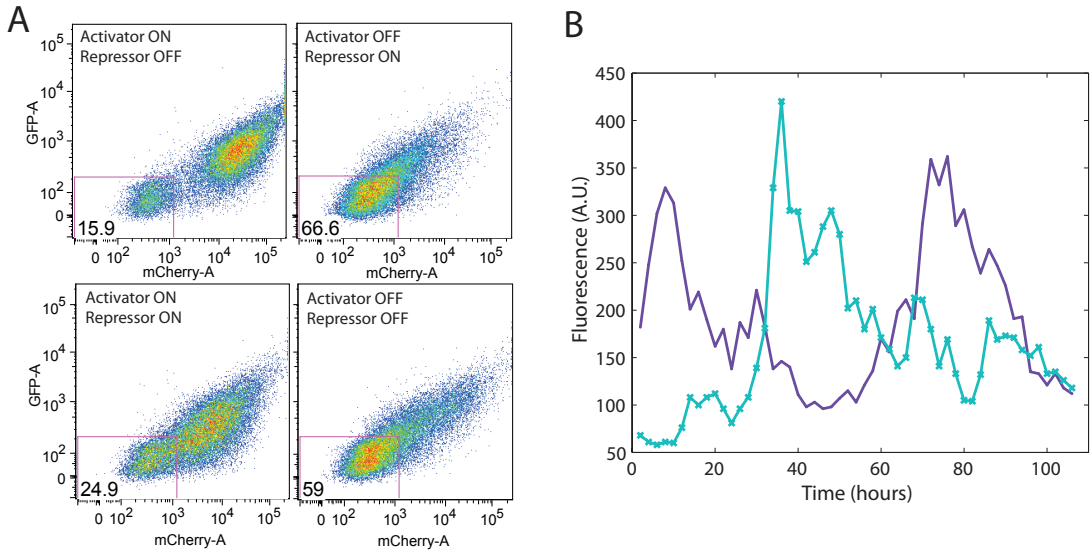

Figure 4.23: Representative non-competitive dual-feedback clone EM-21. (A) Fluorescence density plots for EM-21. Activator is ON at zero erythromycin, OFF at 1ug/mL. Repressor is ON at zero doxycycline, OFF at 243ng/mL. Rectangular gate indicates percent of cells in the lowest EGFP/mCherry expression bin. (B) Two individual cell trajectories of destabilized mCherry signal in EMc21 imaged at $32°C$ in the absence of inducers (fully active repressor and activator).

indicates that the representative non-competitive dual-feedback clone EM-21 is characterized by high-amplitude oscillations of similar frequency to the parent CHO clone D-2

(Fig 4.23B).

High-throughput analysis of this rich clone library to determine the optimal parameter space for oscillations should generate a subset of clones with different characteristic oscillations based on the particular integration sites of the positive feedback constructs. Subsequent characterization of the genomic loci of such integrations within each clone should reveal the genetic differences which make each clone unique and provide novel insights into the regulation of dynamic processes such as oscillations in an epigenetic context.

4.6 Discussion

I successfully created a genomically integrated mammalian synthetic gene circuit that exhibits oscillatory behavior within the native epigenetic context of mammalian transcriptional regulation. The auto-regulated repression that drives the circuit dynamics is mediated by the well-characterized tetR-KRAB chimeric transrepressor. The KRAB silencing domain exerts its activity by inducing the formation of local heterochromatin through the recruitment of KAP1 and other associated factors (Moosmann et al., 1996b; Peng et al., 2007; Groner et al., 2010). While heterochromatin was historically thought of as a stable and inaccessible state of DNA, a recent surge of evidence indicates that heterochromatin appears to be a dynamic entity which can be accessible to transcription (Maison and Almouzni, 2004; Huisinga et al., 2006; Grewal and Elgin, 2007). The circuit that I constructed is the first example of a synthetic negative feedback module in mammalian cells to incorporate epigenetic silencing as the mode of auto-regulated repression to produce a self-sustained dynamic expression readout. The oscillatory pulses of expression generated by this circuit can be used to develop future models of this simple system in order to better understand the complex interaction dynamics of native autoregulated reversible gene silencing.

In addition to exploring negative feedback dynamics, I developed two separate positive feedback architectures for coupling to the negative feedback and generated a

library of dual-feedback clones which can be used to further study the effects of competition between repressor and activator at the promoter level. The use of this clonal library to characterizate the effects of integration site differences on the dynamics of the synthetic circuit behavior should reveal novel insights into the dynamics of native reversible silencing as a function of location within the genome.

4.7 Acknowledgements

Chapter Four contains material in preparation for publication as Kolnik, M., Tsimring, L.S., Hasty, J., 2012: A genomically integrated synthetic mammalian oscillator.

Chapter 5

Summary

As our ability to describe the myriad of diverse components in biological systems has grown exponentially with the development of high-throughput technologies, the field of systems biology has emerged with the goal of understanding the underlying connectivity among individual parts of increasingly complex biological networks. Advancement on this front is enabled by novel means of probing the dynamics of cellular behavior using tools such as microfluidics, as well as synthetic approaches to understanding native regulation through the construction and characterization of designed gene networks. Successful contribution to progress along these two main avenues is the focus of the work presented here.

In Chapter Two, I developed a novel microfluidic culture platform for real-time dynamic stimulation of mammalian cells. The device enables simple, rapid and efficient cell loading via a unique localized on-chip vacuum that allows for sequestration of cells in culture regions with extremely high resistance to fluid flow. This ensures successful long-term perfusion cell-culture that is free of flow-induced shear-stress effects which are potentially detrimental to cell viability and normal biological function. The utility of the culture platform was demonstrated for three commonly used mammalian cell lines and dynamic stimulation provided by the on-chip fluidic function generator was validated using a fluorescent reporter cell line. The highly modular design of the culture

traps allows for ready tunability of the desired ratio of convective to diffusive transport to suit a particular application. The simple design is free of multi-layer PDMS networks or associated control-valves and external hardware and thus lends itself well for general adoption by a broad audience of experimental biologists.

In Chapter Three, I employed the aforementioned microfluidic platform to probe the single-cell response of the NFκB signaling pathway to dynamic stimulation with TNFα. This study presents the first case of tracking the NFκB response of individual cells to a truly dynamic input of inducer in the form of a linear temporal gradient (ramp). Comparison of this mode of stimulation uniquely enabled by microfluidics to a traditional step function reveals marked differences in the timing and amplitude characterstics of the NFκB response. Specifically, a ramp induction which mimics a gradually increasing concentration of TNFα similar to an in-vivo exposure results in enhanced timing variability of the response compared to a step function of the inducer. More significantly, unlike the step experiments which exhibit a high amplitude intial response peak followed by uniform amplitude oscillation peaks, comparable ramp experiments result in completely uniform magnitude of all response peaks. Together these results indicate that an un-natural mode of induction by a high impulse step function of TNFα over-stimulates the initial NFκB amplitude response and obscures the inherent variability in the timing of the response. The implication for future studies of NFκB signaling dynamics is that careful consideration must be given to the mode of stimulation in order to draw biologically relevant conclusions from experimental data.

In Chapter Four, I designed and constructed synthetic autoregulated transcriptional circuits integrated into the genome of mammalian cells. The focus was to couple positive and negative feedback to study the potential of this architecture for generating oscillatory expression behavior. The system was engineered using well-characterized chimeric transcription factors that were further engineered for rapid kinetics of protein turnover to maximize expression dynamics. Different promoter configurations were explored for competitive and non-competitive interactions of the activator and repressor, and cell line optimization was performed to enable time-lapse fluorescent characteriza-

tion of the engineered cell lines. Clonal screening revealed the capacity of the negative feedback architecture to exhibit oscillatory pulses of expression driven by autoregulated epigenetic repression. This synthetic circuit is the first such mammalian module to generate self-sustained pulses of expression using an epigenetic silencing-mediated repression mechanism. Supertransduction with the two modes of positive feedback generated a clonal library of dual-feedback constructs. The characterization of the differences in dynamic behavior of individual clones and correlation to integration site mapping is expected to shed light on how positional effects in the mammalian genome influence gene regulation by reversible silencing.

The overarching theme of these studies points towards the importance of understanding biological processes in a dynamic context. The development of novel microfluidic tools drives progress along this front by enabling the precise spatial and temporal control of the cellular microenvironment. Characterization of the cellular response to dynamic inputs in this manner typically leads to new insights into how biological regulatory networks deal with an ever-changing natural environment. Alongside perturbations of existing networks to gain insight into regulatory dynamics, synthetic biology is successful in constructing de novo artificial gene circuits which replicate certain aspects of biological function in order to shed light on native regulatory mechanisms. The work presented here successfully deploys these strategies to deepen our understanding of the biological dynamics of gene regulation, the final goal of which is to translate this knowledge to applications in medicine and bioenergy production for the betterment of our society.

References

Abràmoff, M., Magalhães, P., and Ram, S., 2004: Image processing with imagej. *Biophotonics international*, **11**(7), 36–42.

Ashall, L., Horton, C., Nelson, D., Paszek, P., Harper, C., Sillitoe, K., Ryan, S., Spiller, D., Unitt, J., Broomhead, D., et al., 2009: Pulsatile stimulation determines timing and specificity of nf-{kappa} b-dependent transcription. *Science's STKE*, **324**(5924), 242.

Barken, D., Wang, C. J., Kearns, J., Cheong, R., Hoffmann, A., and Levchenko, A., 2005: Comment on "oscillations in nf-κb signaling control the dynamics of gene expression". *Science*, **308**(5718), 52. doi:10.1126/science.1107904.

Barnes, L., Bentley, C., and Dickson, A., 2003: Stability of protein production from recombinant mammalian cells. *Biotechnology and bioengineering*, **81**(6), 631–639.

Bennett, M., Pang, W., Ostroff, N., Baumgartner, B., Nayak, S., Tsimring, L., and Hasty, J., 2008: Metabolic gene regulation in a dynamically changing environment. *Nature*, **454**(7208), 1119–1122.

Berridge, M., Bootman, M., Roderick, H., et al., 2003: Calcium signalling: dynamics, homeostasis and remodelling. *Nature Reviews Molecular Cell Biology*, **4**(7), 517–529.

Berthier, E., Young, E., and Beebe, D., 2012: Engineers are from pdms-land, biologists are from polystyrenia. *Lab on a Chip*.

Black, R., Rauch, C., Kozlosky, C., Peschon, J., Slack, J., Wolfson, M., Castner, B., Stocking, K., Reddy, P., Srinivasan, S., et al., 1997: A metalloproteinase disintegrin that releases tumour-necrosis factor-α from cells.

Bochkov, Y., and Palmenberg, A., 2006: Translational efficiency of emcv ires in bicistronic vectors is dependent upon ires sequence and gene location. *Biotechniques*, **41**(3), 283.

Carpenter, A., Jones, T., Lamprecht, M., Clarke, C., Kang, I., Friman, O., Guertin, D., Chang, J., Lindquist, R., Moffat, J., et al., 2006: Cellprofiler: image analysis software for identifying and quantifying cell phenotypes. *Genome biology*, **7**(10), R100.

Charvin, G., Cross, F., and Siggia, E., 2008: A microfluidic device for temporally controlled gene expression and long-term fluorescent imaging in unperturbed dividing yeast cells. *PLoS One*, **3**(1), e1468.

Chen, Y., Jensen, M., and Smolke, C., 2010: Genetic control of mammalian t-cell proliferation with synthetic rna regulatory systems. *Proceedings of the National Academy of Sciences*, **107**(19), 8531.

Chiu, D., Jeon, N., Huang, S., Kane, R., Wargo, C., Choi, I., Ingber, D., and Whitesides, G., 2000: Patterned deposition of cells and proteins onto surfaces by using three-dimensional microfluidic systems. *Proceedings of the National Academy of Sciences*, **97**(6), 2408.

Chung, I., Norris, J., and Benveniste, E., 1991: Differential tumor necrosis factor alpha expression by astrocytes from experimental allergic encephalomyelitis-susceptible and-resistant rat strains. *The Journal of experimental medicine*, **173**(4), 801–811.

Cooksey, G., Elliott, J., and Plant, A., 2011: Reproducibility and robustness of a real-time microfluidic cell toxicity assay. *Analytical chemistry*.

Corish, P., and Tyler-Smith, C., 1999: Attenuation of green fluorescent protein half-life in mammalian cells. *Protein engineering*, **12**(12), 1035–1040.

Dan, L., Chua, C., and Leong, K., 2010: Fibroblast response to interstitial flow: A state-of-the-art review. *Biotechnology and bioengineering*, **107**(1), 1–10.

Deuschle, U., Meyer, W., and Thiesen, H., 1995: Tetracycline-reversible silencing of eukaryotic promoters. *Molecular and cellular biology*, **15**(4), 1907–1914.

Di Carlo, D., Wu, L., and Lee, L., 2006: Dynamic single cell culture array. *Lab Chip*, **6**(11), 1445–1449.

Dolmetsch, R., Lewis, R., Goodnow, C., and Healy, J., 1997: Differential activation of transcription factors induced by ca2+ response amplitude and duration.

Dranoff, G., Jaffee, E., Lazenby, A., Golumbek, P., Levitsky, H., Brose, K., Jackson, V., Hamada, H., Pardoll, D., and Mulligan, R., 1993: Vaccination with irradiated tumor cells engineered to secrete murine granulocyte-macrophage colony-stimulating factor stimulates potent, specific, and long-lasting anti-tumor immunity. *Proceedings of the National Academy of Sciences*, **90**(8), 3539.

Elowitz, M., Leibler, S., et al., 2000: A synthetic oscillatory network of transcriptional regulators. *Nature*, **403**(6767), 335–338.

Ferry, M., Razinkov, I., and Hasty, J., 2011: Microfluidics for synthetic biology: From design to execution. *Synthetic Biology: Methods for Part/Device Characterization and Chassis Engineering*, 295.

Fiore, M., Zanier, R., and Degrassi, F., 2002: Reversible g1 arrest by dimethyl sulfoxide as a new method to synchronize chinese hamster cells. *Mutagenesis*, **17**(5), 419–424.

Fleischmann, R., Adams, M., White, O., Clayton, R., Kirkness, E., Kerlavage, A., Bult, C., Tomb, J., Dougherty, B., Merrick, J., et al., 1995: Whole-genome random sequencing and assembly of haemophilus influenzae rd. *Science*, **269**(5223), 496.

Friedrichsen, S., Harper, C., Semprini, S., Wilding, M., Adamson, A., Spiller, D., Nelson, G., Mullins, J., White, M., and Davis, J., 2006: Tumor necrosis factor-α activates the human prolactin gene promoter via nuclear factor-κb signaling. *Endocrinology*, **147**(2), 773–781.

Fussenegger, M., Morris, R., Fux, C., Rimann, M., Von Stockar, B., Thompson, C., and Bailey, J., 2000: Streptogramin-based gene regulation systems for mammalian cells. *Nature biotechnology*, **18**(11), 1203–1208.

Gilmore, T., 2006: Introduction to nf-κb: players, pathways, perspectives. *Oncogene*, **25**(51), 6680–6684.

Gómez-Sjöberg, R., Leyrat, A., Pirone, D., Chen, C., and Stephen, R., 2007: Versatile, fully automated, microfluidic cell culture system. *Analytical chemistry*, **79**(22), 8557–8563.

Gonzalez-Nicolini, V., and Fussenegger, M., 2005: In vitro assays for anticancer drug discovery-a novel approach based on engineered mammalian cell lines. *Anti-cancer drugs*, **16**(3), 223.

Gossen, M., and Bujard, H., 1992: Tight control of gene expression in mammalian cells by tetracycline-responsive promoters. *Proceedings of the National Academy of Sciences*, **89**(12), 5547.

Gossen, M., Freundlieb, S., Bender, G., Muller, G., Hillen, W., and Bujard, H., 1995: Transcriptional activation by tetracyclines in mammalian cells. *Science*, **268**(5218), 1766–1769.

Grewal, S., and Elgin, S., 2007: Transcription and rna interference in the formation of heterochromatin. *Nature*, **447**(7143), 399–406.

Groner, A., Meylan, S., Ciuffi, A., Zangger, N., Ambrosini, G., Dénervaud, N., Bucher, P., and Trono, D., 2010: Krab–zinc finger proteins and kap1 can mediate long-range transcriptional repression through heterochromatin spreading. *PLoS genetics*, **6**(3), e1000869.

Hayden, M., and Ghosh, S., 2011: Nf-κb in immunobiology. *Cell research*, **21**(2), 223–244.

Hayden, M., and Ghosh, S., 2012: Nf-κb, the first quarter-century: remarkable progress and outstanding questions. *Genes & Development*, **26**(3), 203–234.

Hellen, C., and Sarnow, P., 2001: Internal ribosome entry sites in eukaryotic mrna molecules. *Genes & Development*, **15**(13), 1593–1612.

Hersen, P., McClean, M., Mahadevan, L., and Ramanathan, S., 2008: Signal processing by the hog map kinase pathway. *Proceedings of the National Academy of Sciences*, **105**(20), 7165.

Hess, S., and Webb, W., 2002: Focal volume optics and experimental artifacts in confocal fluorescence correlation spectroscopy. *Biophysical Journal*, **83**(4), 2300–2317.

Hoffmann, A., Levchenko, A., Scott, M., and Baltimore, D., 2002: The ikappa b-nf-kappa b signaling module: temporal control and selective gene activation. *Science's STKE*, **298**(5596), 1241.

Hsu, H., Huang, J., Shu, H., Baichwal, V., Goeddel, D., et al., 1996: Tnf-dependent recruitment of the protein kinase rip to the tnf receptor-1 signaling complex. *Immunity*, **4**(4), 387.

Hsu, H., Xiong, J., Goeddel, D., et al., 1995: The tnf receptor 1-associated protein tradd signals cell death and nf-kappa b activation. *Cell*, **81**(4), 495.

Hu, W., and Temin, H., 1990: Retroviral recombination and reverse transcription. *Science*, **250**(4985), 1227–1233.

Hubbard, S., Walls, L., Ruley, H., and Muchmore, E., 1994: Generation of chinese hamster ovary cell glycosylation mutants by retroviral insertional mutagenesis. integration into a discrete locus generates mutants expressing high levels of n-glycolylneuraminic acid. *Journal of Biological Chemistry*, **269**(5), 3717–3724.

Huisinga, K., Brower-Toland, B., and Elgin, S., 2006: The contradictory definitions of heterochromatin: transcription and silencing. *Chromosoma*, **115**(2), 110–122.

Hung, P., Lee, P., Sabounchi, P., Aghdam, N., Lin, R., and Lee, L., 2005: A novel high aspect ratio microfluidic design to provide a stable and uniform microenvironment for cell growth in a high throughput mammalian cell culture array. *Lab Chip*, **5**(1), 44–48.

Jacobsen, L., Calvin, S., Colvin, K., and Wright, M., 2004: Fugene 6 transfection reagent: the gentle power. *Methods*, **33**(2), 104–112.

Jiang, Y., Woronicz, J., Liu, W., and Goeddel, D., 1999: Prevention of constitutive tnf receptor 1 signaling by silencer of death domains. *Science*, **283**(5401), 543–546.

Jordan, M., Schallhorn, A., and Wurm, F., 1996: Transfecting mammalian cells: optimization of critical parameters affecting calcium-phosphate precipitate formation. *Nucleic acids research*, **24**(4), 596–601.

Kaufmann, H., Mazur, X., Fussenegger, M., and Bailey, J., 1999: Influence of low temperature on productivity, proteome and protein phosphorylation of cho cells. *Biotechnology and bioengineering*, **63**(5), 573–582.

Kemmer, C., Gitzinger, M., Daoud-El Baba, M., Djonov, V., Stelling, J., and Fussenegger, M., 2010: Self-sufficient control of urate homeostasis in mice by a synthetic circuit. *Nature biotechnology*, **28**(4), 355–360.

Khalil, A., and Collins, J., 2010: Synthetic biology: applications come of age. *Nature Reviews Genetics*, **11**(5), 367–379.

Kim, L., Toh, Y., Voldman, J., and Yu, H., 2007: A practical guide to microfluidic perfusion culture of adherent mammalian cells. *Lab Chip*, **7**(6), 681–694.

Kim, L., Vahey, M., Lee, H., and Voldman, J., 2006: Microfluidic arrays for logarithmically perfused embryonic stem cell culture. *Lab Chip*, **6**(3), 394–406.

King, K., Wang, S., Jayaraman, A., Yarmush, M., and Toner, M., 2007: Microfluidic flow-encoded switching for parallel control of dynamic cellular microenvironments. *Lab Chip*, **8**(1), 107–116.

Kramer, B., and Fussenegger, M., 2005: Hysteresis in a synthetic mammalian gene network. *Proceedings of the National Academy of Sciences of the United States of America*, **102**(27), 9517.

Kramer, B., Viretta, A., Daoud-El Baba, M., Aubel, D., Weber, W., and Fussenegger, M., 2004: An engineered epigenetic transgene switch in mammalian cells. *Nature biotechnology*, **22**(7), 867–870.

Krippner-Heidenreich, A., Grunwald, I., Zimmermann, G., Kühnle, M., Gerspach, J., Sterns, T., Shnyder, S., Gill, J., Männel, D., Pfizenmaier, K., et al., 2008: Single-chain tnf, a tnf derivative with enhanced stability and antitumoral activity. *The Journal of Immunology*, **180**(12), 8176–8183.

Lathe, W., Williams, J., Mangan, M., and Karolchik, D., 2008: Genomic data resources: challenges and promises. *Nature Education*, **1**(3).

Lee, P., Gaige, T., and Hung, P., 2008: Dynamic cell culture: a microfluidic function generator for live cellmicroscopy. *Lab Chip*, **9**(1), 164–166.

Lee, P., Gaige, T., and Hung, P., 2011: Microfluidic systems for live cell imaging. *Recent advances in cytometry*, **1**, 77.

Lee, P., Hung, P., Rao, V., and Lee, L., 2006: Nanoliter scale microbioreactor array for quantitative cell biology. *Biotechnology and bioengineering*, **94**(1), 5–14.

Lee, T., and Covert, M., 2010: High-throughput, single-cell nf-κb dynamics. *Current opinion in genetics & development*, **20**(6), 677–683.

Lee, T., Denny, E., Sanghvi, J., Gaston, J., Maynard, N., Hughey, J., and Covert, M., 2009: A noisy paracrine signal determines the cellular nf-{kappa} b response to lipopolysaccharide. *Science's STKE*, **2**(93), ra65.

Leibovitz, A., 1963: The growth and maintenance of tissue–cell cultures in free gas exchange with the atmosphere. *American Journal of Epidemiology*, **78**(2), 173–180.

Li, X., Zhao, X., Fang, Y., Jiang, X., Duong, T., Fan, C., Huang, C., and Kain, S., 1998: Generation of destabilized green fluorescent protein as a transcription reporter. *Journal of Biological Chemistry*, **273**(52), 34970–34975.

Lim, W., 2010: Designing customized cell signalling circuits. *Nature Reviews Molecular Cell Biology*, **11**(6), 393–403.

Liu, A., Lewis, W., and Kay, S., 2007: Mammalian circadian signaling networks and therapeutic targets. *Nature chemical biology*, **3**(10), 630–639.

Longo, D., and Hasty, J., 2006: Dynamics of single-cell gene expression. *Molecular systems biology*, **2**(1).

Longo, D., Hoffmann, A., Tsimring, L., and Hasty, J., 2010: Coherent activation of a synthetic mammalian gene network. *Systems and synthetic biology*, **4**(1), 15–23.

Ludin, B., Doll, T., Meili, R., Kaech, S., and Matus, A., 1996: Application of novel vectors for gfp-tagging of proteins to study microtubule-associated proteins. *Gene*, **173**(1), 107–111.

Luo, C., Zhu, X., Yu, T., Luo, X., Ouyang, Q., Ji, H., and Chen, Y., 2008: A fast cell loading and high-throughput microfluidic system for long-term cell culture in zero-flow environments. *Biotechnology and bioengineering*, **101**(1), 190–195.

Maison, C., and Almouzni, G., 2004: Hp1 and the dynamics of heterochromatin maintenance. *Nature Reviews Molecular Cell Biology*, **5**(4), 296–305.

Mather, W., Bennett, M., Hasty, J., and Tsimring, L., 2009: Delay-induced degrade-and-fire oscillations in small genetic circuits. *Physical review letters*, **102**(6), 68105.

May, T., Eccleston, L., Herrmann, S., Hauser, H., Goncalves, J., and Wirth, D., 2008: Bimodal and hysteretic expression in mammalian cells from a synthetic gene circuit. *PLoS One*, **3**(6), e2372.

Moosmann, P., Georgiev, O., Le Douarin, B., Bourquin, J., and Schaffner, W., 1996a: Transcriptional repression by ring finger protein tif1β that interacts with the krab repressor domain of kox1. *Nucleic acids research*, **24**(24), 4859–4867.

Moosmann, P., Georgiev, O., Le Douarin, B., Bourquin, J., and Schaffner, W., 1996b: Transcriptional repression by ring finger protein tif1β that interacts with the krab repressor domain of kox1. *Nucleic acids research*, **24**(24), 4859–4867.

Moser, S., Rimann, M., Fux, C., Schlatter, S., Bailey, J., and Fussenegger, M., 2001: Dual-regulated expression technology: a new era in the adjustment of heterologous gene expression in mammalian cells. *The journal of gene medicine*, **3**(6), 529–549.

Mukherji, S., and Van Oudenaarden, A., 2009: Synthetic biology: understanding biological design from synthetic circuits. *Nature Reviews Genetics*, **10**(12), 859–871.

Munteanu, A., Constante, M., Isalan, M., and Solé, R., 2010: Avoiding transcription factor competition at promoter level increases the chances of obtaining oscillation. *BMC systems biology*, **4**(1), 66.

Murakami, Y., Matsufuji, S., Hayashi, S., Tanahashi, N., and Tanaka, K., 2000: Degradation of ornithine decarboxylase by the 26s proteasome. *Biochemical and biophysical research communications*, **267**(1), 1–6.

Nelson, D., Horton, C., See, V., Johnson, J., Nelson, G., Spiller, D., Kell, D., and White, M., 2005: Response to comment on" oscillations in nf-κb signaling control the dynamics of gene expression". *Science*, **308**(5718), 52–52.

Nelson, D., Ihekwaba, A., Elliott, M., Johnson, J., Gibney, C., Foreman, B., Nelson, G., See, V., Horton, C., Spiller, D., et al., 2004: Oscillations in nf-{kappa} b signaling control the dynamics of gene expression. *Science's STKE*, **306**(5696), 704.

Nilsson, J., Evander, M., Hammarström, B., and Laurell, T., 2009: Review of cell and particle trapping in microfluidic systems. *Analytica chimica acta*, **649**(2), 141–157.

Noguchi, N., Emura, A., Matsuyama, H., O'Hara, K., Sasatsu, M., and Kono, M., 1995: Nucleotide sequence and characterization of erythromycin resistance determinant that encodes macrolide 2'-phosphotransferase i in escherichia coli. *Antimicrobial agents and chemotherapy*, **39**(10), 2359–2363.

Park, E., Brown, A., DiFeo, M., Barker, T., and Lu, H., 2009: Continuously perfused, non-cross-contaminating microfluidic chamber array for studying cellular responses to orthogonal combinations of matrix and soluble signals. *Lab Chip*, **10**(5), 571–580.

Pedersen, J., Boschetti, F., and Swartz, M., 2007: Effects of extracellular fiber architecture on cell membrane shear stress in a 3d fibrous matrix. *Journal of biomechanics*, **40**(7), 1484–1492.

Peng, H., Gibson, L., Capili, A., Borden, K., Osborne, M., Harper, S., Speicher, D., Zhao, K., Marmorstein, R., Rock, T., et al., 2007: The structurally disordered krab repression domain is incorporated into a protease resistant core upon binding to kap-1-rbcc domain. *Journal of molecular biology*, **370**(2), 269–289.

Pilbrough, W., Munro, T., and Gray, P., 2009: Intraclonal protein expression heterogeneity in recombinant cho cells. *PLoS One*, **4**(12), e8432.

Poiesi, C., Albertini, A., Ghielmi, S., Cassani, G., and Corti, A., 1993: Kinetic analysis of tnf-α oligomer-monomer transition by surface plasmon resonance and immunochemical methods. *Cytokine*, **5**(6), 539–545.

Pomerantz, J., and Baltimore, D., 2002: Two pathways to nf-κb. *Molecular cell*, **10**(4), 693–695.

Pourquié, O., 2003: The segmentation clock: converting embryonic time into spatial pattern. *Science's STKE*, **301**(5631), 328.

Quan, J., and Tian, J., 2009: Circular polymerase extension cloning of complex gene libraries and pathways. *PloS one*, **4**(7), e6441.

Regehr, K., Domenech, M., Koepsel, J., Carver, K., Ellison-Zelski, S., Murphy, W., Schuler, L., Alarid, E., and Beebe, D., 2009: Biological implications of polydimethylsiloxane-based microfluidic cell culture. *Lab Chip*, **9**(15), 2132–2139.

Rinaudo, K., Bleris, L., Maddamsetti, R., Subramanian, S., Weiss, R., and Benenson, Y., 2007: A universal rnai-based logic evaluator that operates in mammalian cells. *Nature biotechnology*, **25**(7), 795–801.

Rossi, F., Guicherit, O., Spicher, A., Kringstein, A., Fatyol, K., Blakely, B., Blau, H., et al., 1998: Tetracycline-regulatable factors with distinct dimerization domains allow reversible growth inhibition by p16. *Nature genetics*, **20**, 389–393.

Ruder, W., Lu, T., and Collins, J., 2011: Synthetic biology moving into the clinic. *Science*, **333**(6047), 1248–1252.

Scallan, J., Huxley, V., and Korthuis, R., 2010: Capillary fluid exchange: Regulation, functions, and pathology. In *Colloquium Lectures on Integrated Systems Physiology-\ nl\ hspace* 18pt From Molecules to Function*, volume 2, 1–94. Morgan & Claypool Publishers.

Scheidereit, C., 2006: Iκb kinase complexes: gateways to nf-κb activation and transcription. *Oncogene*, **25**(51), 6685–6705.

Schenborn, E., Goiffon, V., et al., 2000: Calcium phosphate transfection of mammalian cultured cells. *Methods in Molecular Biology - Clifton Then Totowa METHODS IN MOLECULAR BIOLOGY-CLIFTON THEN TOTOWA-*, **130**, 135–146.

Shih, V., Tsui, R., Caldwell, A., and Hoffmann, A., 2010: A single nfκb system for both canonical and non-canonical signaling. *Cell research*, **21**(1), 86–102.

Spiller, D., Wood, C., Rand, D., and White, M., 2010: Measurement of single-cell dynamics. *Nature*, **465**(7299), 736–745.

Sprengel, R., and Hasan, M., 2007: Tetracycline-controlled genetic switches. *Conditional Mutagenesis: An Approach to Disease Models*, 49–72.

Stricker, J., Cookson, S., Bennett, M., Mather, W., Tsimring, L., and Hasty, J., 2008: A fast, robust and tunable synthetic gene oscillator. *Nature*, **456**(7221), 516–519.

Stuhlmann, H., and Berg, P., 1992: Homologous recombination of copackaged retrovirus rnas during reverse transcription. *Journal of virology*, **66**(4), 2378–2388.

Tay, S., Hughey, J., Lee, T., Lipniacki, T., Quake, S., and Covert, M., 2010: Single-cell nf-[kgr] b dynamics reveal digital activation and analogue information processing. *Nature*, **466**(7303), 267–271.

Tigges, M., Dénervaud, N., Greber, D., Stelling, J., and Fussenegger, M., 2010: A synthetic low-frequency mammalian oscillator. *Nucleic acids research*, **38**(8), 2702–2711.

Tigges, M., Marquez-Lago, T., Stelling, J., and Fussenegger, M., 2009: A tunable synthetic mammalian oscillator. *Nature*, **457**(7227), 309–312.

Toepke, M., and Beebe, D., 2006: Pdms absorption of small molecules and consequences in microfluidic applications. *Lab on a Chip*, **6**(12), 1484–1486.

Urrutia, R., et al., 2003: Krab-containing zinc-finger repressor proteins. *Genome Biol*, **4**(10), 231.

Vo, K., Michaelis, S., Paddon, C., et al., 1997: Recombination-mediated pcr-directed plasmid construction in vivo in yeast. *Nucleic acids research*, **25**(2), 451–452.

Wach, A., 1996: Pcr-synthesis of marker cassettes with long flanking homology regions for gene disruptions in s. cerevisiae. *Yeast*, **12**(3), 259–265.

Wajant, H., Henkler, F., and Scheurich, P., 2001: The tnf-receptor-associated factor family:: Scaffold molecules for cytokine receptors, kinases and their regulators. *Cellular signalling*, **13**(6), 389–400.

Wajant, H., Pfizenmaier, K., and Scheurich, P., 2003: Tumor necrosis factor signaling. *Cell Death & Differentiation*, **10**(1), 45–65.

Wang, C., and Levchenko, A., 2009: Microfluidics technology for systems biology research. *Methods Mol Biol*, **500**, 203–219.

Weber, W., and Fussenegger, M., 2006: Pharmacologic transgene control systems for gene therapy. *The journal of gene medicine*, **8**(5), 535–556.

Weber, W., and Fussenegger, M., 2011: Emerging biomedical applications of synthetic biology. *Nature Reviews Genetics*.

Weber, W., Fux, C., Daoud-El Baba, M., Keller, B., Weber, C., Kramer, B., Heinzen, C., Aubel, D., Bailey, J., and Fussenegger, M., 2002: Macrolide-based transgene control in mammalian cells and mice. *Nature biotechnology*, **20**(9), 901–907.

Weber, W., Schoenmakers, R., Keller, B., Gitzinger, M., Grau, T., Daoud-El Baba, M., Sander, P., and Fussenegger, M., 2008: A synthetic mammalian gene circuit reveals antituberculosis compounds. *Proceedings of the National Academy of Sciences*, **105**(29), 9994.

Wendland, J., 2003: Pcr-based methods facilitate targeted gene manipulations and cloning procedures. *Current genetics*, **44**(3), 115–123.

Young, E., Wheeler, A., and Simmons, C., 2006: Chips & tips: Avoiding bubble injection by droplet merging.

Yu, H., Alexander, C., and Beebe, D., 2007: Understanding microchannel culture: parameters involved in soluble factor signaling. *Lab Chip*, **7**(6), 726–730.

Zhang, X., and Roper, M., 2008: Microfluidic perfusion system for automated delivery of temporal gradients to islets of langerhans. *Analytical chemistry*, **81**(3), 1162–1168.

Zhu, M., and Fu, Y., 2010: The complicated role of nf-κb in t-cell selection. *Cellular & molecular immunology*, **7**(2), 89–93.